A Classical Analysis of Double Ionization of Helium in Ultra Short Laser Pulses

Dissertation

zur Erlangung des Doktorgrades
der Naturwissenschaften
(Dr. rer. nat.)

dem Fachbereich Physik
der Philipps-Universität Marburg

vorgelegt von

Lisa Beran
aus Seattle, WA

Marburg (Lahn)
Mai 2014

Vom Fachbereich Physik der Philipps-Universität Marburg
als Dissertation angenommen am 24.06.2014
Erstgutachter: Prof. Bruno Eckhardt
Zweitgutachter: Prof. Mackillo Kira
Tag der Mündlichen Prüfung: 07.07.2014
Hochschulkennziffer 1180

Declaration of Authorship

I, Lisa BERAN, declare that this thesis, titled 'A Classical Analysis of Double Ionization of Helium in Ultra Short Laser Pulses' and the work presented in it are my own. I confirm that:

- This work was done wholly or mainly while in candidature for a research degree at this University.
- Where any part of this thesis has previously been submitted for a degree or any other qualification at this University or any other institution, this has been clearly stated.
- Where I have consulted the published work of others, this is always clearly attributed.
- Where I have quoted from the work of others, the source is always given. With the exception of such quotations, this thesis is entirely my own work.
- I have acknowledged all main sources of help.
- Where the thesis is based on work done by myself jointly with others, I have made clear exactly what was done by others and what I have contributed myself.

Signed: _____

Date: _____

PHILIPPS-UNIVERSITÄT MARBURG

Abstract

Department of Physics

Doctoral Thesis

A Classical Analysis of Double Ionization of Helium in Ultra Short Laser Pulses

by Lisa BERAN

Experiments of double ionization in noble gases [58, 64, 68, 84] were the catalyst for extensive theoretical investigations [9, 11, 13, 21, 39, 80, 87]. The measurement of the momenta of outgoing electrons in non-sequential strong field double ionization exposed the correlated nature of their escape [66, 67, 88, 90].

A (1+1)-dimensional model for helium, introduced in [25, 73], has been the foundation of ongoing research into non-sequential double ionization [24, 26, 27, 71, 74]. The model reproduces the re-scattering scenario, the correlation between the outgoing electrons, and the interference patterns in the momentum distribution [72]. The observed interference patterns depend on the amplitude of the external field, pulse duration, and carrier envelope phase.

Guided by the semi-classical idea that many paths contribute to the double ionization events and the interference between these paths could cause the patterns, a rigorous analysis of the classical trajectories depicting double ionization was undertaken. Applying few-cycle pulses, the effects from multiple re-scattering are intrinsically minimized. In classical calculations, field parameters were varied and configurations yielding trajectories of reduced complexity were targeted. The classical trajectories allow a connection between the initial conditions in phase space and the final states to be established. A link between the external field strength and the electrons initial conditions was found.

In the single-cycle limit, the electrons mutual repulsion ensures that anti-parallel double ionization is the only double ionization mechanism at intensities above the threshold. Stable and symmetric back-to-back double ionization trajectories are identified. Parallel non-symmetric double ionization with same final momentum was generated from two-cycle fields. The extent of the frequency and field strength dependency on classical non-sequential double ionization was determined.

PHILIPPS-UNIVERSITÄT MARBURG

Zusammenfassung

Fachbereich Physik

Dissertation

A Classical Analysis of Double Ionization of Helium in Ultra Short Laser Pulses

vorgelegt von Lisa BERAN

Die Dynamik der Doppelionisation in Edelgasen geriet erstmals durch die Experimente von L'Huillier *et al* [58] in den Fokus experimenteller [64, 68, 84] und theoretischer [9, 11, 13, 21, 39, 80, 87] Forschung. Die Messung der Impulse der das Atom verlassenden Elektronen im Fall von nicht-sequentieller Doppelionisation in starken Feldern zeigte den korrelierten Charakter des Ionizationsprozesses [66, 67, 88, 90].

Ein (1+1)-dimensionales Model für Helium wurde in [25, 73] eingeführt und war die Grundlage weiterer Forschung an Doppelionisation [24, 26, 27, 71, 74]. Das Modell reproduziert das Rückstreu-Szenario, die Korrelation zwischen den das Atom verlassenden Elektronen sowie das Interferenzmuster der Impulsverteilung [72]. Letzteres hängt von der Amplitude des externen Feldes, der Pulsdauer sowie der Phase ab.

Inspiriert von der semiklassischen Idee, dass viele Pfade zu Doppelionisationsereignissen beitragen und die Interferenz zwischen diesen die Muster in den Impulsverteilung bewirken, wurde eine rigorose Analyse der klassischen Trajektorien, welche Doppelionisation zeigen, durchgeführt. Durch Anwendung von kurzen Pulsen werden die Effekte von Mehrfachstreuung intrinsisch minimiert. In klassischen Berechnungen wurden Feldparameter variiert und Konfigurationen, die zu Trajektorien mit reduzierter Komplexität führen, gesucht. Die klassischen Trajektorien ermöglichen es, die Anfangsbedingungen und die Endzustände im Phasenraum miteinander in Beziehung zu setzen. Es wurde ein Zusammenhang zwischen externer Feldstärke und den Anfangsbedingungen der Elektronen gefunden.

Im Grenzfall eines einzelnen Zyklus sorgt die gegenseitige Abstoßung der Elektronen dafür, dass nur antiparallele Doppelionisation möglich ist. Nicht-sequentielle Doppelionisationen mit dem gleichen Endimpuls werden durch Zwei-Zyklen-Felder erzeugt. Das Auftreten klassischer nicht-sequentieller Doppelionisation wurde in Abhängigkeit von Frequenz sowie Feldstärke untersucht.

Acknowledgements

I would like to begin by thanking my Mom and Dad, my sisters Marlene and Kristine, and my three awesome nephews James, Peter, and Willem. Thank you for your love and support.

I would like to thank Davor, with whom everything began.

Vielen Dank an meine Tanten Inge und Gisela, und meine Onkeln Manfred und Jürgen. Vielen Dank an Frau und Herr Löffler.

Thank you to my friends André, Volker, Tommy, Fabian, and Nico. Thanks for your visits and friendship.

Thank you to Mischa, Konstanze, Kristof, Hannes, Tobias, Patrick, Jens, Stefan, Michael G., Michael R., and Shuxin. They started out as colleagues but are now friends.

Ein ganz herzliches Dankeschön an alle meine Mitbewohner in Marburg: Susi, Annika, Isa, Martin, Amrei, Wiebke, Lukas, Stef, und Mimi.

Vielen Dank an Dr. Kauß, Dr. Redies, Fr. Nölling, Fr. Ribke für die hervorragende Betreuung.

Thanks to Jan Thiede for carrying out the quantum mechanical simulations that produced the figures in Chapter 8.

I would like to thank my professor, Bruno Eckhardt, for supervising my research. Thank you for this opportunity and the continued support these past years.

Contents

List of Figures

Abbreviations

MPI	**M**ulti-**P**hoton **I**onization
ATI	**A**bove **T**hreshold **I**onization
HHG	**H**igh **H**armonic **G**eneration
BSI	**B**arrier **S**uppression **I**onization
SAE	**S**ingle-**A**ctive **E**lectron Approximation
SI	**S**ingle **I**onization
DI	**D**ouble **I**onization
SDI	**S**equential **D**ouble **I**onization
NSDI	**N**on-**S**equential **D**ouble **I**onization
RESI	**R**ecollision **E**xcitation with **S**ubsequent **I**onization
REDI	**Re**collision-Induced **D**irect **I**onization
COLTRIMS	**Col**d-**T**arget **R**ecoil-**I**on **M**omentum **S**pectroscopy

Atomic Units

Grossmann, Frank (2008). *Theoretical Femtosecond Physics*

Definitions	**S.I.**	**a.u.**
Planck constant $\hbar$	$\approx 1.0546 \times 10^{-34}\,\mathrm{J\,s}$	$= 1\,\hbar$
Charge e	$\approx 1.6022 \times 10^{-19}\,\mathrm{A\,s}$	$= 1\,e$
Electron mass m_e	$\approx 9.10194 \times 10^{-31}\,\mathrm{Kg}$	$= 1\,m_e$
Length a_0	$\approx 5.2918 \times 10^{-11}\,\mathrm{m}$	$= 1\,a_0$
Quantities	**S.I.**	**a.u.**
Energy $2\lvert E_1\rvert$	$\approx 27.212\,\mathrm{eV}$	$= 1\,\frac{\hbar^2}{a_0^2 m_e}$
Electric field F_0	$\approx 5.1427 \times 10^{11}\,\mathrm{V\,m^{-1}}$	$= 1\,\frac{\hbar^2}{a_0^3 m_e e}$
Electric field intensity I	$\approx 3.5101 \times 10^{16}\,\mathrm{W\,cm^{-2}}$	$= 5.4556\,\frac{\hbar^3}{a_0^6 m_e^2}$
Time t_0	$\approx 24.189\,\mathrm{as}$	$= 1\,\frac{m_e a_0^2}{\hbar}$

Dedicated to my parents

Chapter 1

Light-Matter Interaction

1.1 Multiphoton Ionization

The mathematical explanation of the photoelectric effect, first observed by Hertz in 1887 [76], was provided by Einstein in 1905. Light transfers energy to matter via energy quanta, or *photons*. The energy of a photon is $\hbar\omega$, with $\hbar = h/2\pi$ the reduced Planck's constant and ω the photons' angular frequency. A bound electron has an ionization potential I_p. The electron is photoionized when it absorbs a photon with energy larger than the ionization potential of the electron. An illustration of this process is seen in Figure 1.1 a). The maximal kinetic energy of the resulting photoelectron is given by

$$E_{max} = \hbar\omega - I_p. \tag{1.1}$$

In 1929, Maria Göppert-Mayer predicted that if the energy of one photon is insufficient for direct ionization, N photons might be absorbed simultaneously [37]. This is illustrated in Figure 1.1 b). The combined energy allows the bound electron to reach the continuum, e.g. the free state

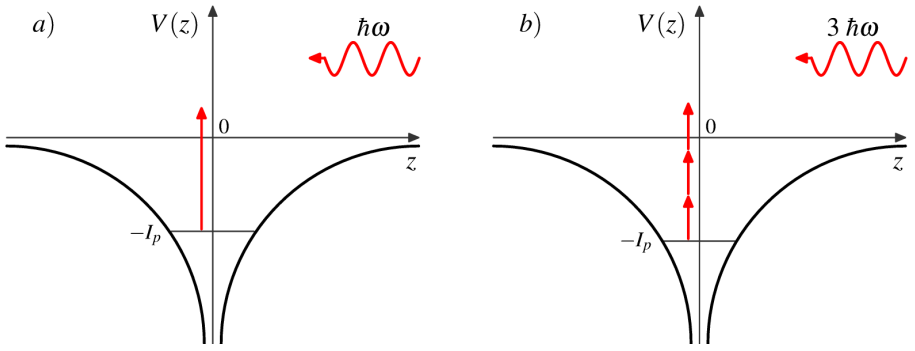

FIGURE 1.1: An electron with ionization potential I_p may absorb a) one photon or b) multiple photons, provided their cumulative energy is larger than the electrons' binding energy.

above the potential. The maximum kinetic energy of the freed electron is

$$E_{max} = N\hbar\omega - I_p. \tag{1.2}$$

Lasers with intensities of $I \geq 10^{10}$ Wcm^{-2} needed to observe multiphoton ionization (MPI) in noble gases were first developed in the 1960's by Voronov [82, 83] and Agostini *et al* [1]. Research by Keldysh, Gold and Bebb further developed the theory of N-photon ionization of gases [10, 36, 48].

In 1964, Keldysh introduced an adiabatic parameter to classify the two mechanisms of ionization known at that time [48], i.e. multiphoton ionization and tunnel ionization. The Keldysh parameter which is defined by

$$\gamma = \frac{\omega}{\omega_t}, \tag{1.3}$$

divides two regimes.

A linearly polarized external field $F(t) = F_0 \cos\omega t$, with an amplitude F_0 and frequency ω, distorts the Coulomb field of an atom. This generates a potential barrier, alternating with the laser frequency on either side of the atom, through which an electron can tunnel. The time or frequency of tunneling is $\omega_t = F_0/(I_p)^{\frac{1}{2}}$. This process, which is dominant for $\gamma \ll 1$, is called tunnel ionization and is explained in more detail in the next section.

For atoms in fields with frequency $\omega \gg \omega_t$ or $\gamma \gg 1$, the electron does not have time to tunnel. By absorbing photons, it passes through virtual energy levels until it reaches the continuum. This is the multiphoton ionization described above. It can be described by time-dependent perturbation theory [16]. The effect of the external field can be seen as a small perturbation of the Coulomb potential. Perturbation theory is used to describe MPI for intensities up to 10^{13}W/cm^{-2}.

1.2 Tunnel and Barrier-Suppression Ionization

In the case of long wavelengths ($\omega \ll \omega_t$), ionization proceeds adiabatically. In the time it takes an electron to tunnel, the change in the external laser field is negligible. Due to the low barrier, the bound electron can tunnel and ionize with a certain probability. The rate of ionization, to first order, is independent of laser frequency and depends mainly on the instantaneous value of the external field amplitude [48]. A generalization for the tunneling rate of arbitrary atoms was developed by Ammosov, Delone, and Krainov (ADK-Theory) [4].

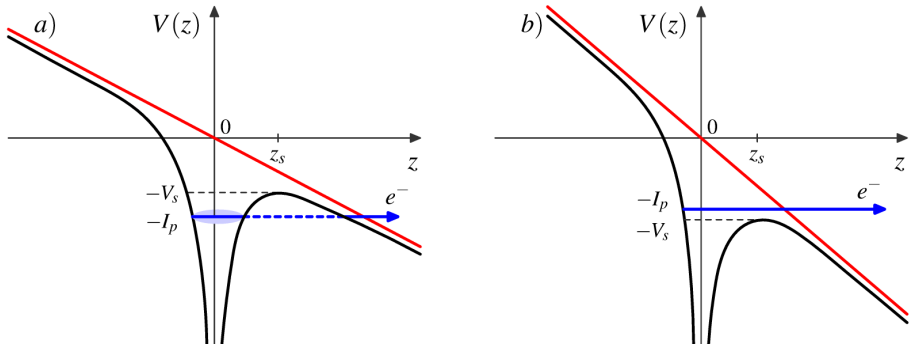

FIGURE 1.2: In *a*), the superposition of the linearly polarized electric field (red) and the Coulomb potential (black) of an atom shows a local maximum, i.e. the Stark saddle point, at z_s with energy V_s. An electron has a finite probability to traverse the barrier (dotted blue line). *b*) illustrates the case where the strength of the electric field creates a saddle point in the Coulomb field of the ion that is lower than the ionization potential of the bound electron.

The ionization rate peaks at the maximal amplitude, F_0, in the oscillating field. The ionization probability is confined to a small interval around the extrema in the field oscillation. This is illustrated in Figure 1.2 *a*).

In the case of very strong fields, a peak in the external field may distort the Coulomb potential of the atom such that the potential barrier is lower than the ionization potential of an electron, see Figure 1.2 *b*). The electron does not tunnel but can pass directly over the potential barrier. This is called barrier-suppression ionization (BSI). The intensity threshold for BSI can be found using a simple one-dimensional model [6, 7].

The superposition of the Coulomb potential and a quasi-static laser field results in a total potential

$$V(x) = -\frac{Z}{|x|} - F_0 x. \tag{1.4}$$

The atomic number is given by Z. The potential has a local maximum x_{max} which can be found by $\mathrm{d}V(x)/\mathrm{d}x = 0$, evaluated at $x = x_{max}$. Setting the ionization potential equal to the potential $V(x_{max})$ results in the critical electric field

$$F_0^{crit} = \frac{I_p^2}{4Z} \tag{1.5}$$

and intensity $I^{crit} = (F_0^{crit})^2$. At this field intensity, the Coulomb potential is deformed so strongly that the electrons escape without tunneling.

1.3 Above Threshold Ionization

In 1979, Agostini *et al* performed experiments on six-photon ionization of xenon [2]. In the energy spectrum, one peak corresponded to an electron ionized with the energy of six photons.

A second, much smaller peak, was found at one photon energy beyond the first. An electron can be ionized by absorbing more photons than the minimum necessary to overcome its binding energy. This ionization process is called above threshold ionization (ATI) and is illustrated in Figure 1.3 *a*).

The kinetic energy of the ionized electron is

$$E_{kin} = (N+s)\hbar\omega - I_p, \tag{1.6}$$

where N is the minimum number of photons for ionization and s the number of excess photons.

A free electron in an electric field gains a cycle-averaged kinetic energy due to its oscillation in the field. This is called the ponderomotive energy, or quiver energy,

$$U_p = \frac{F_0^2}{4\omega^2} = \frac{I}{4\omega^2}, \tag{1.7}$$

where F_0 is the peak field amplitude, ω the frequency of the laser, and I the laser intensity. Since the pondermotive energy is directly proportional to the field's intensity, the Rydberg and continuum states are shifted upwards by U_p and so there is a corresponding increase in the intensity-dependent ionization potential of the atom [16]. The resulting kinetic energy of the photoelectron is

$$E_{kin} = (N+s)\hbar\omega - (I_p + U_p). \tag{1.8}$$

The coupling between atomic states with the electric field induces the AC-Stark shift of the ionization potential [65]. For pulses in the picosecond range, the field oscillates slow enough so that the photoelectron can regain the ponderomotive energy deficit created by the Stark-shifted ionization potential [17]. The energy cancels out the Stark shift and its total energy is given by Equation 1.6. However, subpicosecond pulses are short enough so that the ponderomotive energy of the field electron is not fully converted into translational kinetic energy, and its energy is given by Equation 1.8 [3].

1.4 High Harmonic Generation

When a laser pulse with intensities of $10^{13} - 10^{15}$ W/cm^{-2} and a frequency ω_f interacts with a gas, radiation is emitted at frequencies Ω that are a high multiple of ω_f: $\Omega = q\omega_f$, $q = 3, 5, ...$ This was dubbed high harmonic generation (HHG). The spectrum of this process has interesting features and was the catalyst for intense research, see [57] and references within. In the spectrum, a decrease in the harmonic intensity at lowest order harmonics, a broad plateau region at increasing intensities, and a sharp cut-off at the highest harmonics can be seen. The

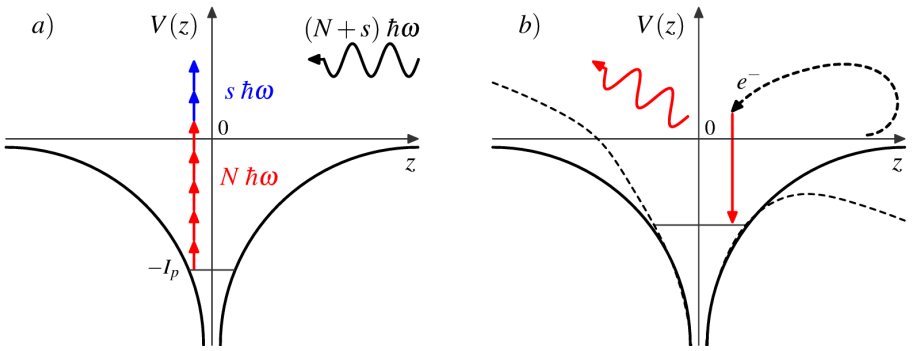

FIGURE 1.3: *a*) is a schematic depiction of above threshold ionization. A bound electron can absorb more photons than necessary to ionize. In *b*), a schematic illustration of high harmonic generation is presented. An electric field initially bends the Coulomb potential allowing an electron to tunnel-ionize. When the electric field changes sign, the ionized electron is turned back to its parent ion. Falling back to its bound state, the electron releases a harmonic, whose photon energy is the sum of the electrons' ionization potential and kinetic energy.

maximum harmonic photon energy is given by a cut-off law [51],

$$E_{max} = I_p + 3.17U_p. \tag{1.9}$$

The ponderomotive potential, U_p, is given by Equation 1.7.

In 1993, Corkum [21] and Kulander, Krause, and Schafer [51, 52, 54] introduced a simple semi-classical three-step model. It not only explains features of HHG, but also those of ATI and double ionization, which is discussed in the following section. In the first step, a linearly polarized laser field maximum distorts the Coulomb potential. An electron may escape by tunneling through the potential barrier. It emerges with zero momentum. The motion of the electron is described by classical equations of motion of an electron in an electromagnetic field. In the second step, the electron is accelerated and, when the external field changes sign a quarter of a cycle later, it is turned back to the ion. In the third step, the electron recombines with the ion. A harmonic with the combined energy of the electrons' ionization potential and its kinetic energy, acquired in the external field, is released. A schematic of this process is found in Figure 1.3 *b*).

By studying classical electron trajectories, Corkum found that, depending on when the electron is ionized, it returns to the ion with different energies. If the electron is ionized at $\omega t = 17°$, it will return with the maximal energy $3.17U_p$ [21].

1.5 Double Ionization in Intense Laser Fields

Double ionization occurs when the re-scattering electron transfers energy to a bound electron and both ionize together, within a fraction of a field cycle. The classical dynamics of double ionization are rigorously studied in this thesis.

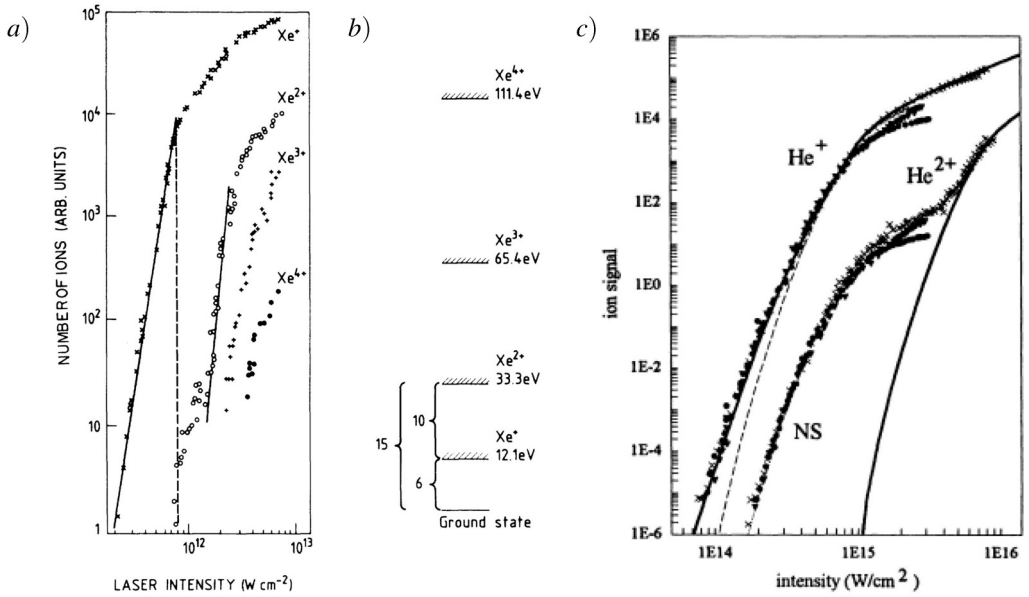

FIGURE 1.4: *a*) shows a double logarithmic plot of xenon ionization yields with respect to laser intensity from experiments described in [58]. The vertical dashed line marks the saturation intensity I_s for Xe^+-ions. Below I_s there is a significant contribution to the Xe^{2+}-ion yield. At intensities above I_s, Xe^{2+}-ions are formed by a step-wise process: Xe absorbs 6 photons from the ground state to singly ionize, then Xe^+ absorbs a further 10 photons to doubly ionize. A schematic representation of these processes is shown in *b*). In *c*), a double logarithmic plot of the He^+/He^{2+} signal with respect to the laser intensity measured by Walker *et al* is shown [84]. The solid line was found using the SEA approximation. The direct double ionization yields would first be accurately reproduced when electron correlation effects were taken into account [12, 87].

In 1983, L'Huillier *et al* performed the first short laser pulse experiments which indicated a direct double ionization process in noble gases [58]. In Figure 1.4 *a*), their findings show the number of Xenon ions recorded for electric field intensities between 10^{11}W/cm^2 and 10^{13}W/cm^2. Doubly charged ions are recorded at intensities below the saturation intensity (vertical dashed line) for singly charged ions. There, the Xe^{2+}-ions are created via a direct absorption of 15 photons. A schematic illustration of this process is seen in Figure 1.4 *b*). At intensities higher than the saturation intensity, double ionization proceeds step-wise with each electron absorbing photons independently.

A decade later, Walker *et al* measured the ion signal for helium [84]. In Figure 1.4 *c*), their measurements exhibit a pronounced enhancement of He^{2+}-ions at intensities below the saturation intensity for singly charged helium ions. The solid line along the He^{2+}-signal was calculated using the single-active electron (SAE) approximation, in which it is assumed that the laser interacts only with the weakest bound electron. It does not predict the low-intensity behavior of the He^{2+} signal. It was concluded that the double ionization signal, at intensities which cannot be modeled by the SAE approximation, is a result of correlated electron processes in the double ionization dynamics. The link between the two double ionization mechanisms, i.e. the

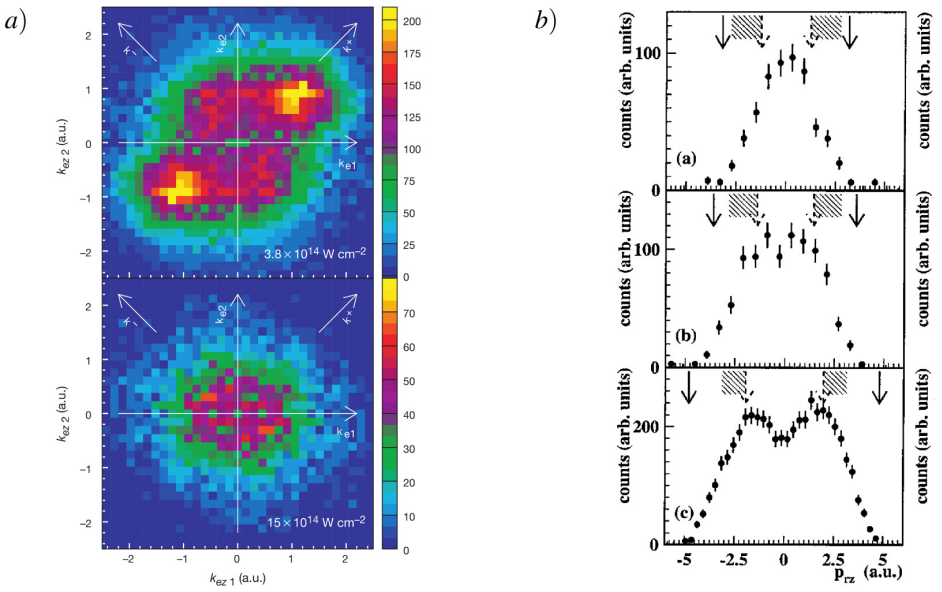

FIGURE 1.5: The momentum distribution from double ionization of argon, generated from two different laser field intensities, is given in a). The z-component of the final momentum of the first electron (horizontal axis) is plotted against that of the second electron (vertical axis) [88]. The laser intensity used in these experiments was 3.8×10^{14} W/cm^{-2}. It lies within the "knee" region in double ionization signal. In the upper plot, the first and third quadrants host a substantial signal from both electrons with similar momentum. The two electrons are emitted from the Ar atom side-by-side. In the lower figure, with laser intensity 15×10^{14} W/cm^{-2}, the electron momentum has an evenly scattered distribution. In b), the projection of the He^{2+}-ion momentum distribution along the electric field vector p_{rz} integrated over the momentum component perpendicular to the field polarization p_{ry} is plotted [90]. With increasing laser intensity, $\left[\text{a) } 2.9 \times 10^{14} \text{ W/cm}^{-2}, \text{ b) } 3.8 \times 10^{14} \text{ W/cm}^{-2}, \text{ c) } 6.6 \times 10^{14} \text{ W/cm}^{-2}\right]$, a pronounced double hump structure emerges. Further details are given in the text.

non-sequential and the sequential double ionization, is characterized by the "knee structure" in the double ionization signal.

In 2000, Weber *et al* determined the final state momentum distributions for two electrons emitted from an argon atom [88]. In the experiments, the momentum of one electron and the momentum of the recoil ion were measured. From the conservation of momentum in the system, the momentum of the second electron was calculated. The momentum distribution in top subplot in Figure 1.5 a) was generated with a laser pulse intensity at the "knee" in the double ionization signal. The z-component of the momentum from the first electron is plotted against that of the second electron. In the first and third quadrants, both electrons' final state momenta have the same sign. A strong signal is located at approximately $|1|$ a.u.. In the second and fourth quadrant, the signal is strongly suppressed. The second plot in a) was created with a field intensity from the sequential double ionization regime. Here, the strong correlation between the magnitude and the direction of the momentum of the outgoing electrons is lost.

In Figure 1.5 b), the differential yields of the He^{2+}-ion momentum component along the field polarization axis, p_{rz}, is plotted [90]. For a laser intensity at the threshold for non-sequential

double ionization (NSDI), there is a maximum at the origin of the momentum distribution (top plot). With increasing field intensity, the distribution broadens and a double peak structure emerges (bottom plot). If the recoil ion momentum is equal to the sum of both electrons' momenta with the opposite sign, then it follows that the momentum distribution of the recoil ion mirrors that of the electrons'. The distribution extends along the horizontal axis to the value $2\sqrt{4U_p}$, U_p is the ponderomotive energy, and is indicated to by the arrows in the plots. This value corresponds to the parallel emission of two electrons at a zero-crossing in the external field.

1.5.1 Sequential Ionization

Sequential double ionization is represented by two steps of single ionization. The two electrons are emitted sequentially, each by independent interactions with the laser field. In the photon picture, each electron absorbs photons independently. In the field picture, each electron tunnels independently at different times during the laser pulse.

For low frequencies and moderate field intensities, where the electric field may be approximated as quasi-static, estimates for the stepwise ionization rates can be found using the ADK formula [4]. This tunnel ionization rate, w, is related to the ionization potential and electric field strength F_0 via

$$w \sim \exp\left[-\frac{2(2I_p)^{\frac{3}{2}}}{3F_0}\right]. \tag{1.10}$$

The "knee" structure in the double ionization yields cannot be explained by any kind of sequential process.

1.5.2 Non-Sequential Ionization

The results from the experiments presented in the previous section lead to the descriptions of various mechanisms which accurately describe the NSDI process.

The re-scattering mechanism was originally proposed by Kuchiev [53]. A freed electron acts as an antenna by absorbing the fields energy while it oscillates in the field before returning and scattering with the ion. Its' energy is transfered to excite or even ionize a second electron. Corkum [21] expanded on this with his three-step model introduced in Section 1.4.

During the re-collision with the ion, the electron can recombine and emit high harmonic radiation or:

- the electron could be elastically scattered and further accelerated producing fast photoelectrons,

- the electron could be inelastically scattered with simultaneous excitation or the ionization of two electrons.

In experiments using circular polarized light instead of linearly polarized light, it was observed that the double emission was strongly suppressed [31]. It was concluded that the re-scattering process is predominantly responsible for NSDI by strong laser fields since the rotating electric field does not drive the field electron back to the parent ion [23].

Different theoretical approaches were undertaken in an effort to reproduce the main features of NSDI. The dynamics of the helium atom is given by two interacting electrons in the field of a heavy nucleus. The attractive Coulomb interactions between the nucleus and electrons and the Coulomb repulsion between the electrons make any analytical approach impossible as there is no solution to the full three-body problem to date.

In 1998, simulations of the three-dimensional time-dependent Schrödinger equation for helium in a strong field were undertaken by Taylor *et al* [80] which correctly predicted the simultaneous parallel emission of two electrons. However, at the time, it was an enormous numerical undertaking. Becker and Faisal used the time independent S-Matrix theory to reproduce the "knee" structure seen in the double ionization yields [13] and momentum distribution [12] for helium.

In 1993, the aligned-electron model was introduced in which the motion of the two electrons is restricted to one dimension within a regularized Coulomb potential [39]. It was used to study the correlated double ionization within the quantum picture [56, 87] and the classical picture [9, 45, 69]. The model qualitatively reproduced the increased double ionization yields where the SAE-approximation failed and confirmed the re-scattering scenario as the main mechanism in NSDI. However, within the model the Coulomb repulsion is over-estimated and the experimentally observed correlated escape in the momentum distributions could not be reproduced.

A decade ago, a reduced-dimensional model was introduced by Bruno Eckhardt and Krzysztof Sacha where the motion of each electron was restricted to one degree of freedom which lies symmetric to the field polarization axis allowing for simultaneous parallel escape [25, 27, 73]. Simulations using this model, within the quantum and classical picture, reproduced all features of the correlated electron escape [24, 26, 71, 72].

1.6 Electromagnetic Field as a Classical Field

The number of photons in each mode from a laser field used for observing multiphoton processes is very large. For example, a laser field generated by a Nd:YAG laser with photon energy $\hbar\omega = 1.17$ eV, intensity on the order of $I \sim 10^{12}$ Wcm^{-2} in a coherence volume of $V = \lambda^3$ ($\lambda = 2\pi c/\omega = 1064$ nm) has a number of photons equal to $N \simeq 2 \times 10^8$ [16]. In any configuration, the

parameter range for the external fields used in this thesis would amount to a minimum photon number of $N \simeq 2.3 \times 10^8$. Therefore, the laser field can be treated classically.

1.7 Structure and Aims of this Thesis

In the following chapter, the Hamiltonian for the helium atom is presented and the interaction with an electromagnetic field described. Chapter 3 introduces the $(1+1)$-dimensional model for the two-electron atom proposed by Bruno Eckhardt and Krzysztof Sacha [27]. In Chapter 4 and Chapter 5 the results of the two-electron trajectories in both a monochromatic driving field with a trapezoidal envelope and a sine-squared pulse are presented. A comprehensive statistical study was undertaken to illuminate the importance of the external field's frequency to the double ionization process. These results are presented in Chapter 6. In Chapter 7, quantum and semi-classical results from the same model are compared. Unless otherwise specifically indicated, atomic units were used throughout this thesis.

The aim of this work is to gain a better understanding of the internal dynamics of helium during the double ionization process. The applied methodology consists of varying parameters of the external driving field, for example angular frequency, amplitude and phase, and comparing two different driving fields. While a quantum treatment of the two-electron system is preferential when studying *final* momentum distributions and comparing them to those from experiments, they are not capable of illustrating the dynamics occurring *during* the ionization process. This way light is shed on the otherwise obscured processes occurring near the core. The progression of the electrons is followed from initial ionization to the re-scattering and ultimately to their final state.

Chapter 2

Helium Atom in an External Field

2.1 The Hamiltonian

A helium atom consists of a nucleus of mass m_n and charge number $Z = 2$, and two electrons with mass m_e and charge $-e$. The non-relativistic Hamiltonian is given by

$$H = \frac{\mathbf{p}_n^2}{2m_n} + \frac{\mathbf{p}_{e,1}^2}{2m_e} + \frac{\mathbf{p}_{e,2}^2}{2m_e} - \frac{2e^2}{|\mathbf{r}_{e,1} - \mathbf{r}_n|} - \frac{2e^2}{|\mathbf{r}_{e,2} - \mathbf{r}_n|} + \frac{e^2}{|\mathbf{r}_{e,1} - \mathbf{r}_{e,2}|}. \tag{2.1}$$

The position and momentum of the nucleus is given by $\mathbf{r}_n$ and $\mathbf{p}_n$ and $\mathbf{r}_{e,i}$ and $\mathbf{p}_{e,i}$ are the position and momentum of the electrons, respectively.

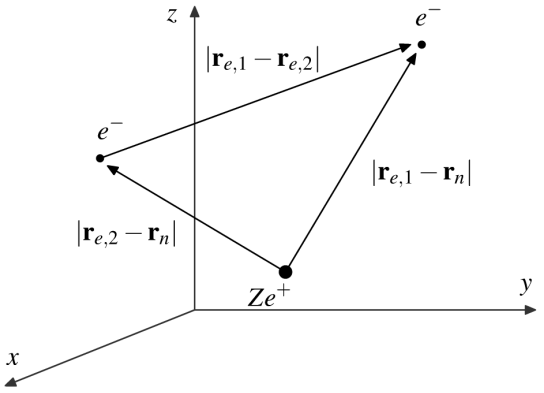

FIGURE 2.1: The helium atom with nuclear charge Ze resides at position $\mathbf{r}_n$. Two electrons are located at a distance of $|\mathbf{r}_{e,1} - \mathbf{r}_n|$ and $|\mathbf{r}_{e,2} - \mathbf{r}_n|$ from the nucleus at positions $\mathbf{r}_1$ and $\mathbf{r}_2$, respectively.

The internal dynamics of the atom can be separated from the center-of-mass motion by introducing center-of-mass coordinates

$$\mathbf{R} = \frac{1}{M}(m_n\mathbf{r}_n + m_e\mathbf{r}_{e,1} + m_e\mathbf{r}_{e,2}), \quad \mathbf{M} = m_n + 2m_e, \tag{2.2}$$

and using the relative coordinates

$$\mathbf{r}_i = \mathbf{r}_{e,i} - \mathbf{r}_n \tag{2.3}$$

which describe the distance of the electrons relative to the nucleus. Along with the corresponding momentum $\mathbf{P}$, the momenta of the nucleus and electrons transform to

$$\mathbf{p}_n = \frac{m_n}{M}\mathbf{P} - \mathbf{p}_1 - \mathbf{p}_2 \ , \ \mathbf{p}_{e,i} = \frac{m_e}{M}\mathbf{P} + \mathbf{p}_i. \tag{2.4}$$

The total kinetic energy in Equation 2.1 can be separated from the center-of-mass part, and the Hamiltonian describing the internal dynamics can be written as

$$H = \frac{\mathbf{p}_1}{2\mu} + \frac{\mathbf{p}_2}{2\mu} - \frac{Ze^2}{|\mathbf{r}_1|} - \frac{Ze^2}{|\mathbf{r}_2|} + \frac{e^2}{|\mathbf{r}_1 - \mathbf{r}_2|} + \frac{\mathbf{p}_1\mathbf{p}_2}{m_n}, \tag{2.5}$$

where $\mu = m_e m_n/(m_e + m_n)$ is the reduced mass.

The mass polarization term $\mathbf{p}_1\mathbf{p}_2/m_n$ is a consequence of the fact that the center-of-mass, Equation 2.2, does not coincide with the position of the nucleus $\mathbf{r}_n$. The nucleus of the helium atom is assumed to be infinitely heavy, $m_n \to \infty$, so that $\mu \to 1$. Then the mass polarization term is small and can be neglected [32].

The Hamiltonian which describes the inner structure of the helium atom is

$$H = \frac{\mathbf{p}_1^2}{2} + \frac{\mathbf{p}_2^2}{2} - \frac{2e}{|\mathbf{r}_1|} - \frac{2e}{|\mathbf{r}_2|} + \frac{e^2}{|\mathbf{r}_1 - \mathbf{r}_2|}. \tag{2.6}$$

The electrostatic attraction between the electron and the nucleus and the electrons' electrostatic repulsion are given by

$$V(\mathbf{r}_i) = -\frac{2e}{|\mathbf{r}_i|}, \tag{2.7a}$$

$$V_{1,2} = +\frac{e^2}{|\mathbf{r}_1 - \mathbf{r}_2|}, \tag{2.7b}$$

respectively.

2.2 Particle in an Electromagnetic Field

The Hamiltonian describing the interaction of a particle, with charge $-e$ and velocity $\mathbf{v}$ and an electromagnetic field is found by using the principle of "minimal coupling" [40]. The classical ansatz begins by finding Newton's equation via the Lorentz force and constructing the Lagrangian. In an electromagnetic field, the charged particle is subject to the Lorentz force,

$$\mathbf{F} = e[\mathbf{E} + \mathbf{v} \times \mathbf{B}]. \tag{2.8}$$

Using Newton's law, the equation of motion,

$$m\ddot{\mathbf{r}} = e[\mathbf{E} + \dot{\mathbf{r}} \times \mathbf{B}] \tag{2.9}$$

is determined.

For coherent fields, the potentials $\mathbf{A}$ and Φ are related to the electric and magnetic fields by

$$\mathbf{E}(\mathbf{r},t) = -\frac{\partial \mathbf{A}(\mathbf{r},t)}{\partial t} - \nabla\Phi(\mathbf{r},t) \tag{2.10a}$$

$$\mathbf{B}(\mathbf{r},t) = \nabla \times \mathbf{A}(\mathbf{r},t). \tag{2.10b}$$

They can be inserted into the Hamiltonian as real functions [46]. The minimal coupling Hamiltonian [20] reads

$$H_{mc} = \frac{1}{2}[\mathbf{p} + e\mathbf{A}(\mathbf{r},t)]^2 - e\Phi(\mathbf{r},t). \tag{2.11}$$

The canonical momentum is replaced by the mechanical (or kinematical) momentum,

$$\mathbf{p} \to \mathbf{p} + e\mathbf{A}(\mathbf{r},t) \tag{2.12}$$

and the potential is shifted by $-e\Phi(\mathbf{r},t)$ [40]. The fields $\mathbf{E}$ and $\mathbf{B}$ are still inherent in the Hamiltonian even though they are expressed by the potentials $\mathbf{A}$ and Φ.

2.3 One-Electron Atom in an Electromagnetic Field

The Hamiltonian for a one-electron atom with nucleus of charge Ze and infinite mass and an electron with charge $-e$ interacting with an electromagnetic field includes the electrostatic Coulomb potential, Equation 2.7a, between the electron and nucleus [16],

$$H = \frac{1}{2}[\mathbf{p} + e\mathbf{A}(\mathbf{r},t)]^2 + V(\mathbf{r}) - e\Phi(\mathbf{r},t). \tag{2.13}$$

Coulomb Gauge

Within the Coulomb gauge, the electromagnetic plane wave fields are described by vector potentials [46]. Assuming no sources are present the electrostatic potential may be set to zero,

$$\nabla \cdot \mathbf{A} = 0 \ , \ \Phi = 0. \tag{2.14}$$

The Hamiltonian, Equation 2.11, in Coulomb gauge becomes

$$H = \frac{\mathbf{p}^2}{2} + V(\mathbf{r}) - \mathbf{p} \cdot \mathbf{A}(\mathbf{r},t) + [\mathbf{A}(\mathbf{r},t)]^2 = H_0 + H_{int}, \tag{2.15}$$

with

$$H_0 = \frac{\mathbf{p}^2}{2} + V(\mathbf{r}), \tag{2.16a}$$
$$H_{int} = -\mathbf{p} \cdot \mathbf{A}(\mathbf{r},t) + [\mathbf{A}(\mathbf{r},t)]^2. \tag{2.16b}$$

The first term in H_{int} on the right hand side is treated as a time-dependent potential. If H_{int} is averaged over an integral number of optical cycles of the electromagnetic field, the A^2-term is equal to the ponderomotive energy Equation 1.7 associated with the quiver motion of the electron in the field [17].

In the Coulomb gauge, physical fields may be expressed in terms of the vector potential and can be written as a set of plane waves [76],

$$\mathbf{A}(\mathbf{r},t) = A_0 \hat{\varepsilon} \left[\mathrm{e}^{i(\mathbf{kr}-\omega t)} + \mathrm{e}^{-i(\mathbf{kr}-\omega t)} \right], \tag{2.17}$$

oscillating in time at an angular frequency ω and propagating in space along a wave vector $\mathbf{k}$ with a spatial period $\lambda = 2\pi/|\mathbf{k}|$. The amplitude of the wave, A_0, is directed along the field polarization vector, $\hat{\varepsilon}$, with $\mathbf{k} \perp \hat{\varepsilon}$. Applying Equation 2.10, it follows

$$\mathbf{E}(\mathbf{r},t) = -\frac{\partial \mathbf{A}(\mathbf{r},t)}{\partial t} = i\omega A_0 \hat{\varepsilon} \left[\mathrm{e}^{i(\mathbf{kr}-\omega t)} - \mathrm{e}^{-i(\mathbf{kr}-\omega t)} \right], \tag{2.18a}$$
$$\mathbf{B}(\mathbf{r},t) = \nabla \times \mathbf{A}(\mathbf{r},t) = i(\mathbf{k} \times \hat{\varepsilon}) A_0 \left[\mathrm{e}^{i(\mathbf{kr}-\omega t)} + \mathrm{e}^{-i(\mathbf{kr}-\omega t)} \right]. \tag{2.18b}$$

The unit vector along the magnetic field polarization is $\hat{b} = \mathbf{k} \times \hat{\varepsilon}/|\mathbf{k}| = \hat{k} \times \hat{\varepsilon}$. The prefactors are defined as [20]

$$i\omega A_0 = \frac{E_0}{2}, \tag{2.19a}$$
$$i|k|A_0 = \frac{B_0}{2}. \tag{2.19b}$$

2.4 Dipole Approximation

Within the dipole approximation, the optical field has a wavelength much larger than the maximal extension of the atom[1].

The terms in the Hamiltonian which describe the interaction with the field become independent on the position of the particle. The exponential in the vector potential which describes the spatial dynamics is expanded and approximated by its leading term [20]

$$\mathrm{e}^{\pm i\mathbf{kr}} \approx 1. \tag{2.20}$$

The vector potential is then given by

$$\mathbf{A}(t) = A_0\hat{\boldsymbol{\varepsilon}}\left(\mathrm{e}^{-i\omega t} + \mathrm{e}^{i\omega t}\right). \tag{2.21}$$

The two gauges introduced in the next sections are both within the dipole approximation.

Velocity Gauge

The dipole approximation has an impact on the vector potential, $\mathbf{A}(\mathbf{kr},t) \to \mathbf{A}(t)$, which in turn causes a time-dependent shift of the momentum in the Hamiltonian. The velocity gauge is a Coulomb gauge where the dipole approximation is used. Inserting Equation 2.21 into H_{int} leads to

$$H_{int} = \mathbf{p}A_0\hat{\boldsymbol{\varepsilon}}\left(\mathrm{e}^{i\omega t} - \mathrm{e}^{-i\omega t}\right), \tag{2.22}$$

and along with Equation 2.19a, the interaction Hamiltonian in velocity gauge is

$$H_{int} = \mathbf{p}\cdot\mathbf{A}(t) \;\text{ with }\; \mathbf{A}(t) = A_0\,\hat{\boldsymbol{\varepsilon}}\,\sin(\omega t) \tag{2.23}$$

with $A_0 = E_0/\omega$ the amplitude of the vector potential, E_0 the electric field strength, and ω the field frequency.

Length Gauge

Applying a gauge transformation with the scalar field [40]

$$\chi(\mathbf{r},t) = -\mathbf{r}\cdot\mathbf{A}(t) \tag{2.24}$$

[1] A laser with an intensity $I = 3.5\times10^{14}\mathrm{W/cm^2}$ and wavelength $\lambda = 800$ nm ($\omega = 0.057$ a.u.) irradiates hydrogen with $I_p = 0.5$ a.u. from the ground state. The maximal excursion of the electron is then $\alpha = F_0/\omega^2 = 30.8$ a.u. $= 1.83$ nm. [8]

results in transformed potentials

$$A' = 0, \tag{2.25a}$$
$$\Phi' = -\frac{\partial \chi(\mathbf{r},t)}{\partial t} = -\mathbf{r}E_0\cos(\omega t). \tag{2.25b}$$

Insert Φ' into Equation 2.11 and the corresponding interaction Hamiltonian in length gauge is,

$$H'_{int} = \mathbf{r}\cdot\mathbf{E}(t) \text{ with } \mathbf{E}(t) = E_0\,\hat{\boldsymbol{\varepsilon}}\cos(\omega t). \tag{2.26}$$

A characteristic of the Hamiltonian in length gauge is the direct coupling of the laser field to the unperturbed Coulomb potential. This leads to the time-dependent spatial deformation of the target atoms' potential. The physical implications of this have already been alluded to in the previous chapter. It is the electric field which plays a large role in ionization and governs the electrons' trajectory in the field.

2.5 Helium in an Electromagnetic Field

The resulting Hamiltonian for helium in velocity gauge is

$$H = \frac{\mathbf{p}_1^2}{2} + \frac{\mathbf{p}_2^2}{2} - \frac{2}{|\mathbf{r}_1|} - \frac{2}{|\mathbf{r}_2|} + \frac{1}{|\mathbf{r}_1-\mathbf{r}_2|} + (\mathbf{p}_1+\mathbf{p}_2)\,\mathbf{A}(t). \tag{2.27}$$

The Hamiltonian for helium in length gauge is

$$H = \frac{\mathbf{p}_1^2}{2} + \frac{\mathbf{p}_2^2}{2} - \frac{2}{|\mathbf{r}_1|} - \frac{2}{|\mathbf{r}_2|} + \frac{1}{|\mathbf{r}_1-\mathbf{r}_2|} + (\mathbf{r}_1+\mathbf{r}_2)\,\mathbf{E}(t). \tag{2.28}$$

The length and velocity gauge differ by a total time-derivative. Any measurable quantities must be independent of the gauges used. In the length gauge, the velocity of the electron is the same as the canonical momentum. In the velocity gauge, the momentum of an electron is given by Equation 2.12. The vector potential is found by

$$\mathbf{A}(t) = -\int_0^{t_d} \mathbf{E}(\tau)\mathrm{d}\tau. \tag{2.29}$$

The value of $\mathbf{A}(t)$ is equal to the integral over the electric field in the interval $t \in [0,t_d]$, specifically the direct current (or dc-) component of the electric laser field[2]. If $\mathbf{A}(t=t_d)$ is not zero the pulse transfers a momentum linear in $\mathbf{A}$ (with $\mathbf{A} \parallel \mathbf{E}, \mathbf{A} \perp \mathbf{k}$) to a charged particle in the field [15].

[2]Observe the Fourier transform of the electric field $\mathbf{E}(\omega) = \int_0^{t_d} \mathrm{e}^{i\omega\tau}E(\tau)\mathrm{d}\tau$. In this representation, $\mathbf{A}(t)$ corresponds to the negative frequency component at zero-frequency ($\omega = 0$). A real laser pulse does not have such a component as $\omega = 0$ implies $\mathbf{k} = 0$, and $\mathbf{E}(t)$ in Equation 2.26 would be constant [61].

Chapter 3

Model

In an intense linearly polarized external field, the Coulomb potential of the one-dimensional helium atom bends proportionally to the strength of the field applied and a Stark saddle emerges. An analysis of classical pathways to non-sequential double ionization revealed the highly symmetric configuration of both electrons as they simultaneously cross the saddle point [25]. While propagating away from the nucleus, their mutual repulsion must be compensated by their Coulomb attraction to the core. Any deviation from this symmetry would result in one electron being pulled back to the nucleus as the second electron is pushed over the saddle.

The Hamiltonian of two electrons in six-dimensional phase space with position $\mathbf{r}_i = (x_i, y_i, z_i)$ and momentum $\mathbf{p}_i$ for $i = 1, 2$ and a static electric field $F_0 > 0$ parallel to z-direction is given by

$$H = \sum_{i=1}^{2} \left\{ \frac{\mathbf{p}_i^2}{2} - \frac{2}{|\mathbf{r}_i|} \right\} + \frac{1}{|\mathbf{r}_1 - \mathbf{r}_2|} - F_0 \, (\mathrm{z}_1 + \mathrm{z}_2). \tag{3.1}$$

In the saddle configuration, the motion of both electrons is restricted to one-dimensional lines which lie at a constant angle to the field polarization axis z as shown in Figure 3.1 *a*). The electrons positions in the z-x-plane are $(x_1, 0, z_1)$ and $(-x_2, 0, z_2)$. The saddle points are found in the symmetric subspace $x_1 = x_2$, $z_1 = z_2$ at

$$x_s = \pm 3^{\frac{1}{4}}/(2\sqrt{F_0}), \quad z_s = 3^{\frac{3}{4}}/(2\sqrt{F_0}), \tag{3.2}$$

with potential energy

$$V_s = -3^{\frac{3}{4}} \, 2\sqrt{F_0}. \tag{3.3}$$

In the case of a time-dependent external field, the saddle point moves along a constant line $z_s/x_s = \pm\sqrt{3}$. Since simultaneous parallel electron escape occurs near the saddle points, the motion of each electron is restricted to new coordinates fulfilling $z_i/x_i = \pm\sqrt{3}$ which run at an

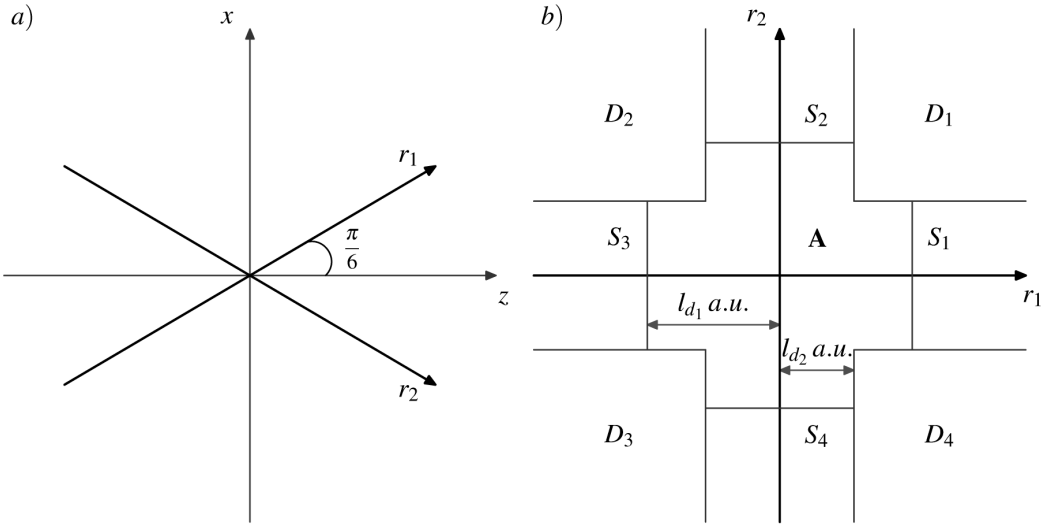

FIGURE 3.1: *a*) Two-dimensional geometry of the model. In the z-x-plane, the motion of electrons 1, 2 is restricted to r_1, r_2 which lie at a constant angle $\pi/6$ to the field polarization axis z. *b*) the configuration space in the new coordinate system is subdivided into sections corresponding to the neutral atom **A**, and the single S_i and double D_i ionization channels. In the quantum picture, $l_{d_1} = 12.5$ a.u. and $l_{d_2} = 7$ a.u. In the classical picture, l_{d_1} and l_{d_2} will vary with the external field frequency (see Section 3.5 and Chapter 7 for further clarification).

angle $\pm\pi/6$ relative to the field axis. Each electron has a single degree of freedom given by r_1 and r_2, with

$$x_1 = -\frac{1}{2}r_1\,,\;\; z_1 = \frac{\sqrt{3}}{2}r_1 \;\;\text{and}\;\; x_2 = \frac{1}{2}r_2\,,\;\; z_2 = \frac{\sqrt{3}}{2}r_2. \tag{3.4}$$

This configuration ensures the simultaneous parallel escape while not over-emphasizing the Coulomb repulsion between the electrons. The Hamiltonian in the new coordinates in length gauge is

$$H = \frac{p_1^2}{2} + \frac{p_2^2}{2} - \frac{2}{|r_1|} - \frac{2}{|r_2|} + \frac{1}{\sqrt{(r_1 - r_2)^2 + r_1 r_2}} - F(t)\,\frac{\sqrt{3}}{2}\,(r_1 + r_2). \tag{3.5}$$

The time-dependent driving field $F(t)$ is described in more detail in Section 3.4.

To circumvent numerical problems due to singularities from the Coulomb interactions, a cut-off factor $\varepsilon = 0.6$ a.u. is added to the Coulomb potentials,

$$\frac{1}{|r_i|} \to \frac{1}{\sqrt{r_i^2 + \varepsilon}}. \tag{3.6}$$

This results in the quantum mechanical ground state energy of the unperturbed helium atom $E_0 = -2.83$ a.u. [71].

3.1 Initial Conditions

In the quantum description of Corkum's three-step model, tunneling is the first step in the sequence. The actual tunneling time has been determined to be small (< 100 as) [28] and, in the case of helium[1], independent of the laser peak intensity. The tunneling time is less than 4 a.u..

In the classical representation, there is no tunneling. Therefore, it is assumed *ab initio* that an electron began to tunnel just before the field reaches a maximum. When the external field has reached the maximum, the "tunneled" electron emerges from the potential barrier with zero momentum. The numerical simulations start from this initial situation, as illustrated in Figure 3.2 b). Here, the effect of the field maximum at the time t_0 on the Coulomb field is represented by the red line. The bound electron is found between the two classical turning points within the potential well (blue line) and the field electron directly outside the potential (blue dot).

The total energy of the system is equal to the ground state energy of helium and it is shared between both electrons equally. In determining the initial conditions, the field parameters are fixed. The amplitude of the field maximum at t_0 influences the initial conditions of both electrons since it directly affects the distortion of the potential field.

From the conservation of energy in the system, the conjugated momentum for the bound electron is determined. The one-parameter ensemble of initial conditions for the bound electron is then constructed along the the ground state energy shell in phase space, illustrated in blue in Figure 3.2 a). The negative momentum indicates the direction the electron is traveling.

For constant field strength, the initial conditions for the field electron are the same. They start from the same position $r_{1,0}$, just beyond the barrier, and with zero momentum $p_{1,0} = 0$. The only variables are the initial conditions of the bound electrons.

A non-linear system is characterized by its sensitivity to initial conditions. To make a qualitative statement about the initial conditions of the bound electrons in phase space, the interval between the initial conditions must be sufficiently small to ensure the continuity of the final states in phase space. These initial conditions are not randomly chosen but equally spaced and calculated in sequence.

[1] Helium, in the presence of a strong laser field, has a smaller polarizability and therefore experiences a smaller Stark shift and laser-induced dipole moment than is the case, for example, in argon. Therefore, the intensity dependent tunneling time is small.

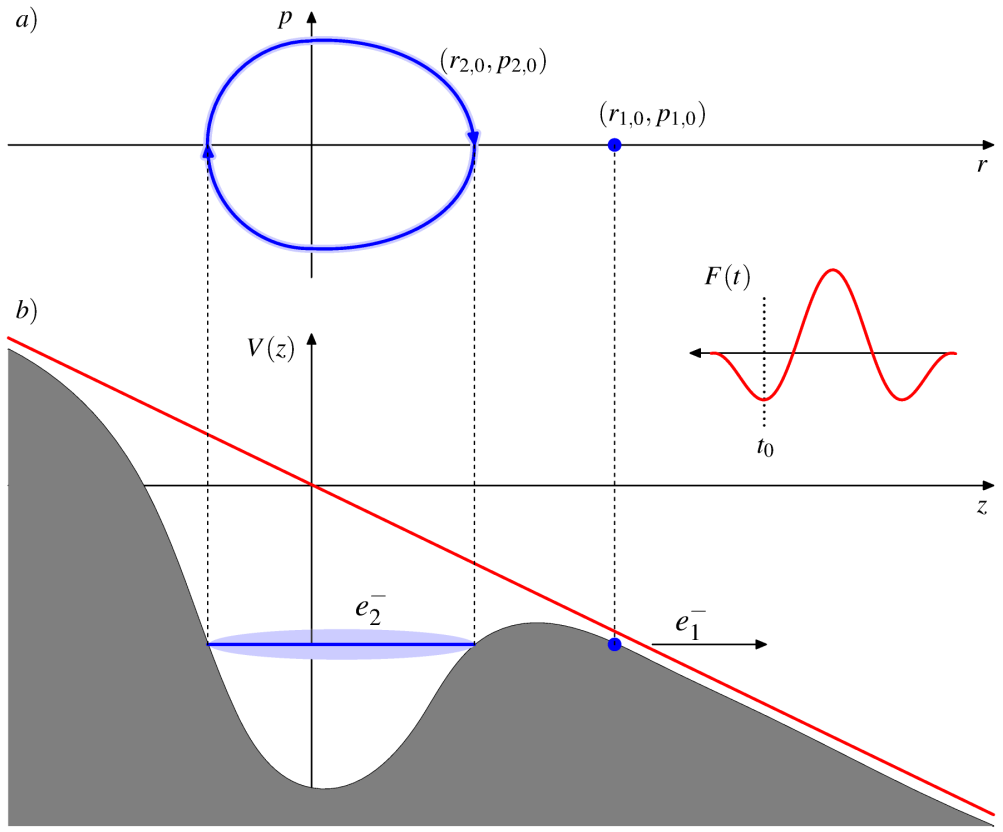

FIGURE 3.2: Determining the initial conditions of the two electrons. a) the initial conditions for each electron in phase space. The initial conditions for the bound electron are found along the energy shell. Further along the r-axis for $p = 0$, the initial conditions for the field electron are found. b) a rough illustration of the smoothed Coulomb potential in the presence of a laser field with a maximum at t_0 (shown in red). The field electron is found on the other side of the Stark barrier. At the beginning of the simulation, it will travel down the potential hill until the following field maximum. There, it turns and will accelerate back towards the nucleus. The bound electron can be found at any position between the two classical turning points within the potential.

The divergence between the final positions of the bound electrons λ relative to the decreasing distance between the initial positions of the bound electron Δn is plotted in Figure 3.3. One set of initial conditions for a bound electron remained unchanged because in the parameter combination used in the simulations they lead to double ionization. For Figure 3.3, two cases from each hemisphere of the energy shell were calculated and compared for $p_{2,0} > 0$ (magenta) and $p_{2,0} < 0$ (turquoise).

For large distances between neighboring initial conditions, the control trajectory represents double ionization while the second trajectory shows single ionization. Decreasing Δn closes the gap between two neighboring initial positions. The second trajectory transitions from single ionization to double ionization. For $\Delta n \lesssim 5 \times 10^{-5}$, the divergence λ is stable in both cases. The ensemble size used in this work for most statistical calculations, including ionization yields, is 2×10^5 initial conditions which, depending of the peak field amplitude, means $\Delta n \geq 2 \times 10^{-5}$

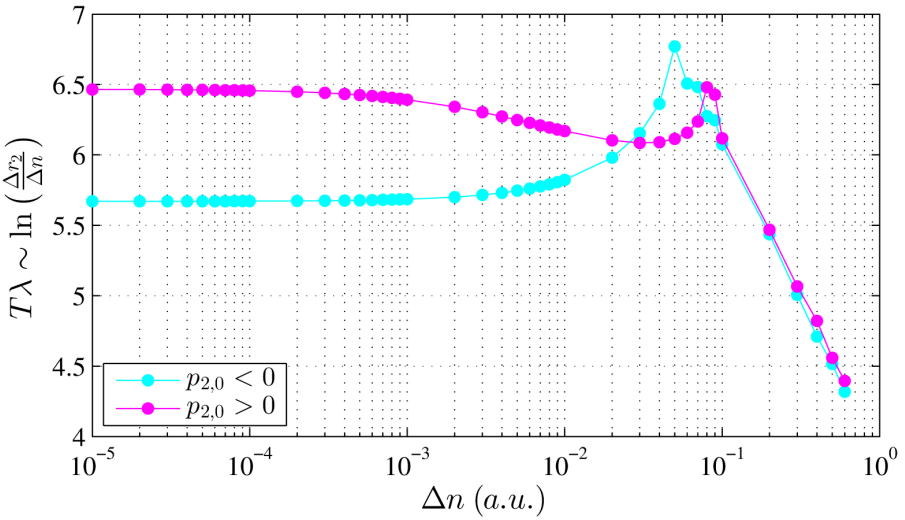

FIGURE 3.3: A semilogarithmic plot of the divergence λ between two neighboring trajectories for the bound electron whose initial positions have varying interval size Δn. The initial conditions of the bound electrons are found on the upper hemisphere of the energy shell, $p_{2,0} > 0$ (magenta), and in the second case they are found on the lower hemisphere of the energy shell, $p_{2,0} < 0$ (turquoise). Each case consists of the transition from single to double ionization with decreasing distances between neighboring initial conditions.

a.u..

An aim of this research is to identify some signature in phase space can be found which predisposes a trajectory to later participate in successful double ionization.

3.2 Energy

Since there are multiple ways to define the one-particle energies, arguments shall be made for two appropriate definitions at $F(t_{end}) = 0$. Firstly, the Coulomb interaction term is divided equally between both electrons,

$$\tilde{E}_1 = \frac{p_1^2}{2} - \frac{2}{\sqrt{r_1^2+\varepsilon}} + \frac{1}{2}\frac{1}{\sqrt{(r_1-r_2)^2+r_1r_2+\varepsilon}}, \tag{3.7a}$$

$$\tilde{E}_2 = \frac{p_2^2}{2} - \frac{2}{\sqrt{r_2^2+\varepsilon}} + \frac{1}{2}\frac{1}{\sqrt{(r_1-r_2)^2+r_1r_2+\varepsilon}}. \tag{3.7b}$$

This is advantageous because no modifications have to be made for the final energy $\tilde{E}_{tot} = \tilde{E}_1 + \tilde{E}_2$. This definition was used by Wasson and Koonin [86] and would arguably be the most suitable in the case of parallel electron escape.

In the second case, the energy of each electron is calculated as

$$E_1 = \frac{p_1^2}{2} - \frac{2}{\sqrt{r_1^2+\varepsilon}} + \frac{1}{\sqrt{(r_1-r_2)^2+r_1r_2+\varepsilon}}, \tag{3.8a}$$

$$E_2 = \frac{p_2^2}{2} - \frac{2}{\sqrt{r_2^2+\varepsilon}} + \frac{1}{\sqrt{(r_1-r_2)^2+r_1r_2+\varepsilon}}. \tag{3.8b}$$

The total energy is then

$$E_{tot} = E_1 + E_2 - \frac{1}{\sqrt{(r_1-r_2)^2+r_1r_2+\varepsilon}}. \tag{3.9}$$

The full value of the Coulomb interaction is present in both single-particle energies. This definition is ideal in the case of single ionization and anti-parallel double ionization, the interaction term goes to zero when the electrons are far away from each other.

The second definition for the single-particle energies, 3.8b, is used here. However, the following must be considered in subsequent calculations. During simultaneous parallel escape, the Coulomb repulsion is shared between the electrons. An electron is considered to be ionized when $E_i(t_{end}) > 0$ for $i = 1,2$. This can be misleading as can be seen in the figures in Section 3.5.1. All values in the plots are calculated using the individual energies with the full Coulomb repulsion (Equation 3.8a, Equation 3.8b) and in the final energy it is subtracted, see Equation 3.9.

3.3 Equations of Motion

Hamilton's equations determine the time evolution of the states of each electron,

$$\dot{r}_i = \frac{\partial H}{\partial p_i}, \quad \dot{p}_i = -\frac{\partial H}{\partial r_i}, \tag{3.10}$$

for $i = 1, 2$. This results in the coupled non-linear differential equations

$$\dot{r}_1 = p_1, \tag{3.11a}$$

$$\dot{p}_1 = \frac{2r_1 - r_2}{2\left((r_1-r_2)^2+r_1r_2+\varepsilon\right)^{\frac{3}{2}}} - \frac{2r_1}{(r_1^2+\varepsilon)^{\frac{3}{2}}} + \frac{\sqrt{3}}{2}F(t), \tag{3.11b}$$

$$\dot{r}_2 = p_2, \tag{3.11c}$$

$$\dot{p}_2 = \frac{2r_2 - r_1}{2\left((r_1-r_2)^2+r_1r_2+\varepsilon\right)^{\frac{3}{2}}} - \frac{2r_2}{(r_2^2+\varepsilon)^{\frac{3}{2}}} + \frac{\sqrt{3}}{2}F(t), \tag{3.11d}$$

where the external field is represented either by Equation 3.12 or Equation 3.15. Numerical integration for each set of initial conditions yields the coordinate and momentum for each electron.

The equations of motion were integrated numerically using a fourth/fifth-order Runge-Kutta method both in a Matlab script, which generated data to the electron trajectories, and a C-scripted program, which was implemented to calculate ionization yields from fields with varying amplitude, frequency, and phase. Adaptive step-size was used, particularly due to the $1/r$-potential. The initial positions of the electrons were found using bisection and interpolation methods in Matlab.

3.4 Time-Dependent External Field

Two different external driving fields were applied to the two-electron system. The field's envelope will prove to have a significant influence on the progress of the electrons as they ionize.

3.4.1 Driving Field with a Trapezoidal Envelope

A trapezoidal-shaped pulse envelope is constructed about a monochromatic electric field which ensures that the zero-frequency condition is fulfilled. The full electric field is given by

$$F(t) = \mathfrak{f}(t)\cos\omega t\,\varepsilon_z, \tag{3.12}$$

with the trapezoidal envelope,

$$\mathfrak{f}(t) = F_0 \begin{cases} \frac{1}{n}\frac{\omega}{2\pi}t & \text{for } 0 \le t \le n\frac{2\pi}{\omega} \\ 1 & \text{for } n\frac{2\pi}{\omega} \le t \le (N-n)\frac{2\pi}{\omega} \\ \frac{1}{n}\left(N - \frac{\omega}{2\pi}t\right) & \text{for } (N-n)\frac{2\pi}{\omega} \le t \le N\frac{2\pi}{\omega}. \end{cases} \tag{3.13}$$

The total number of optical cycles is $N = 14$, where $n = n' = 2$ are the ramp-on and ramp-off cycles respectively, see Figure 3.4.

Numerical calculations using this pulse begin at the first maximum after the 2-cycle ramp-on.

3.4.2 Driving Field with a Sine-Squared Envelope

The vector potential of the external field and its' envelope, as shown in [26], are given by

$$A(t) = a(t)A_0\sin^2(\omega(t - t_d/2) + \phi), \tag{3.14a}$$

$$a(t) = \cos^2(\pi/t_d(t - t_d/2)). \tag{3.14b}$$

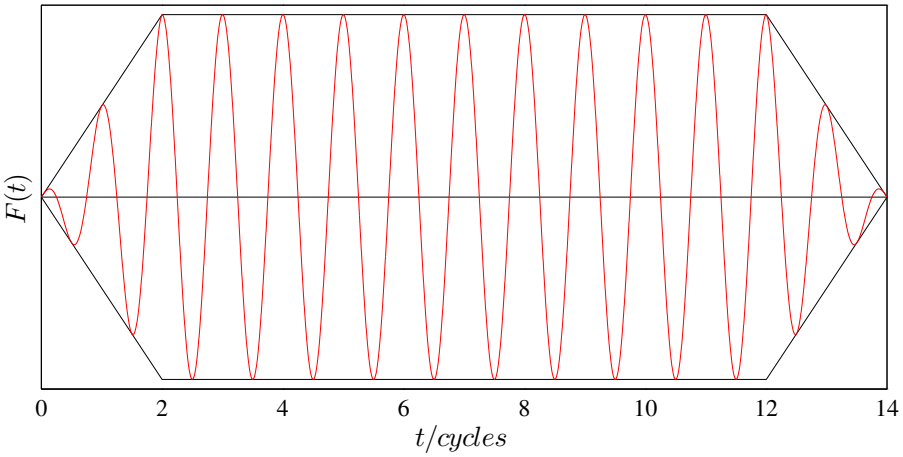

FIGURE 3.4: A trapezoidal envelope with a 14-cycle external field with a two-cycle ramp-on/ramp-off and ten-cycle plateau. This pulse shape is used to simulate a constant monochromatic external field.

The pulse duration is $t_d = \frac{2\pi n}{\omega}$, for now $n = 1$. To get the external field, use

$$F(t) = -\frac{\partial A(t)}{\partial t} \tag{3.15}$$

to get

$$F(t) = \mathrm{F}_0 \cos\left(\frac{\omega(t - t_d/2)}{2}\right) \cos\left(\frac{3\omega(t - t_d/2)}{2} + \phi\right) \tag{3.16}$$

with $A_0 = \frac{F_0}{\omega}$. An illustration of such a pulse using five different phases is given in Figure 3.5.

When using this pulse shape the numerical calculations begin at the first field maximum.

Ideally, a pulse used in computer simulations ought to resemble those used in experiments, or at least be experimentally feasible. The vector potential must vanish at the end of the pulse. If

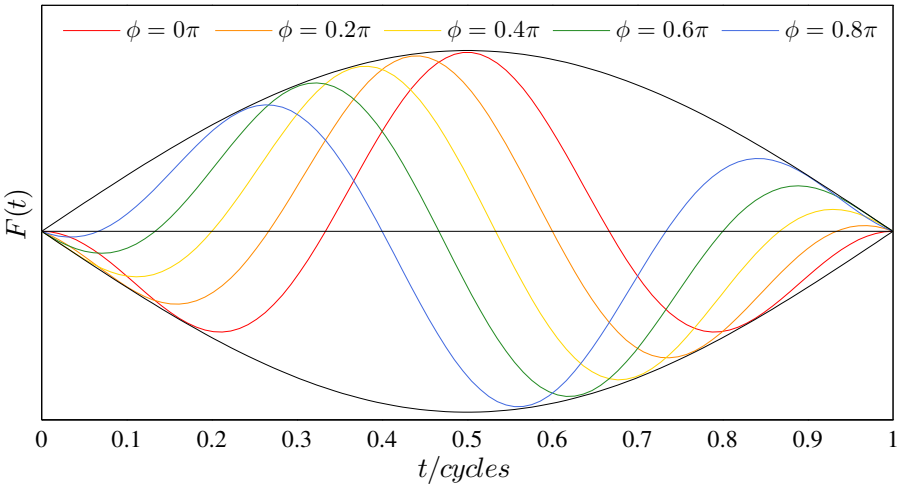

FIGURE 3.5: Single-cycle laser pulse with a sine-squared envelope for different phases, $\phi = 0,\ 0.2\pi,\ 0.4\pi,\ 0.6\pi,\ 0.8\pi$.

a linearly polarized field is defined by its vector potential and includes a squared envelope, the zero-net-force condition is automatically satisfied.

3.4.3 Pulse Duration

For longer pulses, ionization dynamics are not contingent on the pulse form and number of cycles [44]. A monochromatic electric field represented by Equation 2.26 is a reasonable approximation for pulses which have ten or more cycles ([77] and references within). It was used extensively for semi-classical numerical simulations over a decade ago [19, 34, 50].

The effects of the leading and trailing edges are neglected. Quantum mechanical effects such as interference and wave-packet spreading are washed-out. The phase ϕ of the wave has no physical significance [63]. However, to calculate ionization yields an envelope function must be used to ensure a finite laser pulse.

The more modern pulses used in simulations are similar to those made in the laboratory. The ionization dynamics from short pulses are heavily influenced by laser pulse shape and the carrier envelope phase (CEP) [5, 91].

3.4.4 Field Parameters

To understand the dynamics of the electrons mutual' behavior while exposed to an external pulse, there are four field parameters that are individually varied. These are the peak field amplitude, field frequency, and, for a pulse with a sine-squared envelope, phase and tunneling maximum.

The choice of field amplitudes is not arbitrary. They lie where the "knee" structure in the NSDI yields emerges. It is in this domain where the correlated nature of simultaneous electron escape is preserved and observable in a classical picture.

The amplitude of the field directly influences the initial conditions due to the bending the Coulomb potential of the atom. While the ground state energy is constant, the strength of the Stark saddle increases and the shell upon which all initial conditions lie contracts, and visa versa. It is crucial that the saddle point never sinks below the binding energy of the inner electron. Otherwise, the bound electron may just drift out of the potential well and the correlated nature of the double ionizing sequence would be lost. While using the external field with sine-squared envelope, the maximum field strength was capped at $F = 0.3$. This ensured that the largest maximum of the external field did not bend the potential well lower than the binding energy of the inner electron.

The frequency is another field parameter. It determines the extension of the electrons in the field. A small frequency results in a rather large orbit of the re-scattering electron while a large frequency reduces the time spent in the field enormously. This in turn effects the energy gained by the electron in the field as $U_p \sim \omega^{-2}$.

A high frequency field travels fast across the atom and also affects the "time" the electrons have to doubly ionize. For a high-frequency few-cycle pulse with a sine-squared envelope, the pulse might be zero before the field electron can return back to the parent ion. Furthermore, the frequency affects the pulse duration. Simulations using small frequencies need to run much longer as the electrons need longer to travel further distances, i.e. to ionize.

In the semi-classical studies, the field maxima (especially in the sine-squared external field) at which the simulation commences will prove to be important. For a trapezoidal pulse shape, the amplitude in the plateau has equal magnitude. Therefore, the saddle points on both sides of the potential well are of equal height. All calculations begin at a peak maximum. However, the amplitudes of consecutive maxima of pulses with the sine-squared envelope are unequal and the symmetry is broken.

3.5 Ionization

The conditions of double ionization are introduced in this section. When the field is turned off and a period of stabilization time has passed, electrons are considered ionized when two criteria are met. Firstly, their single-particle energies must be positive even after very long stabilization times. The former are given in Equation 3.8. Secondly, the distance of both electrons must exceed some predetermined value ($l_d = X$ a.u.), ideally corresponding to the experimental design.

In the experimental setup (see COLTRIMS [89]), electrons are accelerated in a homogeneous electric field supplemented with a light magnetic field after ionization.

Wasson used a distance of $l_d = 4$Å which corresponds to a distance of $l_d = 7.56$ a.u. [86]. Guo *et al* set their boundary at $l_d = 6$ a.u. for calculations using a field with a frequency of $\omega = 0.4$ a.u.[41]. Watson implemented distances of $l_d = \pm 12.5, \pm 25$ a.u. for calculations using a field with frequency $\omega = 0.057$ a.u.. A distance criteria of $l_d = 30$ a.u. was used for simulations using a field frequency of $\omega = 0.584$ [62]. The evolution of these numbers underline the true value of a classical trajectory analysis.

The time from the field electrons' impact until both electrons' final ionization behavior depends on the field's frequency. For a high-frequency pulse, the full ionization sequence occurs relatively quickly. For a low-frequency field, the electrons travel long distances during the ionization process and stabilization.

A lightly bound electron performs sweeping oscillations across the nucleus. If the cut-off is smaller than the extension of its oscillation, then the whole event could be (wrongly) classified as double ionization. In obtaining classical double ionization yields, a distance criteria of $l_d = 70$ a.u. was implemented in addition to the energy criterion.

For calculation times coinciding with the electrons' field-free excursion, the electrons travel a long time with the attractive force of the nucleus being the only force acting on them. For anti-parallel double ionization, the interaction term goes to zero and the kinetic energy of both electrons is greater than the attractive force of the nucleus (see Section 3.5.1 for further details). Only then do *true* trajectories emerge.

3.5.1 True Trajectories

Individual trajectories in the (1+1)-dimensional configuration space describe the position of both electrons relative to each other. The figures in Table 3.1 illustrates the importance of the stabilization cycles. The figures are generated by the excitation of two electrons by a single-cycle sine-squared pulse of the form seen in Figure 3.5. Their subsequent field-free propagation is measured in multiples of field cycles. The peak field amplitude is $F = 0.30$ a.u. and frequency and phase are $\omega = 0.15$ a.u. and $\phi = 0$ a.u. respectively.

TABLE 3.1: A series of figures with *a)* two-electron trajectories in the (1+1)-dimensional configuration space and momentum distribution (inset) and *b)* final energy values for the initially bound electron (x E_1), re-colliding electron ($+$ E_2) and their sum ($\triangle$ E_{tot}). The field parameters used were $F = 0.30$ a.u., $\omega = 0.15$ a.u., and $\phi = 0$ a.u.. The final number of field cycles $t_f = 1, 2, 5, .., 200$ the electrons could travel field-free is given in the left column. The color scheme, blue-to-red, is a reference to the sequence in which neighboring initial conditions are calculated. Further details are found in the text.

t_f (in cycles)	*a)* Configuration space	*b)* Final energy
$t_f = 1$	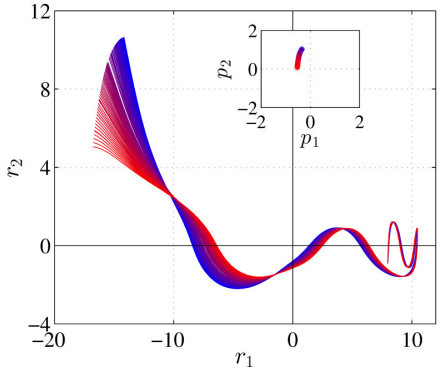	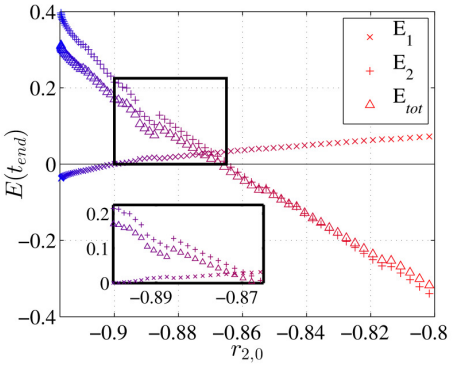

Continued on next page

Table 3.1 – *Continued from previous page*

t_f (in cycles)	*a)* **Configuration space**	*b)* **Final energy**
$t_f = 2$	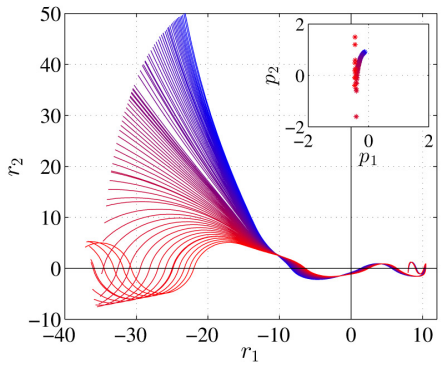	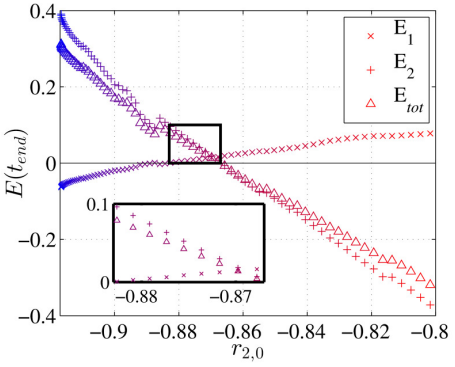
$t_f = 5$	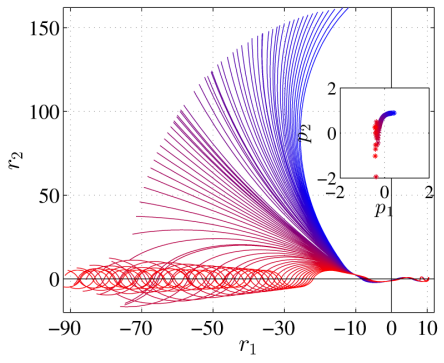	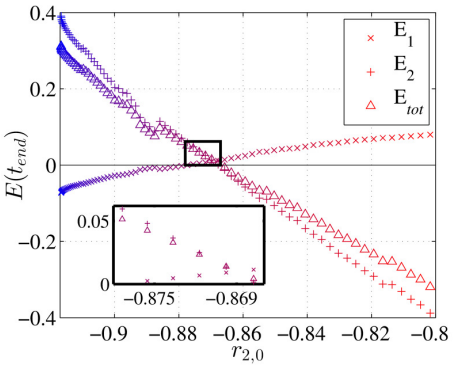
$t_f = 10$	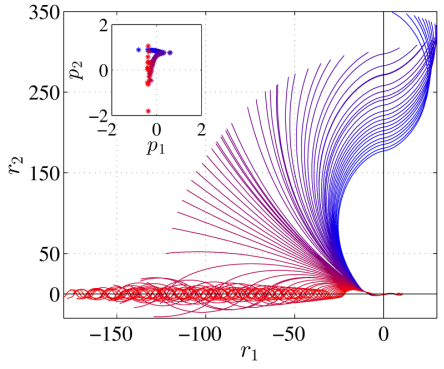	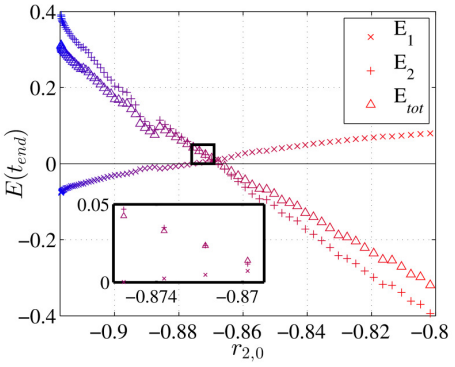
$t_f = 20$	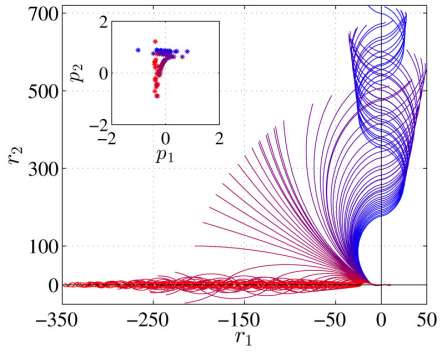	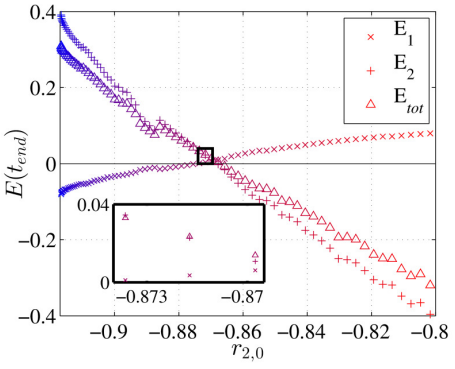

Continued on next page

Table 3.1 – *Continued from previous page*

t_f (in cycles)	*a)* **Configuration space**	*b)* **Final energy**
$t_f = 50$	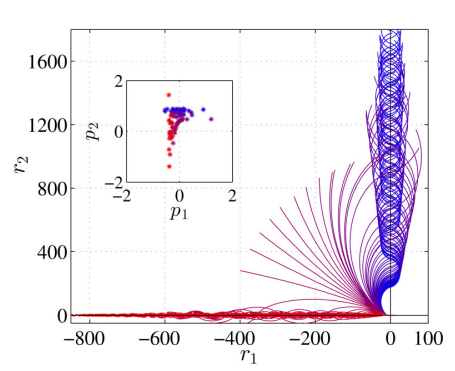	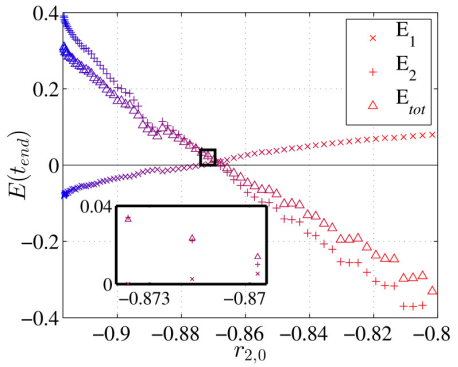
$t_f = 100$	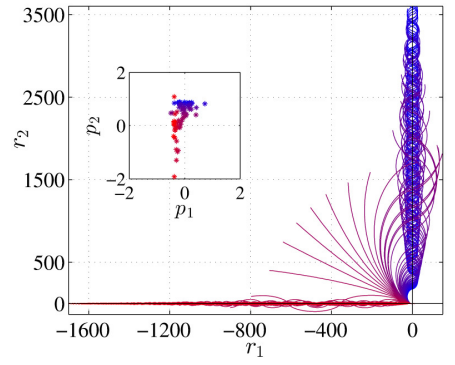	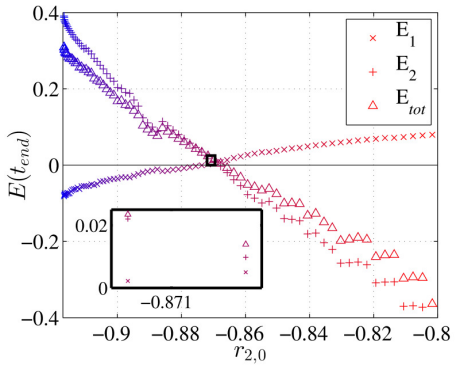
$t_f = 200$	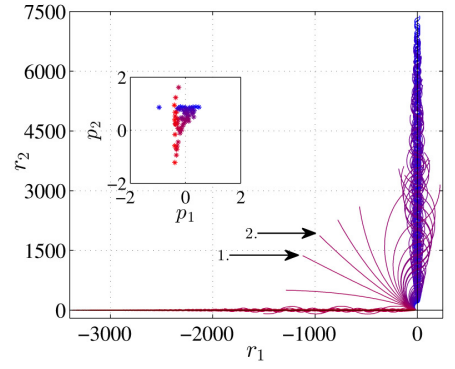	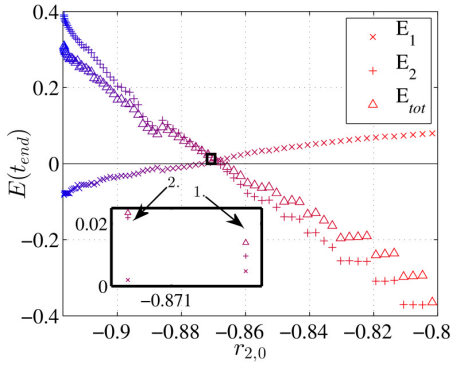

In the left column in Table 3.1, the full propagation time t_f is given. In the middle column *a)*, a cluster of 75 two-electron trajectories is plotted in configuration space. Their momentum distribution is given in the inset. The initial position of the field electron is $r_1 = 7$ a.u.. The initial positions of the bound electrons r_2 are found ≈ -1 a.u.. In the right column, the final energies of each electron and their sum relative to the initial position of the bound electron are plotted.

The color scheme, blue-to-red, refers to the sequence in which neighboring initial conditions are calculated; blue being the first and red is last.

In the first row, there are many trajectories in configuration space which, at first glance and with no further examination, would appear to represent anti-parallel double ionization. The field electron has tunneled and is found at 7 a.u.. As with such a high frequency, the field electrons' propagation is relatively short. It extends to ≈ 11 a.u. before it returns to the ion.

In this relatively short time, the bound electron performs only three oscillations across the potential well. For a short distance both electrons travel across the nucleus in the same direction before the bound electron turns, crosses the origin, and ionizes in the opposite direction. The trajectories found in the second quadrant represent anti-parallel double ionization.

Stemming from neighboring initial conditions, the transition between neighboring trajectories is smooth and consecutive. In b), the final energy of all trajectories found in a) directly after the pulse has passed is plotted. The final energy E_{tot} of the conserved system ($\triangle$) and the energy for each electron E_1 (x), E_2 (+) is plotted with respect to the bound electrons' initial position $r_{2,0}$. This is an appropriate and often implemented method of displaying final values since the only variables in the system are the initial conditions of the bound electron. Only a fraction of all calculated trajectories fulfills the energy criteria for double ionization. These double ionization events are enclosed in the thick black box. On the left side of the box is the evidence that the final energy of the system is an insufficient energy criterion for double ionization. While the final energy of the system is positive, only the final energy of the bound electron is positive. As mentioned in Section 3.2, the final energies of each electron do not add up to the final state energy.

Allowing both electrons to propagate in the single cycle pulse plus one additional field-free pulse duration results in the trajectories shown in a) in the second row of Table 3.1. All except the red trajectories are still displaying strong anti-parallel double ionization. The red trajectories describe single ionization. Both electrons were initially free running back-to-back, but then the formerly bound electron is pulled back by the ion and commences large sweeping oscillations of ± 5 a.u. across the nucleus. The corresponding momentum distribution for the electrons reflects this. The momentum for the field electron is constant, while the momentum for the bound electron varies from $\sim \pm 2$ a.u.. In the classical picture, the bound electrons travel through a large region of phase space as they have more energy. For all other trajectories, the final momenta of both electrons are smooth and reflect the continuous nature of the neighboring trajectories representing double ionization.

If the spacial criteria for double ionization of 20 a.u. were invoked, all but 22 trajectories would be considered to be double ionization events. The final energies in b) display slight shifts when compared to b) at $t_f = 1$, however, they are significant in the full ionization context. Across the spectrum the final energy of each electron is decreased by ≈ 0.01 a.u. The impact of this is seen in the magnification of the region where both electrons have positive energy. Of the 75 initial conditions only eight events could be classified as double ionization.

In the third row of Table 3.1, the two electrons have been excited by the single cycle pulse and propagated four field-free cycles longer, $t_f = 5$. There are more instances of single ionization by the formerly bound electron (now referred to as electron two). The scenario develops where the former field electron (now referred to as electron one) has initially ionized but during the field-free propagation it is unable to overcome the attraction of the nucleus. These are represented by the blue trajectories. Electron two evolves up to 150 a.u. where the electron one is pulled back to 10 a.u. The momentum distribution for these trajectories seems misleading at first glance. Even though electron one is found in the second quadrant, it is traveling towards the nucleus, i.e. in the positive direction, hence its positive momentum. The final energy for the blue trajectories, found in b), was never larger than zero for electron one. The instances of double ionization has reduced to five from a cluster of 75 trajectories.

In the fourth row, the necessity of the ionization criteria described in Section 3.5 and used in this worked can be seen. In this case, the electrons were given ten full cycles with nine field-free ones to evolve in space. In a), the trajectories show single ionization of both electrons and a few remaining double ionization trajectories. From the spacial criteria of ± 70 a.u., 15 events of double ionization would be recorded. Then with the energy criteria b) that number would be further reduced to three. In all simulations using the pulse seen in Figure 3.5, where ionization yields are considered, both electrons evolve in a field-free field for a further 12 cycles after the external pulse has passed. This selection procedure ensures that sustainable double ionization events are captured.

The non-linear nature of the simulations and extreme sensitivity of the system to the initial conditions is reflected in the trajectories in configuration space. Here the initial positions neighboring trajectories are equally spaced 1.6×10^{-3} a.u. apart. The final positions of the trajectories are irregularly spaced and widely vary in size.

Allowing the electrons to evolve a further ten cycles to a total of 20 field-free cycles does not significantly alter the general behavior of the electrons. The trajectories are presented in the fifth row in Table 3.1 a). The single ionization of electron two is clearly discernible. Further events of electron one returning to the nucleus are impending. The final momenta associated with the trajectories showing double ionization creates a smooth curve in the second quadrant of the momentum distribution. At this point, it should be pointed out that due to the left/right saddle point symmetry generated by the external field, if the phase of the pulse were shifted by $\phi = \pi$, trajectories would go in the opposite direction. In b) the same three double ionization events seen in b) are magnified.

If the progression of the electrons were followed up to 50 field-free cycles, the single ionization channels dominate over the double ionization considerably. At $t_f = 50$, the red trajectories only reach half the distance of the blue trajectories. The oscillations are more compact, signifying a small radius of the bounded electron two around the nucleus. This, in turn, is an indication of

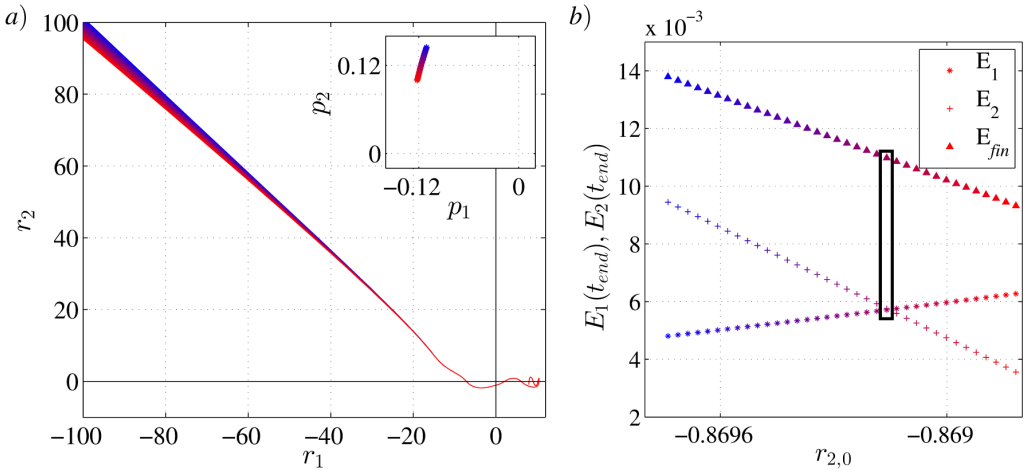

FIGURE 3.6: *a*) shows neighboring trajectories on and around $-r_1 = r_2$. Each trajectory describes near to exact anti-parallel double ionization. The momentum of both electrons is given in the inset. *b*) final energy values for both electrons at $t_f = 200$ cycles. The initial positions of the bound electron are separated by 3×10^{-5} a.u. and there is one case where both electrons have near to exact final energy (black box). Further details of end values are given in Table 3.2

a larger binding energy, as seen in *b*). The blue trajectories, on the other hand, show that electron two ionizes, while the lightly bound electron one performs large oscillations. The energy criterion for double ionization has eliminated a further contestant for a double ionization event. From the original 75 initial trajectories, only two are left which represent double ionization. For completeness, trajectories which evolved a full 100 field-free cycles was included, $t_f = 100$. However, other than distance covered, there is no difference in the ionization behavior.

In the last row of Table 3.1, there are two black arrows pointing to two trajectories in *a*). The corresponding final energies of the electrons for each trajectory are specified in *b*). If the system were to progress another 200 field-free cycles, trajectory 2. would eventually evolve into a single ionization event. Trajectory 1. has the best chance to survive as double ionization. Most significant is the distribution of the energy between the two electrons. Their final energy is very similar. This is a strong contributing factor to the survival of a doubly ionized state. That is why these trajectories are referred to as *true* trajectories of double ionization. Both electrons interacted only once. In each cluster of ionizing initial conditions, there is one surviving trajectory

Difference of end values at $t_f = 200$ cycles in a.u.				
$\lvert r_1\rvert - \lvert r_2\rvert$	$\Delta p_{1,2}$	ΔT	ΔV	$\Delta E_{1,2}$
1.4	4×10^{-4}	5×10^{-5}	2×10^{-6}	5×10^{-5}

TABLE 3.2: The final state values for the anti-parallel double ionization encased in the black box in Figure 3.6 *b*) are compared after propagation in $t_f = 200$ field-free cycles. All values, position and momentum, kinetic, potential and final energy are given in atomic units and rounded. The minimal difference in the final values underline the symmetry of the anti-parallel escape.

for $t_f \to \infty$. The difficulty lies in finding the initial condition that leads to that one trajectory.

Backtracking on trajectory 1. ends at its initial position. Within a small interval around this region of phase space, the initial positions are spaced 3×10^{-5} a.u. apart. All trajectories are propagated 200 field-free cycles but only plotted up to 100 a.u. in Figure 3.6. All trajectories are strikingly similar and only begin to slightly diverge around ± 40 a.u. In b), the final energy of the two electrons is plotted. The black box encloses the case where the two electrons have near to exact final energy. The final state values of this *true* trajectory are compared in Table 3.2.

Chapter 4

Electron Ionization Dynamics from a Monochromatic Wave

A decade ago it was popular to approximate an oscillating field with constant amplitude and a trapezoidal envelope [33, 42, 70, 78]. The pulse consisted of a plateau region with equal amplitude and short ramp-on/ramp-off region analog to the one described in Equation 3.12 and seen in Figure 3.4. The field is constructed to have an integer number of field cycles. The zero-net force condition is fulfilled. These pulses are advantageous because they have equal peak field amplitudes in the plateau region. This provides a welcome symmetry as each field cycle generates identical ionization dynamics.

4.1 Trajectories

The trajectories plotted in configuration space contain information on the motion of both electrons. Both electrons are considered to be ionized when each of their single-particle energy is greater than zero *and* they have traveled beyond a boundary limit $l_d = X$ a.u. away from the ion. A pulse with many field cycles causes multiple re-collisions between both electrons and the nucleus. This can lead to very complicated electron trajectories. If one were to study the final states of the electrons, then the complexity of their trajectories is immaterial. However, the aim in this research is to study the impact of the incident electron and the influence of the Coulomb repulsion and the atomic potential. It is therefore advantageous to concentrate on the electron-electron interaction from known instances of direct double ionization.

An example of the pulse with the trapezoidal envelope is seen in Figure 4.1 a). The leading two cycles are not included in the graphic. The numerical simulations begin at the first maximum in the plateau at $t_i = 2$ cycles. The plateau field strength is $F_0 = 0.18$ a.u. and the field frequency

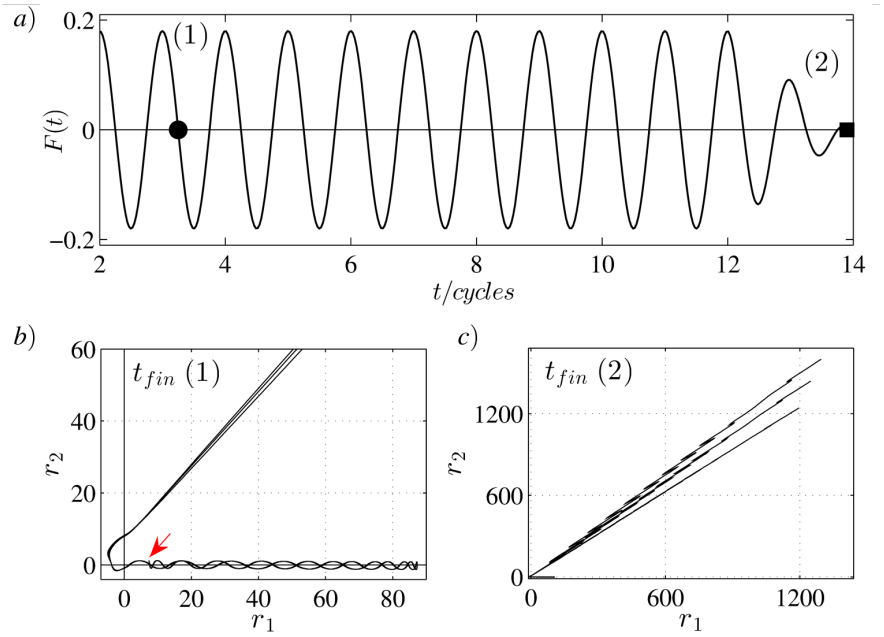

FIGURE 4.1: *a*) The trapezoidal pulse with a plateau field strength of $F_0 = 0.18$ a.u. and frequency $\omega = 0.06$ a.u.. The circle (1) denotes the final calculation time for the trajectories in subplot *b*). The square (2) denotes the final calculation time for trajectories seen in *c*). The red arrow in *b*) points to the initial positions of the electrons.

is $\omega = 0.06$ a.u.. The circle (1) and the square (2) denote the end calculation time for the simulations. The circle (1) corresponds to a calculation time $t_f = 9\pi/2\omega$. The trajectories plotted in configuration space are found in *b*). The ones which propagated the full pulse length are seen in *c*). They reach distances of $r_1, r_2 \approx 1200$ a.u.. Even though the electrons are far away from the ion, they are continuously influenced by the field. The essential dynamics remain the same. In both subplots *b*) and *c*), the only difference between the trajectories is the final calculation time.

Trajectories are calculated in sequence from neighboring initial conditions. The double ionization trajectories emerge in clusters. All trajectories must be allowed to propagate the full length of the pulse. It is a particular advantage of the classical description that the entire progression of each electron can be followed. In some cases, trajectories initially show double ionization after a few field cycles only to change direction mid-pulse and return to the nucleus. As long as the field is on, trajectories are calculated in their entirety. For optical simplicity, emphasis is on the region of re-collision where double ionization has already been found, seen in Figure 4.1 *b*).

The double ionization trajectories in Figure 4.1 *c*), and magnified in *b*), are typical for those generated with such a pulse form and parameter configuration. The field electron is located outside the potential barrier created at the field maximum at ≈ 7 a.u. while the bound electron is close to the nucleus. The red arrow points to the initial positions of the electrons in Figure 4.1 *b*). The time evolution of the field first causes a deformation in the atomic potential resulting

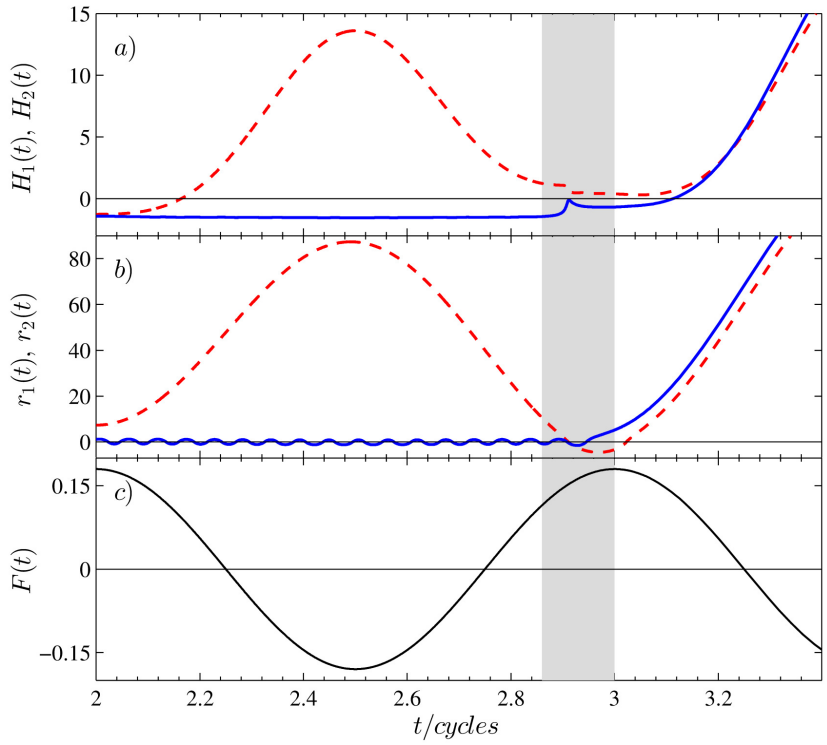

FIGURE 4.2: *a*) The Hamiltonian of the field electron $H_1(t)$ (red) and the Hamiltonian of the bound electron $H_2(t)$ (blue) from one of the trajectories found in Figure 4.1. In *b*), the positions $r_1(t)$ (red) and $r_2(t)$ (blue) of both electrons are plotted. The external field $F(t)$ is given in *c*). The shaded region highlights the interval where the collision between both electron occurs.

in the field electron effectively "sliding" down the potential as it grows. When the field nears the second maximum, $t \to t_i + \pi$, the field electron slows down. After the field maximum has passed, the field electron is accelerated back towards the nucleus at ≈ 90 a.u..

During the field electron's excursion in the external field, the bound electron is moving back and forth between the turning points in the potential well at $-1 \leq r_2 \leq +1$ a.u.. As the field electron nears the nucleus, the increase in its velocity can be seen in the lengthening oscillations. Upon re-collision, the field electron interacts with the bound electron once. The field electron passes the bound electron, crosses the nucleus, and approaches the now increasing atomic potential. There the re-colliding electron turns and follows the now-freed electron out over the sinking Stark barrier.

A more detailed study of a trajectory found in Figure 4.1 is given in Figure 4.2. In *a*), the Hamiltonian of each electron during the first few cycles of the external field is plotted. Both electrons have an initial energy value of $E_0 = -1.415$ a.u.. The Hamiltonian of the field electron (dashed red line) is strongly influenced by the phase of the external field. The time of collision is $t \approx 2.9$ field cycles. A dip can be seen in the Hamiltonian of the field electron while the Hamiltonian of the bound electron (blue line) jumps up to $H_2 = 0$. The Hamiltonian of the

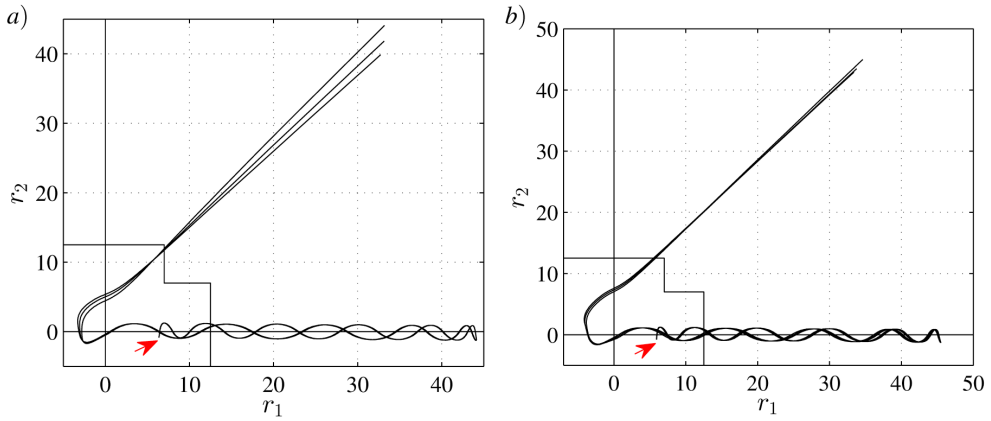

FIGURE 4.3: $a)$ and $b)$ demonstrate a separate family of trajectories stemming from neighboring initial conditions. The trajectories in both images are generated from a monochromatic driving field of strength $F_0 = 0.2$ a.u. and frequency of $\omega = 0.09$ a.u..

bound electron becomes positive once the latter travels across the saddle from the subsequent maximum in the external field.

The electron trajectories $r_1(t)$ and $r_2(t)$ are plotted in Figure 4.2 b. The trajectory of the field electron (red dashed line) begins at ≈ 10 a.u.. Under the influence of the external field, the field electron is pulled away from the parent ion. The bound electron oscillates between the two classical turning points in the potential well. When the field electron returns to the ion, the bound electron is moving in the same direction. This constellation allows the two electrons to interact the longest. The energy transfer from the incident electron to the bound electron is not sufficient to ionize the bound electron directly. Both turn, cross the nucleus and ionize in the direction of the incident electron. The shaded region highlights the time where the interaction occurs.

There can be multiple clusters of discrete neighboring initial conditions found on the energy shell that lead to double ionization. Examples are given in Figure 4.3. The set of trajectories found in $a)$ is generated from one set of neighboring initial conditions in phase space. The set of trajectories, seen in $b)$, stems from a set of neighboring initial conditions from a very different region of phase space. The red arrow points to the initial positions. Small differences between the sets of trajectories are noticeable. The only variables in both sequences are the initial conditions of the bound electron. This can be seen in the oscillations the bound electron performs.

In each subplot, three trajectories are plotted. In $a)$, by the time the trajectories reaches the second quadrant, the atomic potential has such an influence that neighboring trajectories are strongly reflected. The trajectories in $b)$, on the other hand, are found very close together. This underlines the non-linear effect of the Coulomb potential. The excursion of the field electron is approximately 45 a.u. for a field frequency of $\omega = 0.09$ a.u.. Compared to the excursion of

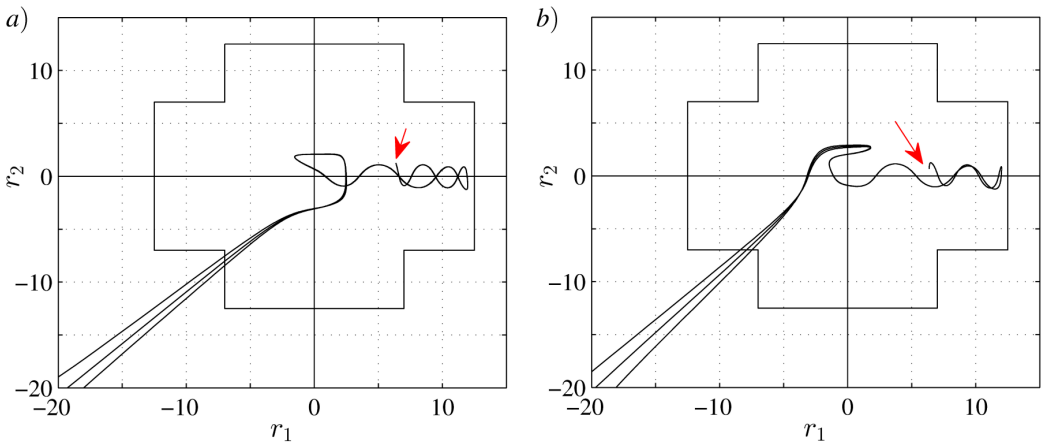

FIGURE 4.4: *a)* and *b)* demonstrate a separate family of trajectories stemming from neighboring initial conditions. Both images were generated from a monochromatic driving field of strength $F_0 = 0.2$ a.u. and frequency of $\omega = 0.22$ a.u..

the electron in a field with frequency $\omega = 0.06$ a.u. (seen in Figure 4.1 *a)*), it is nearly half the length.

In the subplots *a)* and *b)* in Figure 4.3, the thin lines represent the boundary of the atom. The dimensions of the region are $l_{d_1} = 12.5$ a.u. and $l_{d_2} = 7$ a.u. used in the quantum picture, as seen in Figure 3.1. In this case, the direct double ionization in Figure 4.3 *a)* would contribute to the direct double ionization yields whereas those trajectories found in *b)* would not.

In Figure 4.4 the trajectories have been generated using an external field with amplitude $F_0 = 0.2$ a.u. and frequency $\omega = 0.22$ a.u.. As in Figure 4.3, both *a)* and *b)* show clusters of trajectories stemming from different regions in phase space. Their initial positions are indicated by the red arrow. The difference in the progression of the trajectories is more pronounced than for the ones found in Figure 4.3. In both sets, the bound electron performs four full oscillations within the potential well while the field electron is traveling in the external field. The excursion of the field electron is very limited. It only reaches a length of ≈ 12 a.u. even though it starts at the same position as the field electron in Figure 4.3. This stems from the fact that the frequency is so large. The atomic potential changes rapidly. The field electron returns at the same time in the fields cycle $t \to t_i + 2\pi$, but it does not gain sufficient energy from the field, $U_p \sim 1/\omega^2$, to directly ionize both electrons. An additional crossing of the nucleus is necessary to gain the energy needed. This can be seen in both *a)* and *b)* in Figure 4.4. The trajectories ionize over the fourth during, as opposed to the third, compared to Figure 4.1 and Figure 4.3. This is also the reason why both electrons are traveling together in the third quadrant.

Up to now, the trajectories discussed show that the electrons do not ionize simultaneously over the Stark barrier. They leave the atom slightly shifted, one after the other. There is a further noticeable detail in each set of trajectories. At re-collision, the influence of the Coulomb potential becomes apparent. Until the field electrons return to the nucleus, all trajectories are

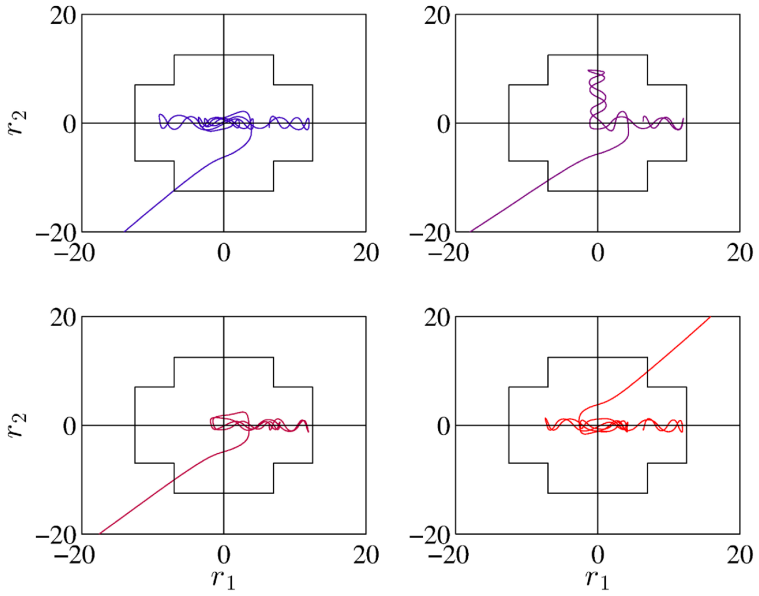

FIGURE 4.5: From an external field with amplitude $F_0 = 0.2$ a.u. and frequency of $\omega = 0.22$ a.u., each of the four trajectories has very different initial conditions and all need a full field cycle longer in the pulse to ionize compared to the direct ionization.

synchronous. Each field electron will return at the same time. The only variable is the position of the bound electron which is small. The field changes so rapidly with a frequency of $\omega = 0.22$ a.u. that only few neighboring trajectories experience similar advantageous conditions which are necessary for a successful double ionization event. Here, all double ionization events here would contribute to the direct parallel double ionization yields in the quantum calculation.

Figure 4.5 presents four sample non-sequential double ionization trajectories. Each was generated with the same field parameters as those in Figure 4.4. All four needed a full cycle longer to ionize than those shown in Figure 4.4. The initial conditions for the bound electron are found in four separate regions on the energy shell. The trajectories are significantly more dynamic than those presented previously. Here, one electron is bound until enough energy has been gained and the channel to direct double ionization opens when both electrons are in the vicinity of the emerging saddle in the potential. In the lower right figure, the channel opens in the first quadrant whereas the others doubly ionize in the third quadrant.

4.2 Summary

The smaller the frequency, the longer the field electron's excursion in the field and the more oscillations the bound electron performs. At high pulse frequencies, electrons execute multiple re-collisions before ionizing. This is due to the small energy transfer and the importance of the phase of the external field. At low frequencies, a single collision between the electrons is sufficient for NSDI.

The duration of the interaction between the electrons is pivotal to the success of double ionization. There is a time delay from initial interaction to double ionization. It depends on the phase of the external field and on the time when the saddle point over which the electrons can ionize emerges. For NSDI, the field electron and bound electron must move in the same direction during the first interaction. This is when the bound electron is at or just beyond maximum momentum. The duration of the electrons' proximity near the nucleus reflects the correlated nature of double ionization. In Chapter 5, the role the Coulomb repulsion plays in the ionization process will be subject of further analysis.

Chapter 5

Electron Ionization Dynamics from Strong Short Pulses

5.1 Single-Cycle Pulses

By the end of the twentieth century, advances in laser technology lead to the generation of few-cycle femtosecond (10^{-15}s) pulses [75, 79, 81]. One of the main applications of ultrashort pulses is the study of ultrafast phenomena, i.e. electron dynamics, in its natural time scale. The electron-electron interaction at the single-cycle limit was investigated in the laboratory [14, 38, 59]. The theoretical investigations into single-cycle double ionization first began within the quantum picture [22, 56] and then within the classical representation [44].

Confining the electron interaction to a single cycle inherently reduces the number of possible re-collisions between the electrons and nucleus. The complexity of the double ionization trajectories is reduced and the fundamental properties of the electrons' interaction can be studied. The classical dynamics of double ionization generated from a strong short pulse with a sine-squared envelope are presented in this chapter.

To recapitulate the initial situation, the first field maximum of the external pulse deforms the Coulomb potential of the helium atom so that a saddle in the atomic potential emerges. The field electron is located just outside the potential barrier at $r_{1,0}$. While the position, $r_{1,0}$, is dependent on the effective external field strength, the momentum of the electron does not $(p_{1,0} = 0)$. For a given set of field parameters, the only variables in the system are the initial conditions of the bound electron.

5.1.1 Initial Conditions

Identifying initial conditions in phase space which lead to double ionization demands a comprehensive parameter study. For Figure 5.1 and Figure 5.2, each parameter set was calculated from an ensemble of 2×10^5 initial conditions. The peak field amplitude in each calculation was $F_0 = 0.29$ a.u., the phase $\phi = 0$ a.u. and frequency $\omega \in [0.045\text{a.u.}, 0.183\text{a.u.}]$. The domain of the initial positions for the bound electron is the same for calculations with varying frequency.

Figure 5.1 is a two-dimensional histogram of the the initial position of the bound electron, $r_{2,0}$, and the field frequency ω. In the left panel, the initial momentum of the bound electrons was positive while on the right it was negative. The initial positions of the bound electron are found at discrete distances along the energy shell. The color bar denotes the number of double ionization events per bin.

In Chapter 3, it was shown that the initial conditions that lead to double ionization occur in clusters. In Figure 5.1, each field frequency is associated with one continuous region in phase space where the initial conditions lead to double ionization. In both plots, there is no discernible connection between the initial conditions found in phase space and the success of double ionization.

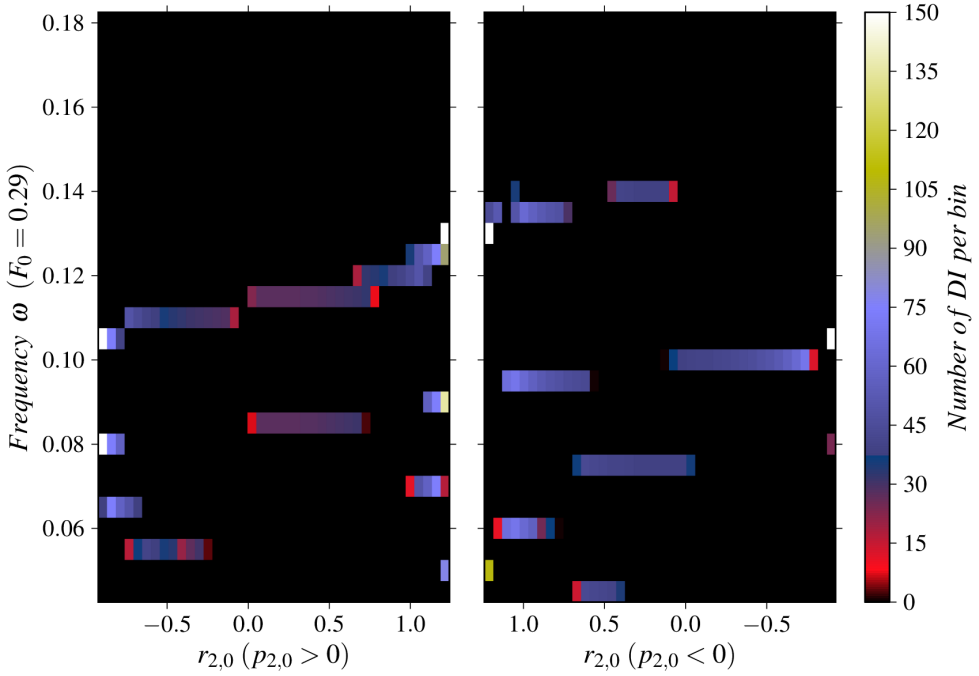

FIGURE 5.1: For 22 different field frequencies, an ensemble of 2×10^5 initial conditions of the bound electron, both for positive $(left)$ and negative initial momentum $(right)$ were calculated. For all results, the pulse applied had a peak field amplitude of $F_0 = 0.29$ a.u.. The number of initial conditions per bin that lead to double ionization are highlighted according to the color bar on the right.

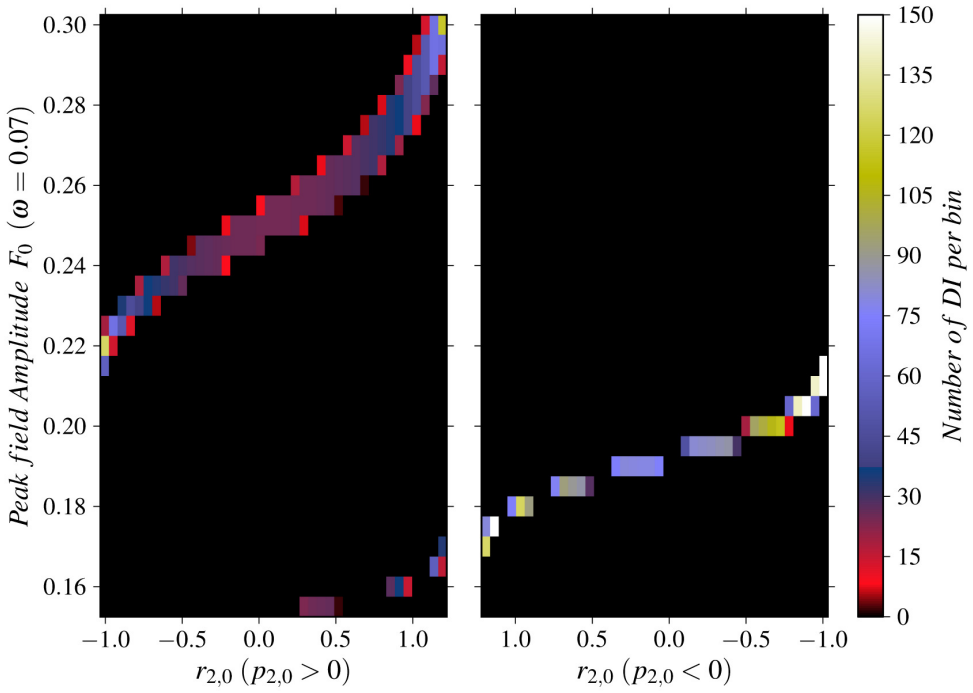

FIGURE 5.2: For 30 different peak field amplitudes, an ensemble of 2×10^5 initial conditions of the bound electron, both for positive $(left)$ and negative initial momentum $(right)$ were calculated. For all results, the pulse applied had a frequency of $\omega = 0.07$ a.u.. The number of initial conditions per bin that lead to double ionization are highlighted according to the color bar on the right.

Figure 5.2 is a histogram with the same composition as Figure 5.1. In this case, the initial positions of the bound electron are plotted against the peak field amplitude. The field frequency, $\omega = 0.07$ a.u., was the same in each simulation. Hence, increasing the peak field amplitude corresponds to a quadratic increase in the electrons' ponderomotive potential.

Again, for each parameter set, only one cluster of initial conditions lead to double ionization. Except in the amplitude range of $F_0 \in [0.17 \text{ a.u.}, 0.21 \text{ a.u.}]$, the initial momentum of the bound electron is negative for successful double ionization events. With increasing field strength, the clusters of neighboring initial conditions of the bound electron that lead to double ionization are found successively along their energy shells. At even higher amplitudes, the clusters overlap.

There is an indisputable connection between the initial conditions that lead to double ionization and the peak field amplitude of the external pulse. While the initial energy of the bound electron is the same, the field strength effects the shape and size of the energy shell upon which the initial conditions of the bound electron are calculated. Increasing the field amplitude distorts the Coulomb potential such that the field electron has less of a distance to tunnel and is therefore found progressively closer to the parent ion.

The number of oscillations made by the bound electron is constant for each field strength. The time it takes for the field electron to return to the parent ion decreases continuously. This is

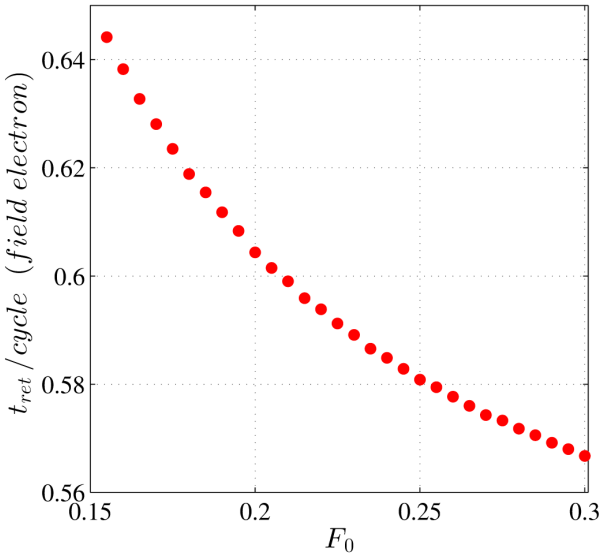

FIGURE 5.3: The return time, in cycles, of the field electron for increasing peak field amplitude.

shown in Figure 5.3. The time (in cycles) when the field electron returns to the ion is plotted as a function of the peak field amplitude. It is this continuity that is responsible for the connection between the field strength and the initial conditions that lead to double ionization. With the field electron returning to the parent ion earlier for each field strength, there is a specific set of conditions that each bound electron can have for successful double ionization.

Double ionization does not necessarily depend on the region where initial conditions are found in phase space, rather on the region the bound electron occupies in phase space when the field electron returns to the ion. A more detailed analysis of the electron ionization dynamics is presented in the following sections which support this conclusion.

5.1.2 Ionization

The four one-dimensional histograms in Figure 5.4 depict the single-cycle pulse (black line) with a constant peak field amplitude of $F_0 = 0.3$ a.u. for four different field frequencies, $\omega = 0.045$, 0.06, 0.096, and 0.15 a.u.. The red bar shows the time during the pulse when the field electron returns to the edge of the Coulomb well. The blue bars indicate when both electrons have positive energy. The yields vary significantly between the four frequencies. Therefore, the histogram is scaled to indicate the percentage of double ionization yields for each calculation.

For the smallest frequency $\omega = 0.045$ a.u., the field electron returns to the ion earliest in the pulse, even though the excursion of the field electron is the largest. Double ionization sets in shortly after the third field maximum and then drops off significantly by the end of the pulse. The time between return and ionization is the second largest.

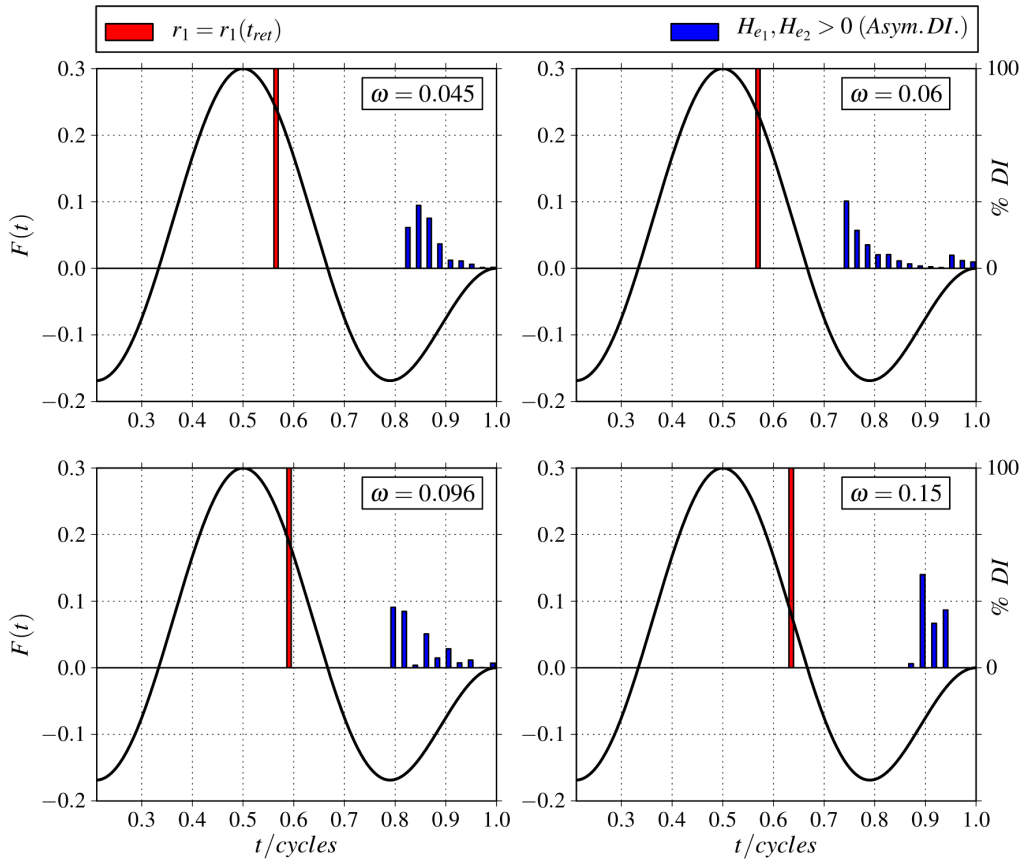

FIGURE 5.4: Single cycle pulse (black curve) with peak field amplitude and phase $F = 0.3$ a.u., $\phi = 0$ a.u. respectively. In each figure, four different field frequencies $\omega = 0.045$, 0.06, 0.096, 0.15 a.u. have been used. In the histogram, the red bar represents the time in the pulse when the field electron arrives at the edge of the Coulomb well after its excursion in the field. The blue bars show at what time both electrons have energy larger than zero, which corresponds to double ionization. The results were scaled, showing the total percentage of double ionization.

In the upper right figure, results are given for $\omega = 0.06$ a.u.. The field electron returns to the ion later in the pulse, than for $\omega = 0.045$ a.u.. The time interval between field electron return and effective double ionization is the smallest of all frequencies investigated. In this case, ionization begins even before the third maximum in the pulse. There, a strong ionization signal is registered. By the third field maximum, the ionization signal is weakest.

The lower left plot in Figure 5.4 was generated with $\omega = 0.096$ a.u.. The field electron returns even later in the pulse. Double ionization effectively begins at the third maximum where it also has the strongest signal. The double ionization signal trails off towards the end of the pulse as is the case for $\omega = 0.06$ a.u..

The lower right plot in Figure 5.4 was generated with the highest frequency that still produces double ionization, $\omega = 0.15$ a.u.. The field electron returns just before the zero-crossing of the pulse. It is important to keep in mind that, with increasing frequency, the time scales of the sequence of events are difficult to compare. Contrary to how it appears, the field electron, while

returning later in the pulse, effectively spends the least amount of time in the external field. Double ionization sets in late in the pulse but with increasing yields.

In all plots, the field electron does not return to the ion by the second peak in the field. With increasing frequency, the field electron will return to the ion at a later time during the pulse. After the collision, both electrons propagate in the field for a quarter of a cycle before the electrons' individual energy is larger than zero. With the exception of the calculations performed with $\omega = 0.06$ a.u., the double ionization signal peaks at or just beyond the third field maximum. This indicates that the saddle in the potential, caused by the third maximum, aids in the double ionization process. The time difference between time of the field electrons' return to time of ionization does not remain constant. None of the four subplots indicate an instantaneous double ionization process.

5.1.3 Trajectories

In Figure 5.5, the position of the field electron and the bound electron is plotted as a function of time, $r_1(t)$ and $r_2(t)$. The black line is the scaled external pulse $35F(t)$. In the calculations, the single-cycle pulse had a peak field amplitude of $F_0 = 0.3$ a.u., a field frequency of $\omega = 0.15$ a.u., and a phase $\phi = 0$ a.u..

The initial position of the field electron at the time of the first field maximum is found at approximately 7 a.u. with zero initial momentum. The 18 initial conditions for the bound electron are located on the upper half of the energy shell, $(p_{2,0} > 0)$. The positions are magnified in the upper left inset. Each simulation begins with the same initial condition for the field electron and one of the initial conditions from the upper half of the energy shell for the bound electron.

The neighboring initial conditions for the bound electron were calculated in sequence. Both single-electron trajectories from the same simulation are plotted in the same color, starting with blue and ending with red. The red trajectories for the field electron initially mask the blue trajectories.

Due to the high frequency, the field electron does not make a significant excursion in the field. It turns toward the ion before the second field maximum and returns to the ion when the field has a zero-crossing. In all cases, the bound electron completes three oscillations across the potential before the field electron returns to the ion. The bound electron finds itself in 18 different states when the field electron approaches. For all but the blue trajectories, the field electron and the bound electron are traveling in opposite directions when crossing the nucleus. This is magnified in the lower left inset.

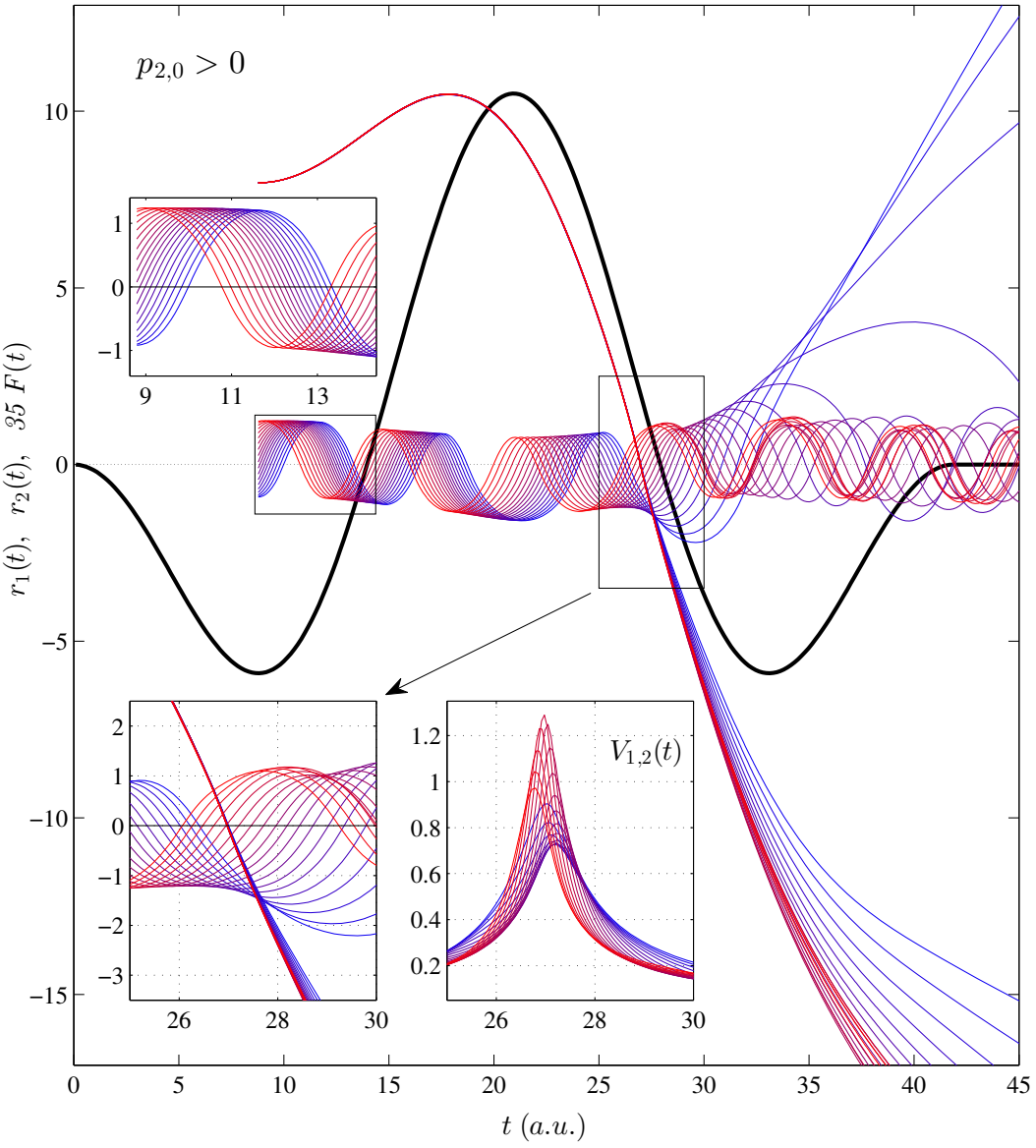

FIGURE 5.5: A trajectory for each electron is generated by the external pulse (black line) with $F_0 = 0.3$ a.u.,$\omega = 0.15$ a.u.,$\phi = 0$ a.u.. The 18 trajectories for the field electron begin at ≈ 7 a.u. while the 18 for the bound electron each begin at discrete distances in the potential well (magnified in the upper left inset). The bound electrons' initial momentum is positive, except at the classical turning points where it is zero. Per simulation, one color for both trajectories was used, i.e. the blue trajectory from the field electron corresponds to the blue trajectory of the bound electron. For each calculation, the field electron returns to the ion at the same time while the bound electron is in 18 different states (magnified in the lower left inset). The electron-electron interaction $V_{1,2}$ is plotted in the lower right inset. The dark blue trajectories demonstrate anti-parallel double ionization.

The red trajectories show the field electron returning to the ion near $r_1(t_{ret}) = 1$ a.u.. There, it collides with bound electron at the turning point. Following the course of their trajectories reveals that little energy transfer has occurred. Both electrons are least affected by the interaction.

In the case of the field electron returning and interacting with bound electron which is at $r_2(27) = 0$ with maximum momentum results in the strongest peak in the interaction potential, $V_{1,2} \approx 1.3$, (lower right inset). The interaction is given by Equation 2.7b with a cut-off parameter $\varepsilon = 0.6$ a.u.. After the collision, the oscillations of the bound electrons are smaller. This indicates that an energy transfer has occurred. The corresponding energy gain of the field electron is mirrored by its increased velocity.

The electrons which have the longest interaction during the collision will most likely result in a double ionization event. In Figure 5.5, they are illustrated by the blue trajectories. Their interaction begins to increase when the field electron returns to the ion. With both electrons traveling in the same direction, the field electron is initially behind the bound electron. Then, the field electron catches up to the bound electron. The blue trajectories show highest interaction values as the field electron overtakes the bound electron and ionizes. After the collision, the field electron is slower. This indicates that an energy transfer has taken place. The corresponding bound electron crosses the nucleus and ionizes in the opposite direction.

There is no indication of a process of the field electron "repelling" the bound electron out of the ion while traveling across the nucleus, and subsequently ionizing in the same direction. Through the long interaction time, the bound electron gains energy but strong repulsion and the increasing potential wall hinders its direct progression out of the well.

Figure 5.6 has the same composition as Figure 5.5. The field electron has the same initial conditions and those for the bound electron are calculated along the lower half of the energy shell, $p_{2,0} < 0$. The numerical integration of one set of initial conditions results in the electron trajectories, $r_1(t)$ and $r_2(t)$, which are plotted in the same color.

The trajectories for the bound electron show that it completes three full oscillations before the field electron returns to the ion. Before completing the third oscillation, the trajectories tend to bundle together. This is due to the influence of the second maximum in the external field. The strength of the peak causes a strong deformation of the potential and, subsequently, the width of the well contracts. This effect is not so pronounced in Figure 5.5.

Following the blue trajectories, the bound electron begins at the positive classical turning point with zero momentum. When the field electron returns to the ion, the bound electron approaches from the opposite direction. This can be seen better in the lower left inset. The interaction $V_{1,2}$ between the two electrons is short (lower right inset).

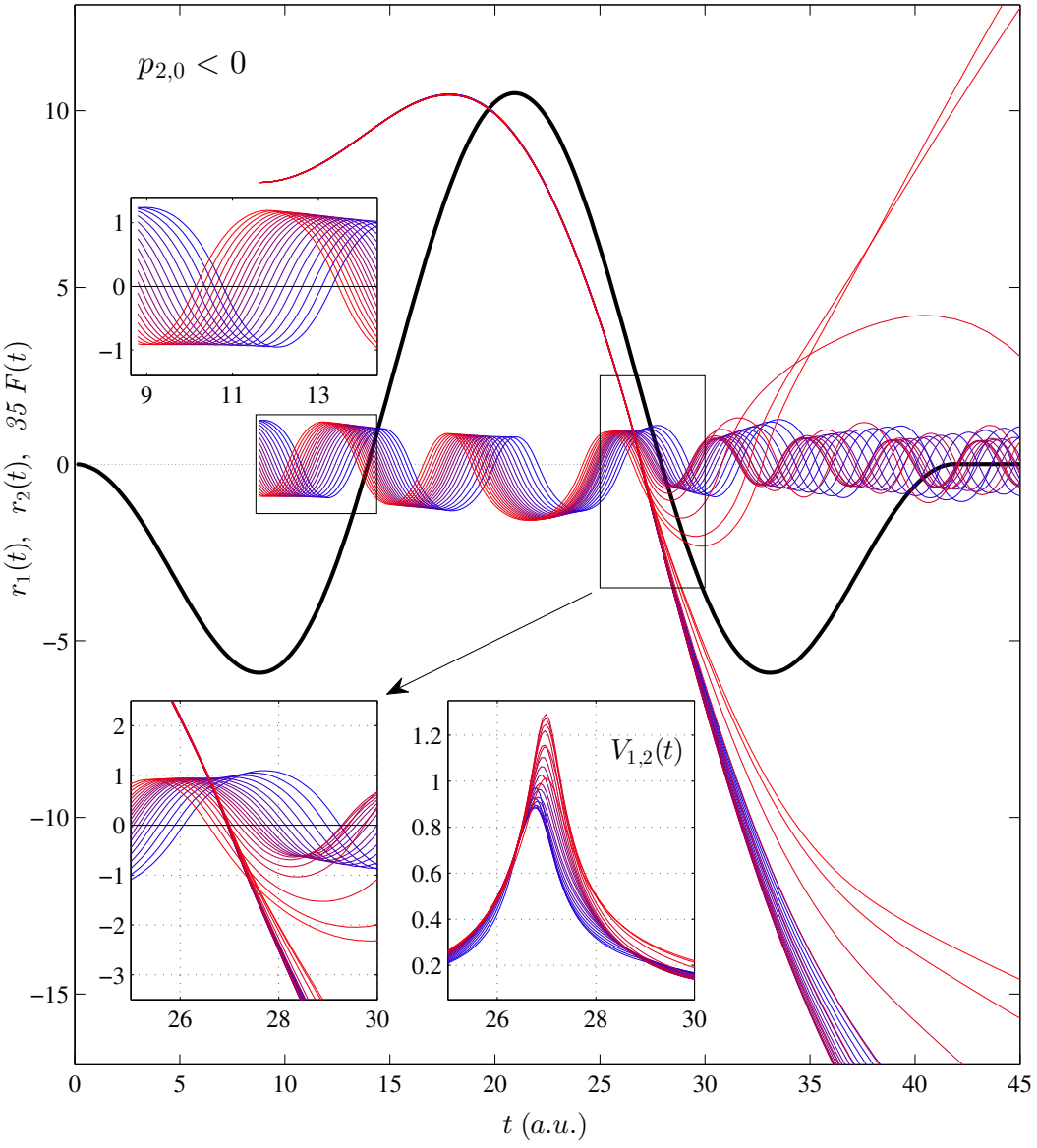

FIGURE 5.6: The difference to Figure 5.5 is the bound electrons' initial momentum which is negative, $p_{2,0} < 0$. The dark red trajectories demonstrate anti-parallel double ionization.

In this set of initial conditions, there are more trajectories which show the bound electron traveling in the same direction as the field electron. The difference between the ionizing trajectories lies in the duration of interaction.

When the field electron collides with the bound electrons (purple trajectories), the bound electron has just turned and its momentum is very small. The interaction is longer than that seen in the blue trajectories. The oscillations of the bound electrons are smaller after the collision. This indicates an energy transfer from the bound electron to the field electron.

The red trajectories from the field and bound electron show that their mutual repulsion is large over a longer period of time. The field electron has a smaller velocity after collision. A part

of its energy has been transfered to the bound electron which can escape over the saddle in the potential induced by the pulse's third maximum.

The trajectories that lead to double ionization are similar in both figures: There is a single collision, both electrons must cross the nucleus in the same direction, and have the longest interaction duration. Furthermore, the $r_1(t)$, $r_2(t)$ trajectories show that shortly before final double ionization, after both electrons traversed the nucleus in the same direction, the bound electron turns back, crosses the origin and ionizes in the opposite direction.

A more in depth analysis of this behavior is given in the next section.

5.1.4 Coulomb Repulsion

In Figure 5.5 and Figure 5.6, the trajectories depicting anti-parallel double ionization within one field cycle are detailed. The question arises as to why no direct double ionization process is observed. To determine what prevents parallel non-sequential double ionization in the single-cycle limit, the interaction between the two electrons at their collision is plotted in incremental time steps.

In Figure 5.7, the external electric field $F(t)$ is given. The field was generated with the same parameters used in the previous section, namely $F_0 = 0.3$ a.u., $\omega = 0.15$ a.u., and $\phi = 0$ a.u.. There are nine vertical lines at specific times of the pulse, each of which is marked with a letter $(a) - (i)$. Each letter corresponds to a subplot in Figure 5.8. There, a snapshot of the electrons and their position relative to each other and the state of the potential is plotted. The

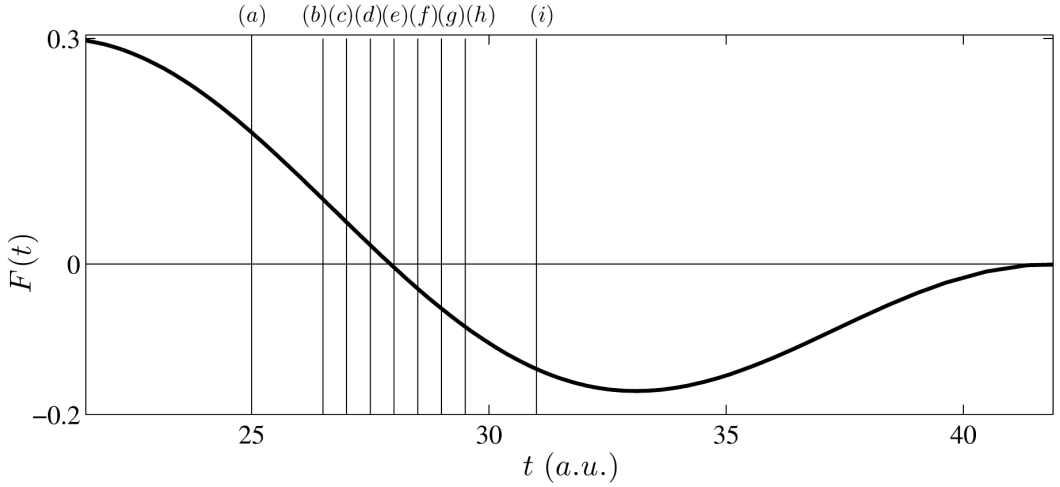

FIGURE 5.7: External electric field, with $F_0 = 0.3$ a.u., $\omega = 0.15$ a.u., $\phi = 0$ a.u., as a function of time. Each of the letters correspond to time frames in Figure 5.8. Herewith, the position of both electrons can be retraced and a more detailed picture of the effects of the electrons repulsion is revealed.

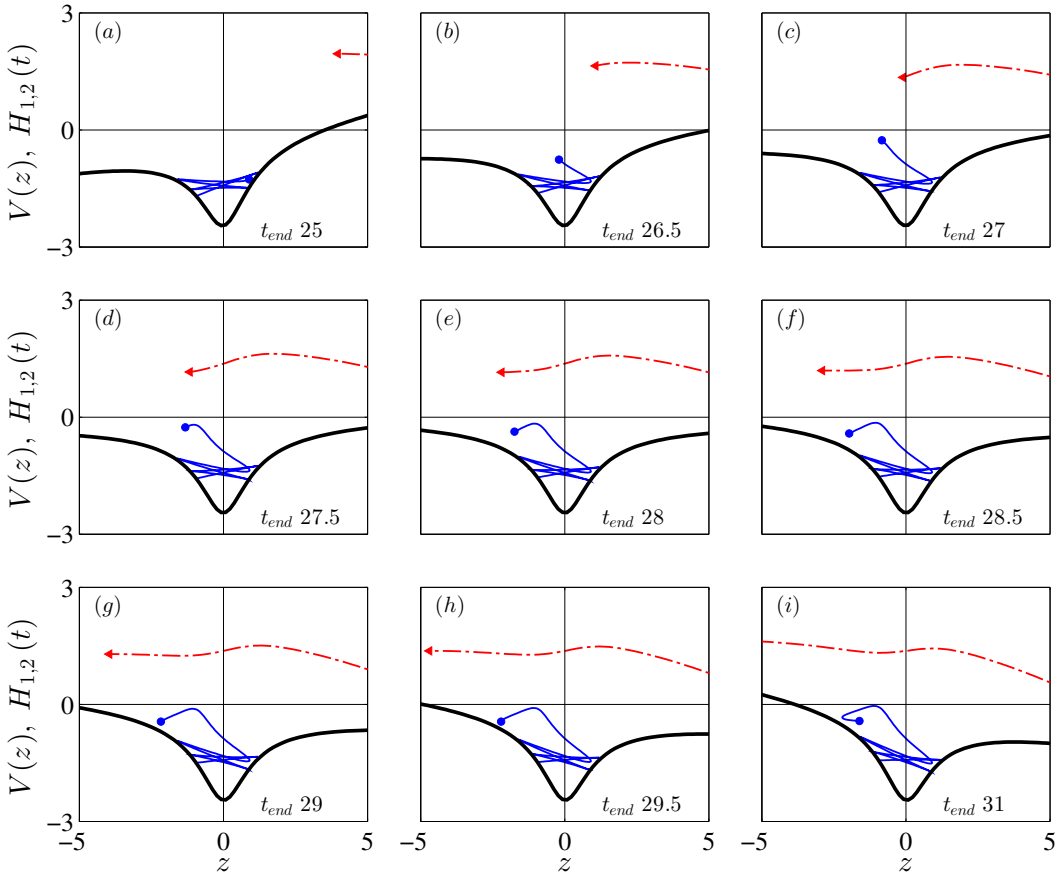

FIGURE 5.8: The detailed interaction of two electrons leading to a double ionizing event, (blue trajectory in Figure 5.5), plotted at time intervals (a)-(i), given in Figure 5.7. The Hamiltonian of the bound electron (blue) and the Hamiltonian of the field electron (red) is plotted. The Coulomb potential (black line) is driven by the external pulse. (a) shows the field electron returning in red dashed line. The bound electron oscillates between both turning points.

doubly ionizing blue trajectory in Figure 5.5 is the double ionization event that is investigated in Figure 5.8.

The black line in the subplots in Figure 5.8 show the Coulomb potential $V(z)$ under the influence of the time-dependent external field. The Hamiltonian of each electron $H_{1,2}(t)$ is time dependent and is given instead of the electrons' energy. The Hamiltonian of the field electron is represented by a red triangle and its previous values are indicated to by a red dashed line. The Hamiltonian of the bound electron is given by a blue dot and line. The calculation end times shown in Figure 5.7 are given in the lower right corner of each subplot.

In (a), the field electron that had been previously accelerated in the external field approaches the ion at time $t_{end} = 25$ a.u.. The bound electron has completed three full cycles within the potential well. The bound electron is at the positive turning point in the potential well and is about to change direction. In (b), 1.5 a.u. later, the bound electron has been noticeably influenced by the oncoming field electron. It has gained significant energy, not only in part due to the maximal

momentum gained crossing the nucleus but also due to the approaching field electron. The next six subplots are given in time increments of 0.5 a.u.

In (c), the field electron has reached the origin. The bound electron is directly in front of the oncoming field electron. In (d), the field electron is closest to the bound electron and their mutual repulsion is at maximum. The momentum of the field electron is greater than that of the bound electron. Instead of propelling the bound electron out of the well, the field electron passes beyond the bound electron. The mutual repulsion causes a deceleration and a decrease in the kinetic energy of the bound electron.

The momentary energy of the bound electron might initially suggest a possible direct channel to double ionization. The increasing potential wall, caused by the second maximum in the external pulse, is a barrier that a classical particle cannot surmount. In (g) and (h) the Hamiltonian of the field electron is large enough so that the field electron ionizes directly. However, in (i), the bound electron has changed direction. It will gain momentum by crossing the origin. At the next field maximum, it will escape over the Stark saddle and ionize in the opposite direction.

The electrons' mutual repulsion initially accelerates the bound electron, but as the incident electron overtakes the bound electron, the latter is pushed back. After changing direction at the turning point and crossing the origin, ionization coincides with a sinking Stark saddle over which the bound electron leaves. If the approach is not timed correctly, then the bound electron might need to make one further oscillation across the nucleus before ionizing. This scenario may occur for external pulses with low field frequencies, an example of which is given in Figure 5.9 with a more detailed analysis shown in Figure 5.10 and Figure 5.11.

In Figure 5.9, there are two subplots $a)$ and $b)$. The electron trajectories $r_1(t)$ (red dashed line), $r_2(t)$ (blue solid line) are plotted together with a scaled version of the external pulse (black line). The external field parameters are $F_0 = 0.3$ a.u., $\phi = 0$ a.u. with a smaller field frequency $\omega = 0.06$ a.u.. Due to the longer wavelength, the field electron returns to the ion earlier in the pulse, see Figure 5.4.

The course of the field electron in the pulse is identical in both subplots. The bound electrons are only slightly shifted due to the neighboring initial conditions. Approaching 60 a.u. the field electron returns and collides with the bound electron. The collision sequence is the same in both plots. First, the field electron returns and crosses the origin with the bound electron traveling in front of it. Then the field electron passes the bound electron which is decelerated towards the rising potential wall. The bound electron in Figure 5.9 $a)$ changes direction at the turning point, crosses back over the origin and ionizes in the opposite direction.

In Figure 5.9 $b)$, the bound electron also changes direction at the turning point and crosses back over the origin. Its binding energy is less than the strength of the saddle. In the quantum picture, the bound electron would have a finite probability to tunnel the Stark barrier. In the classical

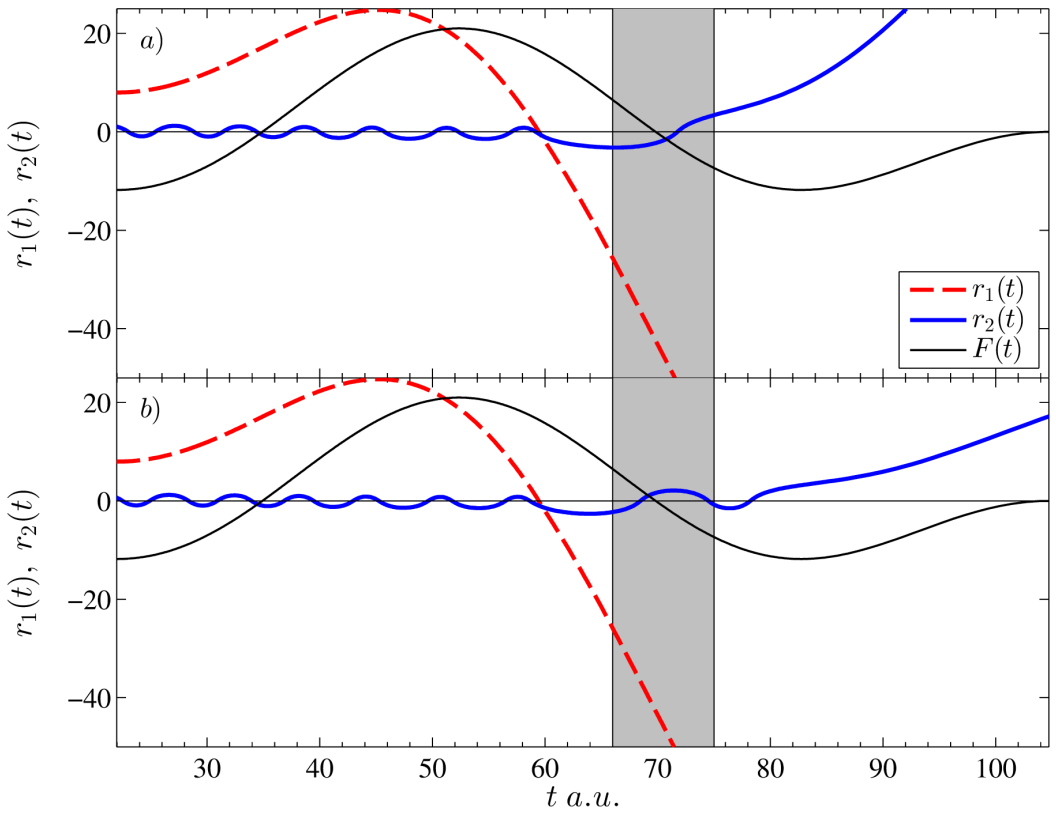

FIGURE 5.9: Time evolution of trajectories from two double ionization events. The external field $F(t)$ is represented by the black line and is scaled to fit the figures dimensions. The field parameters are $\omega = 0.06$ a.u., $F_0 = 0.3$ a.u., and $\phi = 0$ a.u.. In both $a)$ and $b)$, the field electron (red trajectories) have the same initial conditions. The bound electrons' (blue trajectories) initial conditions, for $a)$ and $b)$, are from neighboring positions in phase space. The highlighted gray region is a critical time interval where the neighboring trajectories diverge. The evolution of the bound electrons in this time interval is elaborated in Figure 5.10 for $a)$ and Figure 5.11 for $b)$.

representation, the bound electron is reflected at the turning point and performs a full oscillation before it ionizes over the Stark saddle from the third maximum in the pulse. This critical time frame, where the divergence of the trajectories of the bound electron occurs, is highlighted in gray.

A more in depth analysis of the trajectory from the bound electron in Figure 5.9 $a)$ is given via its Hamiltonian in the presence of the Coulomb potential. The time interval, highlighted in gray, is subdivided into nine time frames. The snapshots of the momentary Hamiltonian of the bound electron are shown in Figure 5.10.

In Figure 5.10, the Hamiltonian of the bound electron $H_2(t)$ (blue) and the Coulomb potential (black) is plotted in the first time frame (a). At $t_{end} = 66$ a.u., the field electron is found at $r_1(66) = -30$ a.u.. Its Hamiltonian, as it crossed the ion, were greater than the dimensions of the subplots. By $t_{end} = 66$ a.u., the bound electron performed multiple oscillations before the

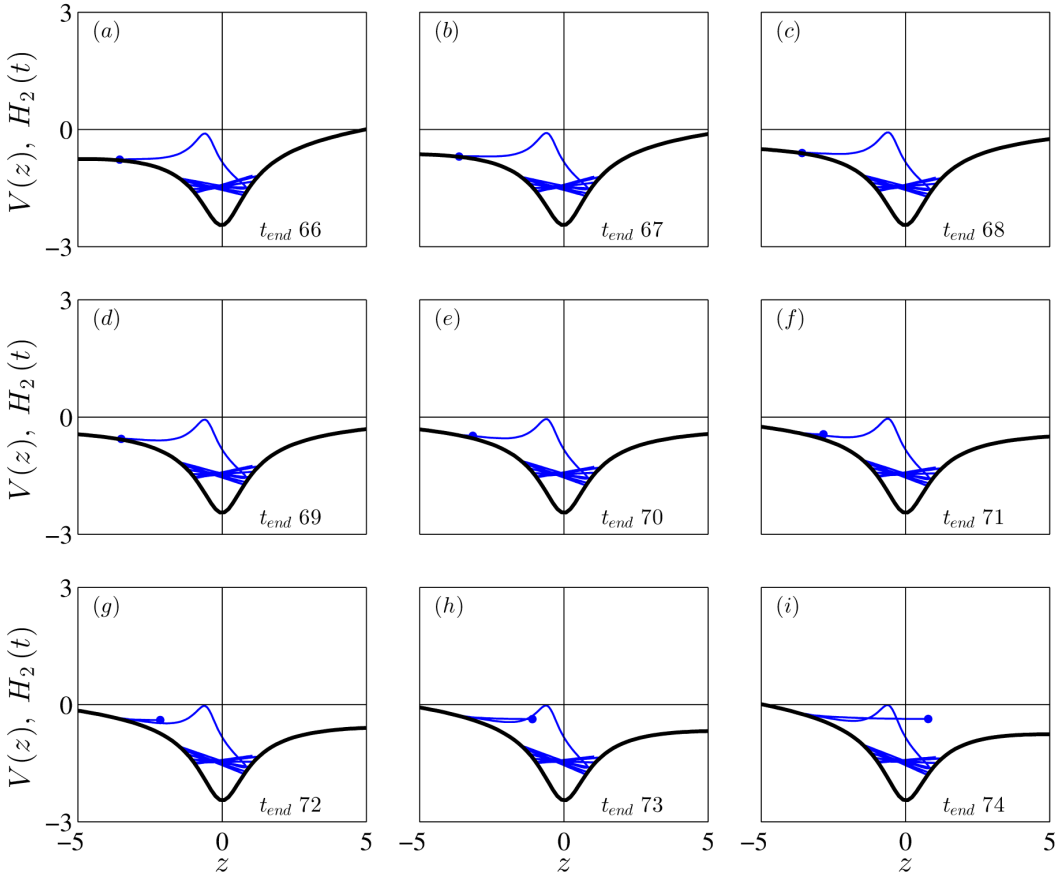

FIGURE 5.10: The time interval $t \in [66\text{ a.u.}, 74\text{ a.u.}]$ which is highlighted in gray in Figure 5.9 is subdivided into nine subplots. The Hamiltonian of the bound electron (blue), whose trajectory is given in Figure 5.9 a), is plotted alongside the Coulomb potential (black).

field electron collision at 60 a.u. and has reached the classical turning point, seen in (a). The Stark saddle is still visible. The deceleration reduces the bound electrons kinetic energy to zero and the bound electron is unable to ionize over the saddle. In (e), the bound electron has changed direction and travels toward the origin between $(e)-(h)$. In (i), the bound electron crosses the ion and has sufficient energy to ionize over the emerging Stark saddle due to the third maximum of the external field.

In Figure 5.9 b), the bound electron started from an adjacent initial condition to that of a). The Hamiltonian of that same bound electron, $H_2(t)$, during the highlighted time interval is shown in Figure 5.11. In (a), it is immediately apparent that the bound electron does not gain as much energy through the collision with the field electron. The spike in the Hamiltonian is smaller than that in Figure 5.10, therefore, it reaches the turning point at the potential wall sooner. By $t_{end} = 66$ a.u., the bound electron has changed direction and, during frames $(b)-(d)$, crosses the origin. The bound electron reaches the turning point at the opposite end at (e). There, the external pulse has a zero crossing but the bound electron has insufficient energy to ionize directly. During $(g)-(i)$, the bound electron completes a second crossing of the ion. The bound

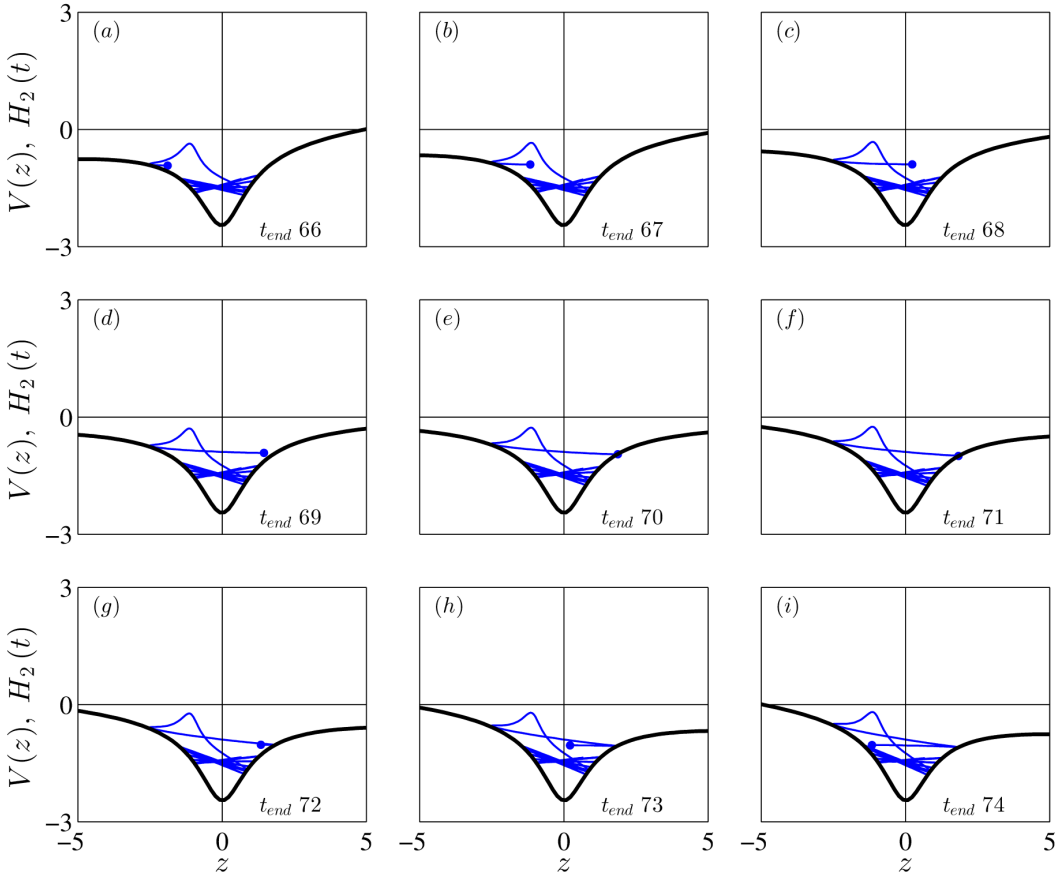

FIGURE 5.11: The time interval $t \in [66\text{ a.u.}, 74\text{ a.u.}]$ which is highlighted in gray in Figure 5.9 is subdivided into nine subplots. The Hamiltonian of the bound electron (blue), whose trajectory is given in Figure 5.9 *b*), is plotted alongside the Coulomb potential (black).

electron ionizes in the opposite direction over the Stark saddle in the potential due to the third maximum in the pulse.

5.1.5 Summary

Single-cycle pulses generate anti-parallel double ionization events from initial conditions for the bound electron from one region of phase space per field parameter constellation. When a field electron collides with a bound electron to produce double ionization, there is a high probability that a neighboring initial condition for the bound electron will also lead to double ionization. No connection to the initial conditions and the field frequency could be identified. The Coulomb potential bends proportional to the peak field amplitude. The phase space energy shell, on which the initial conditions for the bound electron are calculated, contracts with increasing field strength. Furthermore, the duration of the field electron excursion in the external field continuously decreases and the regions of phase space, where the initial conditions lead to double ionization, begin to overlap.

When a single-cycle external pulse is applied, there are very few or even no multiple collisions between the electrons depending of the laser frequency. At very high frequencies, the pulse is so short that sequential ionization is no longer a path to double ionization. The true double ionization trajectories for single-cycle pulses all result in back-to-back escape due to the electron repulsion [30]. Both electrons have similar energy according to Wannier [85].

Both electrons must be traveling in the same direction when the field electron returns to the ion. The Coulomb repulsion plays a significant role in the ionization process, especially for the bound electron. This mechanism of the inner electron was coined *Coulomb-repulsion-assisted laser acceleration*. It was found to be the mechanism for NSDI in reduced dimensional classical models [9].

There is no indication of "direct impact non-sequential ionization". Except for a frequency $\omega = 0.06$ a.u., the timing of the ionization of the bound electron coincides with the emerging saddle point in the atomic potential from the third maximum in the field. The inner electron must be at the right place, i.e. approaching the saddle as it forms in the atomic potential field.

The bound electron gains energy at the collision but not enough to directly overcome its binding energy. The situation of the Coulomb potential and the electrons' interaction facilitates single-collision anti-parallel double ionization. Using a model in which the electron-electron interaction is either neglected or over-exaggerated cannot be a reliable or even physically viable premise on which to study such phenomena.

Calculations which began at the second peak in the pulse produced only single ionization. Even at the lowest frequencies and for a large ensemble of initial conditions, no double ionization yields were registered. Parallel NSDI occurs first when the external pulse has at least two-cycles.

5.2 Two-Cycle Pulses

Investigations into double ionization from two-cycle pulses reveal more complex interaction dynamics. In the semi-classical picture, the two leading peaks of the pulse induce two Stark saddles of increasing strength in the atomic potential. This provides two initial situations for numerical calculations that may lead to double ionization.

5.2.1 Tunneling at First Field Maximum

5.2.1.1 Initial Conditions

From one parameter set, $\phi = 0$ a.u., $F_0 = 0.29$ a.u., and $\omega \in [0.045 \text{ a.u.}, 0.183 \text{ a.u.}]$, a total of 2×10^5 initial conditions for the bound electron were calculated along the energy shell. The initial conditions along the upper half of the energy shell, $p_{2,0} > 0$, are represented on the left side in Figure 5.12 and the initial conditions along the lower half of the energy shell, $p_{2,0} < 0$, on the right. Both are plotted with respect to the field frequency. The number of initial conditions per bin, which lead to trajectories that end in double ionization, are highlighted according to the color bar on the right.

For a peak field amplitude of $F_0 = 0.29$ a.u., there are no instances of double ionization for frequencies higher than $\omega = 0.15$ a.u.. Compared to Figure 5.1, Figure 5.12 has multiple clusters of neighboring initial conditions along the energy shell that lead to double ionization, especially in the frequency range $\omega \in [0.07 \text{ a.u.}, 0.12 \text{ a.u.}]$. At lower frequencies, the clusters are larger. External fields with low frequencies change slowly. At higher frequencies, the size of the clusters noticeably decreases.

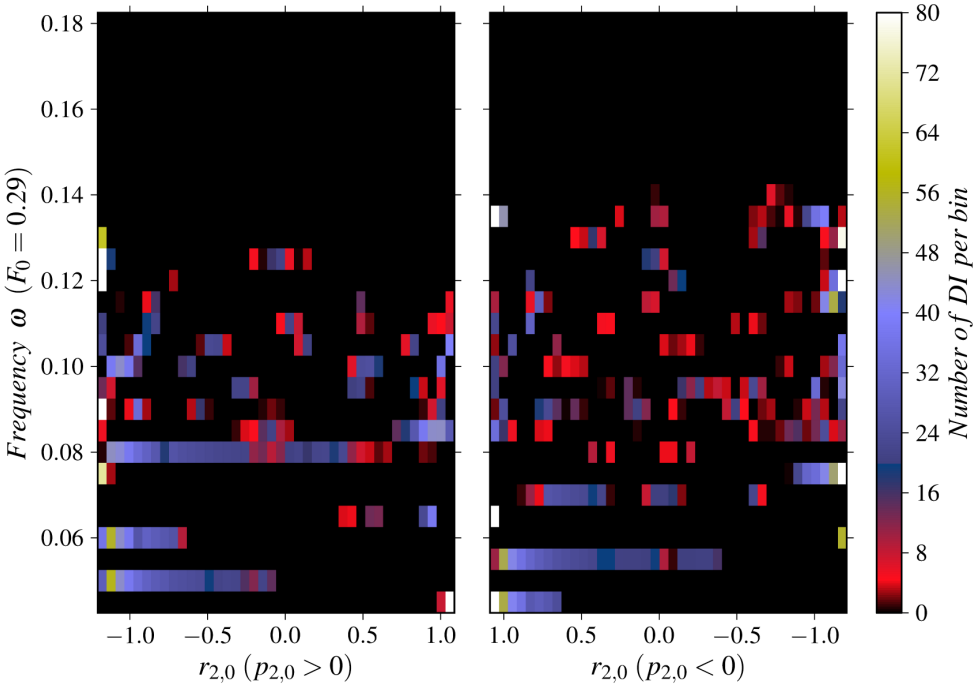

FIGURE 5.12: In a two-cycle pulse, the integration begins at the first field maximum. For one parameter set, 2×10^5 initial conditions for the bound electron, positive initial momentum (*left*) and negative initial momentum (*right*), are calculated. The number of initial conditions per bin that lead to double ionization are highlighted using an inverse color scheme. The external field used in all simulations was constant with a peak field amplitude $F_0 = 0.29$ a.u. and the phase at $\phi = 0$ a.u..

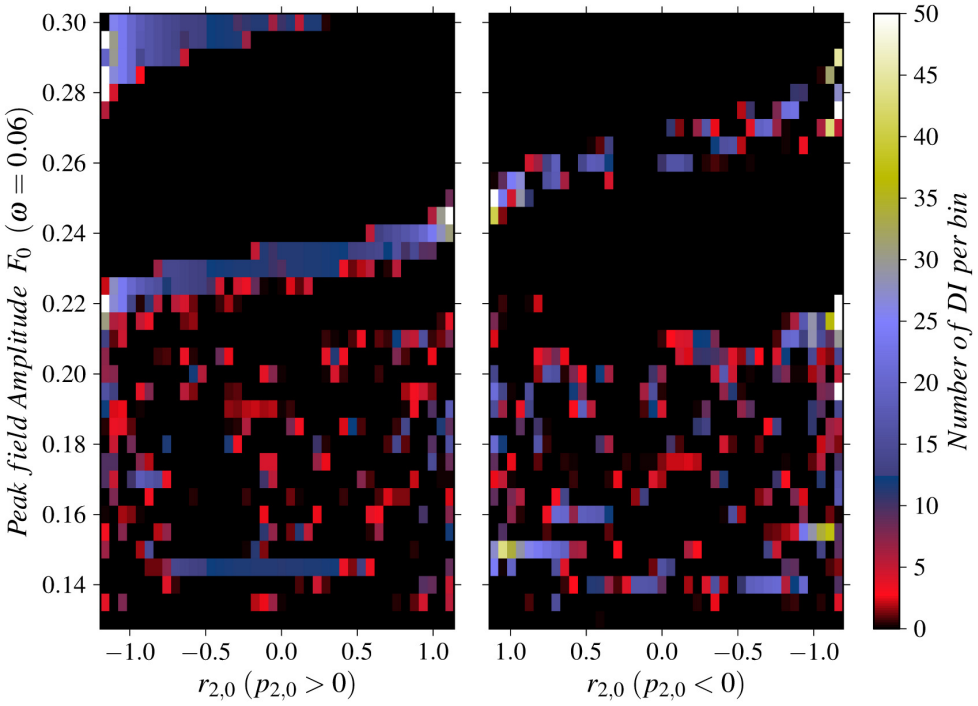

FIGURE 5.13: In a two-cycle pulse, where simulations begin at the first field maximum, trajectories from an ensemble of 2×10^5 initial conditions, for both positive initial momentum (*left*) and negative initial momentum (*right*), have been calculated for 35 different peak field amplitudes. For all results, the applied pulse had $\omega = 0.06$ a.u. and $\phi = 0$ a.u.. The number of initial conditions per bin that lead to double ionization are highlighted according to the color bar on the right.

In Figure 5.13, the initial positions of the bound electron found along the energy shell are plotted against the peak field amplitude. In all simulations, the pulse had $\omega = 0.06$ a.u.. As in Figure 5.2, the initial positions along the energy shell with positive initial momentum are seen left, and those with negative initial momentum are right. Up to a field strength of $F_0 = 0.22$ a.u., there is no noticeable pattern. The structures in the region with smaller amplitudes are disconnected and fragmentary. For fields with a peak field amplitude $F_0 > 0.22$ a.u., a connection between increasing peak field amplitudes and initial conditions along the energy shell that lead to double ionization emerges.

In simulations with constant frequency, the impact the field strength has on the double ionization process is due to the increased energy from the external pulse. At smaller pulse amplitudes, the field electron returns later to the ion with less energy. In the next chapter, it is revealed that parallel NSDI dominates in these cases. The increasing number of smaller clusters of doubly ionizing initial conditions is an indication of increased transitions between the ionization channels (single, parallel, anti-parallel NSDI). This leads to a much more complex momentum distribution.

An example of such a distribution is given in Figure 5.14. The upper left figure depicts the final positions of both electrons in configuration space. The upper right figure is the corresponding

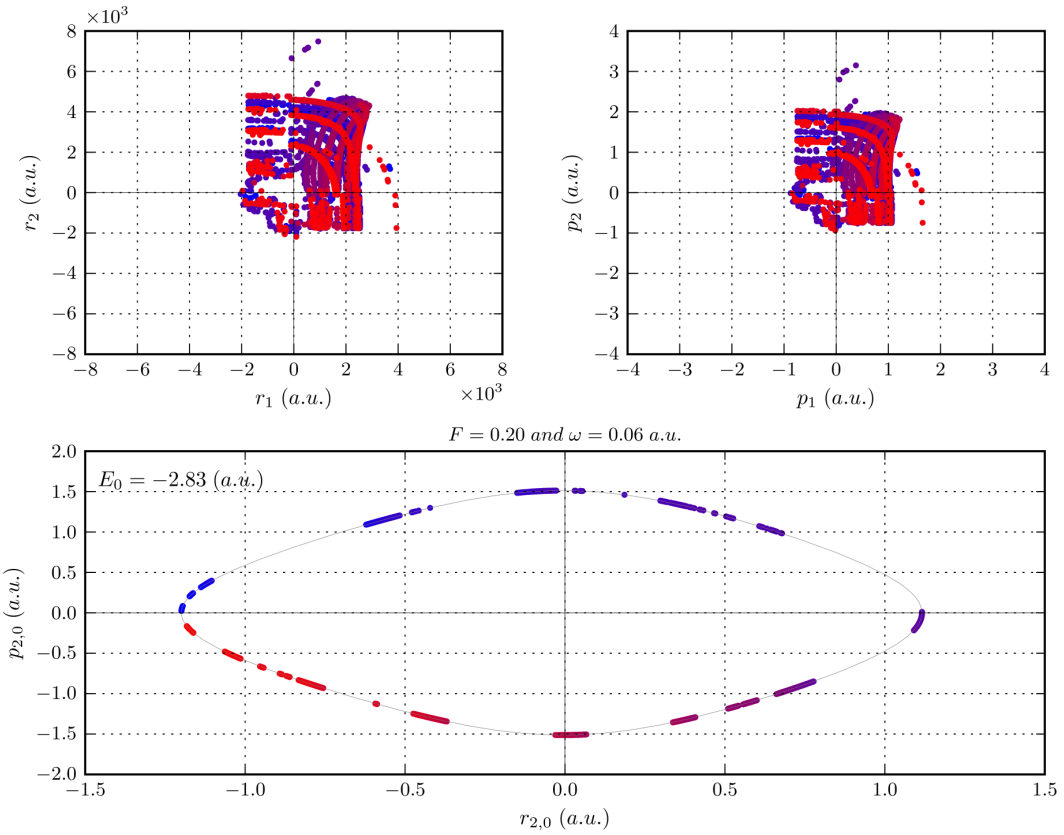

FIGURE 5.14: Using a two-cycle pulse with $\omega = 0.06$ a.u., $F_0 = 0.20$ a.u., and $\phi = 0$ a.u., double ionization events from an ensemble of 2×10^5 initial conditions are plotted. The DI-events in each figure are color-coded, with the color from one event the same in each plot. The upper two figures show the final position (*left*) and momentum (*right*) distribution of both electrons. The lower plot shows the energy shell of the bound electron. The initial conditions leading to double ionization are plotted along the energy shell in phase space.

momentum distribution. Finally, the lower plot displays the energy shell of the bound electron in phase space with color-coded initial conditions leading to double ionization. Along the energy shell, the smaller clusters of initial conditions that lead to double ionization are highlighted.

There is a distribution representing parallel double ionization. The neighboring trajectories repeatedly cross the electrons' axis coordinates. As the single ionization events are filtered out, the continuous array of neighboring trajectories is broken. At higher amplitudes, there are fewer channels to ionization.

In summary, external pulses with large frequency and amplitude, as well as small frequency and amplitude lead to many but small clusters and predominantly parallel NSDI. Pulses with small frequencies and large amplitudes generate long but fewer clusters which lead to, predominantly, anti-parallel NSDI.

All figures in this section help to identify patterns in phase space that not only lead to double ionization but might give clue as to the kind of double ionization.

5.2.1.2 Ionization

Ionization in multi-cycle external fields is complex. After discussing the initial conditions that lead to double ionization, this section deals with the ionization process itself.

Figure 5.15 comprises four histograms. Each one depicts a two-cycle external pulse (black line), with peak field amplitude $F_0 = 0.30$ a.u. and a different frequency, plotted as a function of time (in cycles). The red bar indicates when the field electron approaches the ion. The blue bars show when both electrons have positive energy and ionize anti-symmetrically. The yellow bars indicate when both electrons have positive energy and ionize symmetrically.

The frequency of the pulse used for the upper left plot was $\omega = 0.045$ a.u.. Of the four subplots, this has the longest wavelength. The field electron returns to the ion the soonest, arriving just beyond the second peak in the pulse. According to the blue bars, anti-parallel double ionization

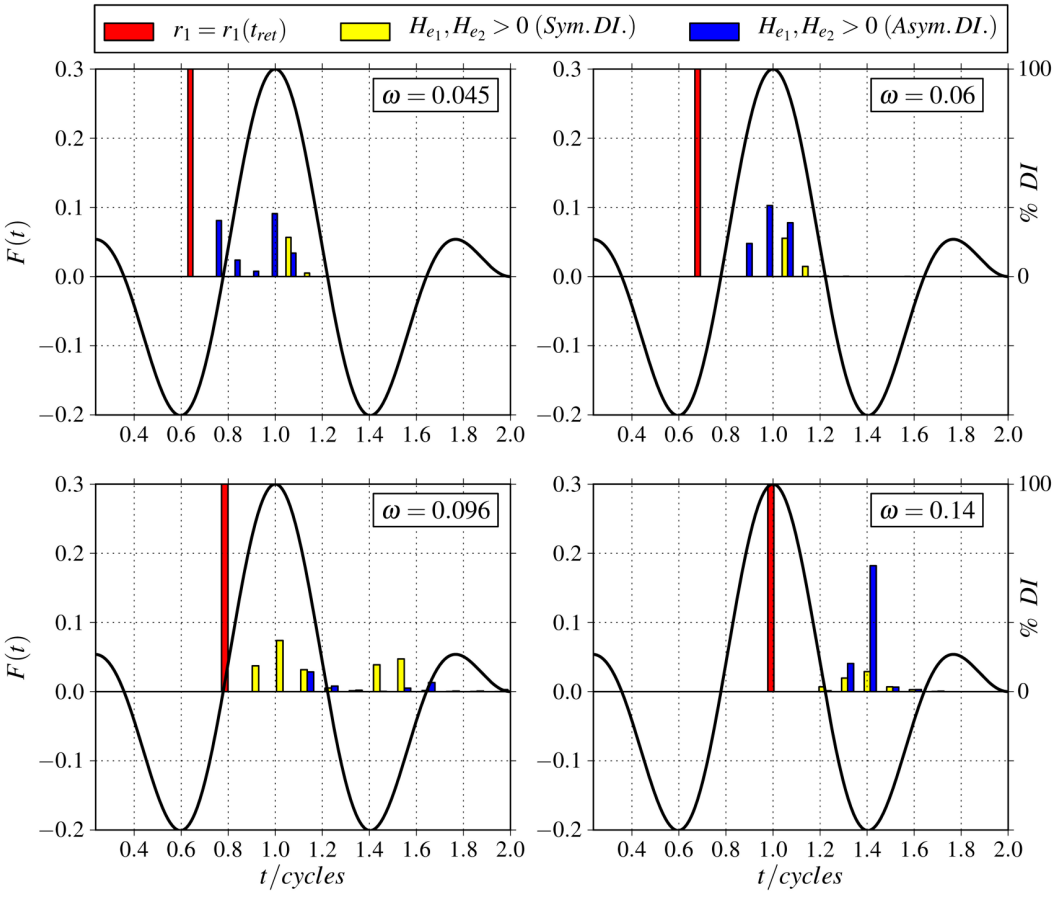

FIGURE 5.15: In each plot, a two-cycle pulse (black line), with peak field amplitude $F = 0.30$ a.u. and phase $\phi = 0$ a.u. with four different field frequencies $\omega = 0.045, 0.06, 0.096, 0.14$ a.u. is plotted. In all simulations, the field electron starts at the first field maximum. The red bar shows when during the pulse the field electron returns to the nucleus for the first time. The blue bars show at what time in the pulse both electrons have energy larger than zero and ultimately ionize anti-symmetrically. The yellow bars show when both electrons have energy larger than zero and the double ionization is parallel.

sets in after approximately one fifth of a field cycle. This coincides with the second zero-crossing of the external pulse. At the largest peak, parallel double ionization appears. After the largest peak in the pulse, there are no more ionization events. All double ionization events originate early in the pulse.

The field in the upper right plot in Figure 5.15 had a frequency $\omega = 0.06$ a.u.. The field electron returns just after the second peak of the pulse. Ionization proceeds after the second zero-crossing of the pulse. All double ionization events originate during the largest peak. Anti-parallel double ionization sets in first, just after the maximal peak. There, a weaker parallel double ionization signal is detected as well.

The lower left plot in Figure 5.15 was generated by a pulse with a frequency of $\omega = 0.096$ a.u.. The field electron returns at a zero-crossing of the pulse, before the largest peak. Once more, double ionization sets in early after approximately one fifth of a field cycle. In this parameter range, the parallel double ionization signal dominates over the anti-parallel double ionization. Double ionization events commence at different times during the entire second field cycle; parallel double ionization during peaks in the external field and anti-parallel at zero-crossings.

The lower right plot in Figure 5.15 depicts a pulse with frequency $\omega = 0.14$ a.u.. The field electron returns to the pulse at the largest peak. In this case, the field electron returns with least energy. Both parallel and anti-parallel double ionization set in during the fourth peak. The majority of the events occur at the fourth peak. This implies that the saddle point is a major crutch that supports the double ionization process, thus directly influencing the double ionization.

In all four plots in Figure 5.15, double ionization sets in at approximately one fifth of a field cycle after the field electron has returned to the ion. Except for the case of $\omega = 0.096$ a.u., the subsequent interval of the double ionization signal is found within one half of one field cycle and concentrated in the vicinity of a peak in the pulse.

From one ensemble of initial conditions, there is no long delay after the first collision until both electrons have energy larger than zero. The freed electrons are still under the influence of the external field, but, their kinetic energy is larger than the cumulative potentials acting upon them. Multiple re-scattering, as a dynamic in the electron trajectories, is not ruled out. Multiple re-collisions are not necessary for the electrons to directly ionize.

A more detailed look into the electron dynamics at initial collision, especially in the case of $\omega = 0.096$ a.u., is needed to support this assumption.

5.2.1.3 Trajectories

In this section, various electron trajectories are studied, particularly trajectories showing parallel double ionization. These trajectories were chosen out of an ensemble of 2×10^5 because their final momenta differ by $\Delta p_{1,2} < 10^{-4}$ a.u.. This condition ensures that the investigated double ionization events are parallel.

In Figure 5.16, there is one two-electron trajectory in each of the subplots. The external field used to generate these trajectories had a peak field amplitude $F_0 = 0.29$ a.u., a field frequency $\omega = 0.096$ a.u., and a phase $\phi = 0$ a.u.. The initial conditions for the bound electron for each trajectory are plotted (in black) on the phase space energy shell in Figure 5.17. All initial conditions which resulted in double ionization are plotted in green.

In this case, the field electron returns to the ion at the second zero-crossing of the external pulse, see Figure 5.15. The trajectories in the subplots $a)$, $b)$, and $i)$ stem from initial conditions from

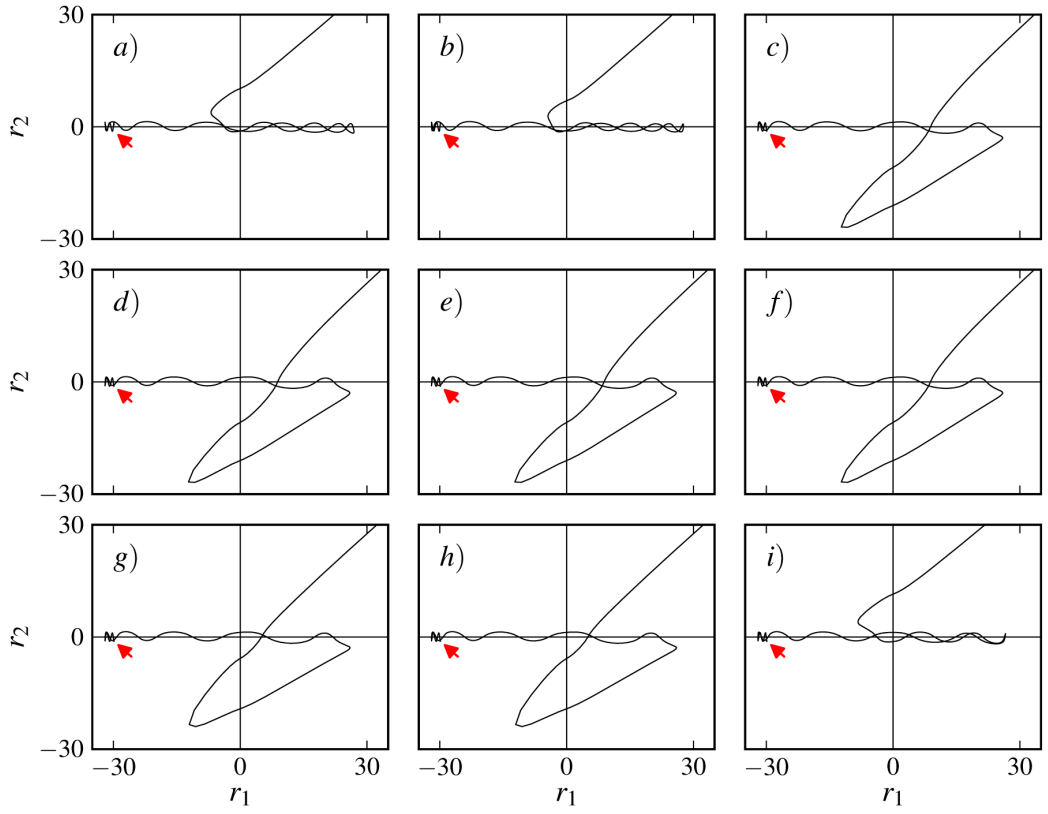

FIGURE 5.16: Each of the nine subplots shows a different two electron trajectory in configuration space. The pulse used in the simulations had two-cycles, a phase $\phi = 0$ a.u., peak field amplitude $F_0 = 0.29$ a.u., and frequency $\omega = 0.096$ a.u.. $c) - f)$ ($t_{ion} \approx 1.14$ cycle) and $g) - h)$ ($t_{ion} \approx 1.2$ cycle) each stem from different clusters of initial conditions (indicated by red arrows) that lead to double ionization. The trajectories seen in $a)$, $b)$, and $i)$ have the ionization times $t_{ion} \approx 1.53$, 1.49, 1.55 cycle respectively. The initial conditions for the bound electron are plotted in Figure 5.17. The final position and final momenta of each double ionization event is given in Figure 5.18.

different regions of phase space. The field electron proceeds to cross the nucleus and ionize in the opposite direction. The external field changes sign and the field electron is turned back to the ion. The field electron re-collides with the bound electron. The bound electron then ionizes in the direction of the saddle due to the fourth peak. Both electrons gain energy through their interaction with the field and each other. They are ionized at approximately 1.53, 1.49, and 1.55 field cycles. The electrons in $b)$ escape the soonest in the pulse. They would have more time in the field, thus acquiring the most momentum to allow them to travel the furthest. A comparison to the final position and momentum in Figure 5.18 reveals that the trajectory in $b)$ also corresponds to the event with the largest momentum.

The situation is similar in $a)$ and $i)$, except that the interaction of the electrons and the nucleus is extended. Subsequently, the time of ionization is delayed and the electrons do not gain as much energy during the tail of the pulse.

In Figure 5.16, the trajectories in $c)-f)$ and $g)-h)$ are each separate clusters of trajectories from the same region in phase space. The trajectories in $c)-f)$ ionize at approximately 1.14 field cycles. The trajectories in $f)-g)$ ionize at approximately 1.19 field cycles. The ionization dynamics in both clusters are more complex. While both electrons have energies larger than zero, they remain in the vicinity of the core for a longer amount of time. The field electron returns to the ion, interacts with the bound electron, and crosses the nucleus. Simultaneously, just as the saddle begins to emerge, the bound electron is at the opposite end of the potential well. This scenario allows the bound electron with its increased energy to escape over the

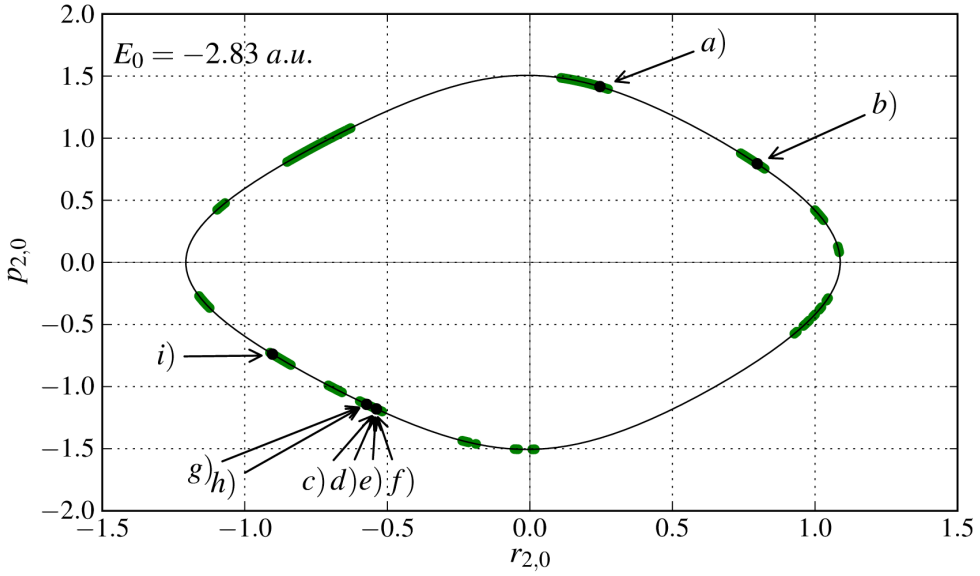

FIGURE 5.17: The phase space energy shell on which the initial conditions for the bound electrons, $(r_{2,0},\ p_{2,0})$, are found. The arrows, lettered $a)-i)$, point to the initial conditions that lead to the corresponding double ionization trajectories seen in Figure 5.16. All initial conditions for the bound electron that lead to double ionization are plotted in green. The total ground state energy of the system is $E_0 = 2.83$ a.u.

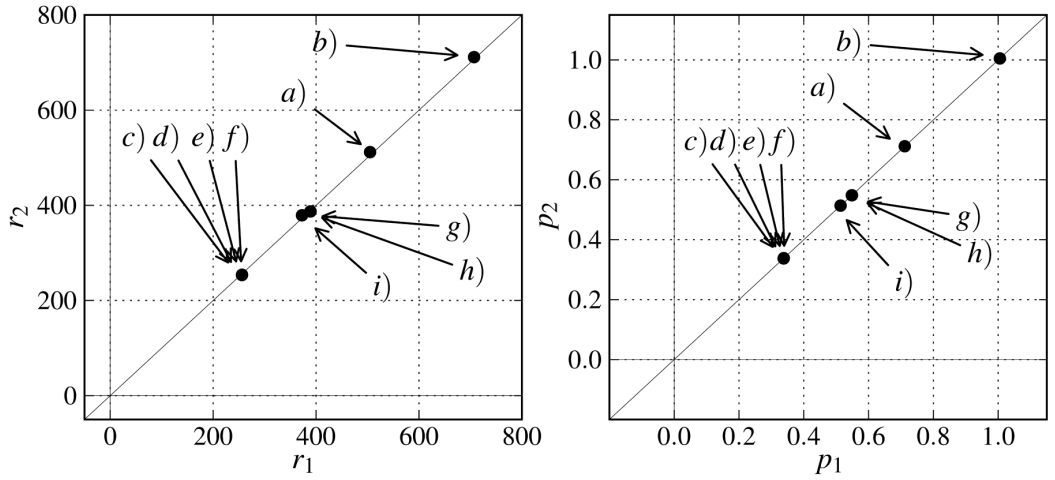

FIGURE 5.18: The final positions of the two-electron trajectories seen in Figure 5.16 in configuration space (*left*) and the final momentum of the electrons in momentum space (*right*). The double ionization events were specifically chosen as their final momenta differs by less than $\Delta p_2 = 4 \times 10^{-4}$.

saddle. The bound electron does not have sufficient energy to immediately escape the attraction of the nucleus before it turns back to the core. The field electron makes a final pass across the core and both electrons escape. The situation is similar with the pair of trajectories $g) - h)$. The electrons, in the both scenarios, have positive energy at 1.19 field cycles. This is the time when their trajectories are in the fourth quadrant. The difference between both clusters is that the distance between the electrons and the nucleus is smaller.

In Figure 5.19, two different clusters of trajectories with ionization times at the very end of the external pulse, $t_{ion} = 1.9$ field cycles, are plotted. Anti-parallel double ionization dominates in

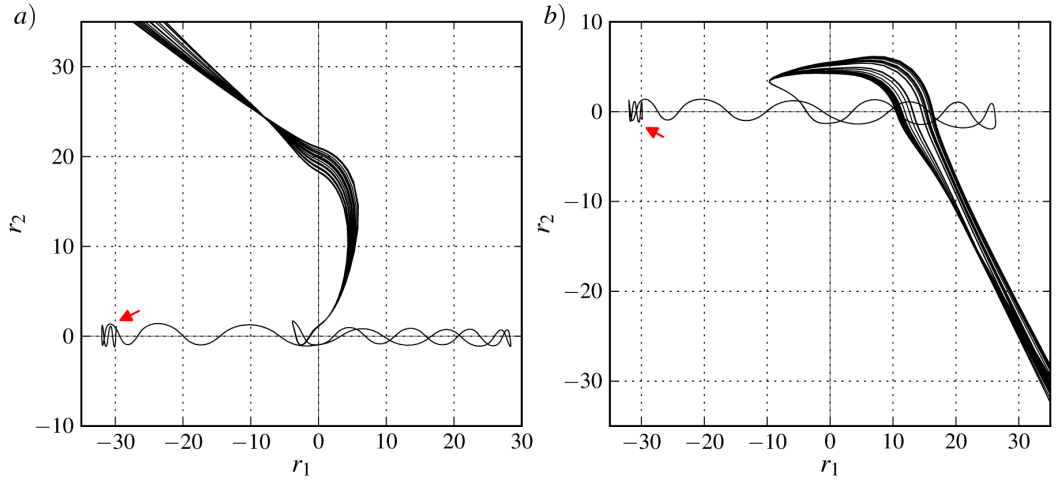

FIGURE 5.19: Two clusters of trajectories from neighboring initial conditions (red arrow). Generated from a two-cycle external driving field with parameters $F = 0.29$ a.u., $\omega = 0.096$ a.u., $\phi = 0$ a.u., they show anti-parallel double ionization which occurs from the tail of the pulse, $t_{ion} = 1.9$ field cycles.

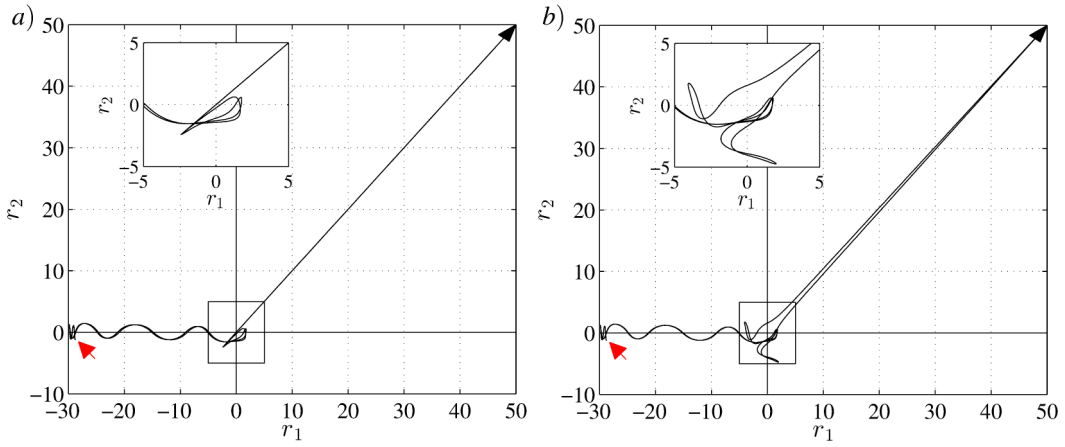

FIGURE 5.20: Trajectories generated using a two-cycle pulse and beginning at the first field maximum. The field parameters are $F_0 = 0.30$ a.u., $\omega = 0.14$ a.u., and $\phi = 0$ a.u.. The red arrows point to the initial positions of both electrons. a) show two examples of trajectories which represent parallel double ionization. The divergence in the progression of both trajectories in a) occurs near the nucleus. This is magnified in the inset. Both trajectories simultaneously cross the origin before symmetrically ionizing over the potential barrier. The trajectories in b) are also very similar up to their interaction at the nucleus. There, both electrons leave in succession. Although the double ionization is not exactly symmetrical, the electrons position and momentum become increasingly similar.

that region, see Figure 5.15. The start of the trajectories is indicated by the red arrow. Both clusters initially resemble trajectories a), b), and i) in Figure 5.16. However, the trajectories do not continue in the first quadrant. The trajectories in a) cross over into the second quadrant. The trajectories in b) go into the fourth quadrant, all representing anti-parallel double ionization.

Pulses with higher frequencies generate trajectories with less complex dynamics. In Figure 5.20, each plot has two similar trajectories. The external field parameters were $F_0 = 0.30$ a.u., $\omega = 0.14$ a.u., and $\phi = 0$ a.u.. All initial conditions for the trajectories were found within an interval of $\Delta r_{2,0} = 0.086$ a.u. on the energy shell in phase space. Their initial positions in configuration space are indicated by the red arrows. With such a high frequency, the field electron returns to the core when half the pulse has passed, i.e. at the largest peak in the pulse. This can be seen in Figure 5.15. The interaction between the two electrons is contained near the nucleus. In a), when the field electron returns to the ion, the bound electron is traveling in the same direction. Both electrons complete one orbit across the nucleus. The symmetric configuration of the electrons and the nucleus allows the electrons to cross the saddle point simultaneously.

In Figure 5.20 b), the two trajectories begin with neighboring initial conditions to those used in a). At the origin, each trajectory turns into either the second or fourth quadrant. The magnification of the electrons' interaction near the nucleus is seen in the inset in the upper left corner of the plot. The time dependence of the potential field and the relatively high field strength and frequency cause almost identical trajectories to diverge. Both electrons complete a second cycle about the nucleus before ionizing in the same direction and in succession. After propagating 50

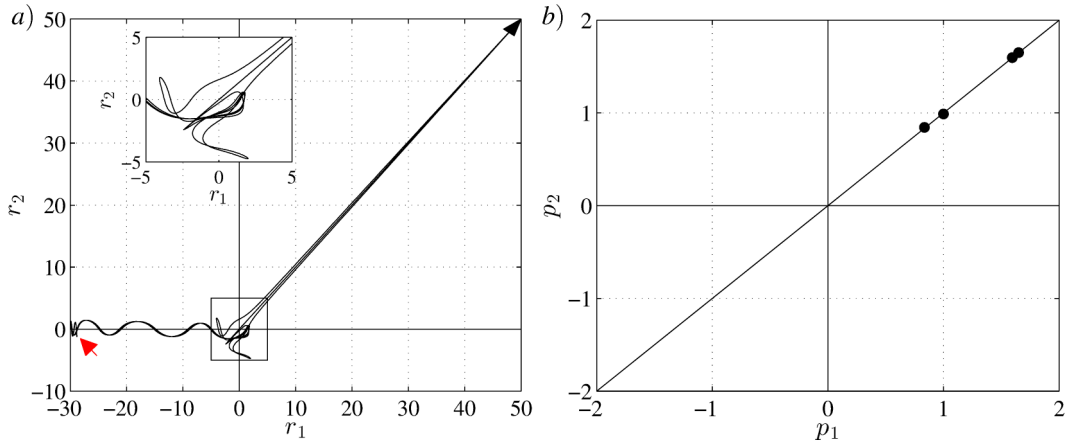

FIGURE 5.21: *a*) all four trajectories from Figure 5.20 are displayed. The red arrow indicates the initial positions of the electrons which are all found within a region of $\Delta r_{2,0} = 0.086$ a.u. in phase space. In *b*) the final momentum is given for the four double ionization events. The two final momenta with ≈ 1.8 a.u. stem from the trajectories shown in Figure 5.20 *a*), whereas the two final momenta ≈ 1 a.u. are from the ionization sequence represented in the trajectories from Figure 5.20 *b*).

a.u., both trajectories converge onto the diagonal. The momentum distribution of all four double ionization events is given in Figure 5.21 *b*). Each point along the diagonal indicates the final momentum of both electrons in the four double ionization events described above.

The trajectories were chosen as examples of symmetric electron escape. Since they run along or converge onto the diagonal indicates not only a symmetric spatial configuration but also a symmetric configuration in momentum. The final momentum of both electrons is $p_1 = p_2$. The two trajectories that run along the diagonal in Figure 5.21 *a*) have the largest momenta with $p_{1,2} \approx 1.8$ and the two trajectories with the additional cycle about the nucleus have final momenta of $p_{1,2} \approx 1$.

An external pulse with $F_0 = 0.21$ a.u. and $\omega = 0.06$ a.u. generated the trajectories plotted in the nine subplots in Figure 5.22. The trajectories were, again, chosen because their final momenta was $\Delta p_{1,2} < 4 \times 10^{-4}$ a.u.. The trajectories in subplots $b) - c)$ and $g) - h)$ do not have neighboring initial positions. Nevertheless, the initial positions of the bound electrons are found in an interval $\Delta r_{2,0} = 4.25 \times 10^{-4}$ a.u.. The trajectories in subplots $e)$, $f)$ and $a)$, $i)$ stem from the same cluster of initial conditions of the bound electron. The red arrow point to the joint initial positions of the electrons. The initial conditions for the bound electron (black) are plotted separately on the phase space energy shell in Figure 5.23. All initial conditions leading to double ionization for this parameter set are plotted in green.

The *ab initio* assumption that one electron has tunneled and emerged on the opposite side of the potential barrier generated from the first field maximum in the two-cycle pulse results in a small propagation for the field electron as the first and last peak of the pulse are the weakest. In all cases except for *e*), the field changes sign and the field electron returns to the ion and crosses

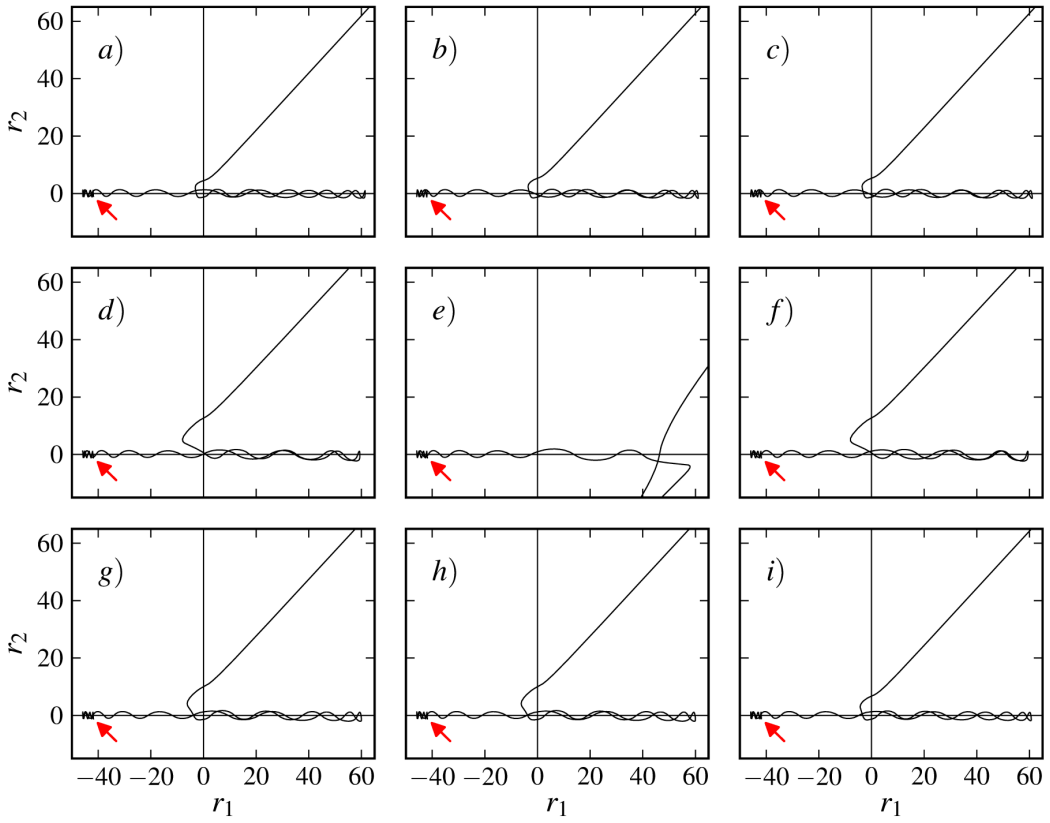

FIGURE 5.22: The nine subplots show two-electron trajectories in configuration space. The pulse used in the simulations had two cycles, a phase $\phi = 0$ a.u., a peak field amplitude $F_0 = 0.21$ a.u., and a frequency $\omega = 0.06$ a.u.. The trajectories in $b) - c)$ and $g) - h)$ start from initial conditions (red arrows) which are not directly adjacent but from a region within $\Delta r_{2,0} = 4.25 \times 10^{-4}$ a.u. The trajectories seen in $e), f)$ and $a), i)$ originate from the same cluster of doubly ionizing initial conditions. The corresponding initial conditions for the bound electron are plotted in Figure 5.23. The final position and final momenta of each double ionization event is given in Figure 5.24.

the core. The field electron completes one further cycle in the external field, extending a further 20 a.u. from its original position, before returning to the ion.

The trajectories in Figure 5.22, $a) - c)$ and $g) - i)$, have a similar propagation in the external field. When the field electron approaches the ion, the bound electron just turned at the classical turning point. They then travel across the nucleus in the same direction. The bound electron crosses the origin first, followed closely by the field electron. The short excursion into the third quadrant demonstrates their parallel course. The bound electron reaches the classical turning point first, turns and crosses the nucleus again. After the field electron turns and crosses the origin, both electrons are propagating in the same direction. They are slightly offset but eventually converging on the diagonal. Their final positions are plotted in Figure 5.24.

The anomalous trajectory in plot $e)$ in Figure 5.22, resembles the trajectories $c) - h)$ in Figure 5.16. However, in this case, the field electron does not get pulled back all the way to the ion. The trajectory initially resembles single ionization. The larger oscillations show that the

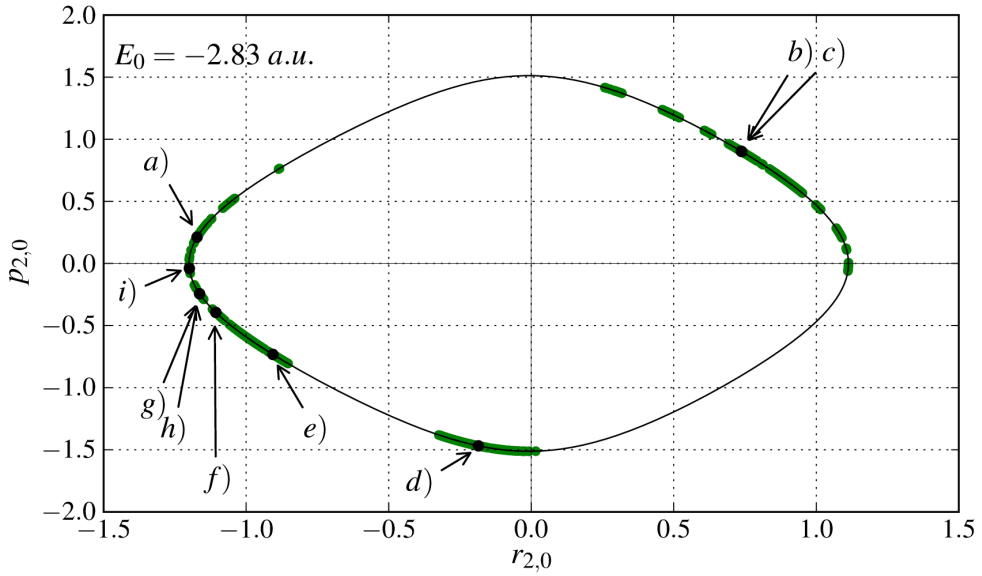

FIGURE 5.23: The phase space energy shell on which the initial conditions for the bound electrons, $(r_{2,0},\ p_{2,0})$, are found. The arrows, lettered $a)-i)$, point to the initial conditions, in black, that lead to the corresponding double ionization trajectories seen in Figure 5.22. All initial conditions that lead to double ionization are plotted in green. The total ground state energy of the system is $E_0 = 2.83$ a.u.

bound electron has gained significant energy after the initial interaction. When the field changes sign, the bound electron may cross the potential barrier. Simultaneously, the field electron is confronted with a rising potential barrier and at approximately 60 a.u., it turns and propagates back in the direction of the ion. The field changes sign before the field electron reaches the nucleus. Both electrons change direction and ionize, with the bound electron approximately 40 a.u. behind the field electron. At the end of the calculation time, which is 12 times the pulse

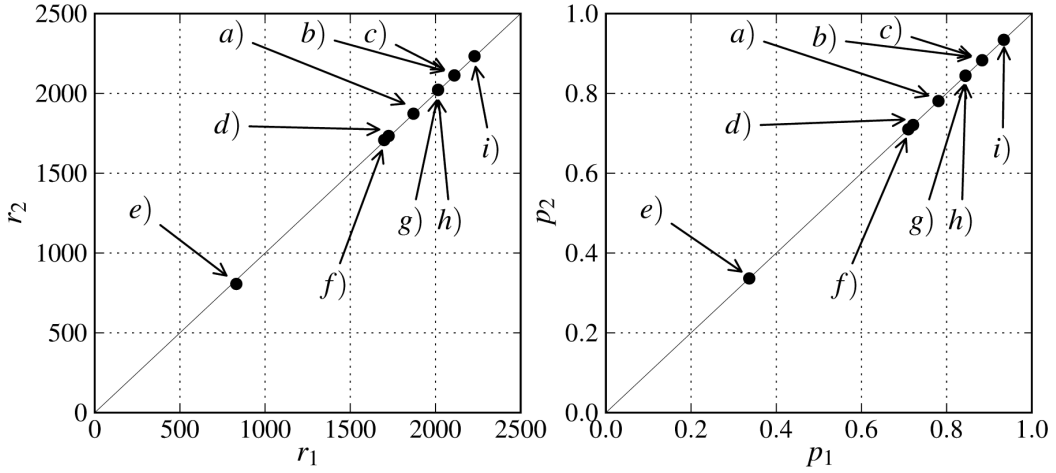

FIGURE 5.24: The final positions of the two-electron trajectories seen in Figure 5.22 in configuration space (*left*) and the final momentum of the electrons in momentum space (*right*). The double ionization events were especially chosen as their final momenta differ by less than $\Delta p_2 = 4 \times 10^{-4}$ a.u..

duration, the system is in a symmetric configuration. The final positions and momentum are given in Figure 5.24.

While both $d)$ and $f)$ in Figure 5.22 look similar, there are features in both that deserve individual study. In $f)$, after the second excursion, the field electron, returns to the ion and crosses the origin at precisely the same moment as the bound electron. However, the bound electron moves anti-parallel to the oncoming field electron. In $d)$, at the first *and* second crossing, both electrons are traveling anti-parallel when traversing the core. In both cases, their mutual repulsion does not seem to affect their trajectories. The field electron turns at the classical turning point and follows the bound electron beyond the nucleus. By the end of the full simulation, both electrons are on the diagonal, both in configuration and momentum space. Their final momenta differ by less than $\Delta p_2 = 4 \times 10^{-4}$ a.u.. The escape of both electrons did not need to occur symmetrically for the final result to be parallel double ionization, see Figure 5.24.

5.2.2 Tunneling at Second Field Maximum

In a two-cycle pulse, there are two peaks that set the initial situation for double ionization. In this section, results from simulations starting at the second peak in the strong short pulse are presented.

5.2.2.1 Initial Conditions

Starting at the second peak in the external field, with $F_0 = 0.29$ a.u., $\phi = 0$ a.u., and $\omega \in [0.045 \text{ a.u.}, 0.18 \text{ a.u.}]$, a set of 2×10^5 initial conditions are calculated for each electron. Varying the frequency, for constant peak field amplitude, has one distinct advantage in that all initial conditions are the same for all simulations. The peak field amplitude was chosen because, in combination with most frequencies, the highest number of double ionization events were calculated. At frequencies lower than $\omega = 0.075$ a.u. no double ionization was observed.

In Figure 5.25, the initial positions of the bound electron are plotted against each field frequency. On the left, the bound electrons' initial momentum is positive ($p_{2,0} > 0$), while on the right it is negative ($p_{2,0} < 0$). The number of initial conditions of the bound electron per bin that lead to double ionization are highlighted according to the color bar on the right.

Increasing the frequency of the field, reduces the number of oscillations the bound electron can complete before the field electron returns to the ion. The shorter the pulse, the smaller the extension of the field electron in the pulse. Once the field electron returns and the bound electron is in an advantageous situation, double ionization is a likely result. In this case, closely neighboring initial conditions of the bound electron will most likely also lead to double ionization as well. This is seen in the highlighted bars in Figure 5.25.

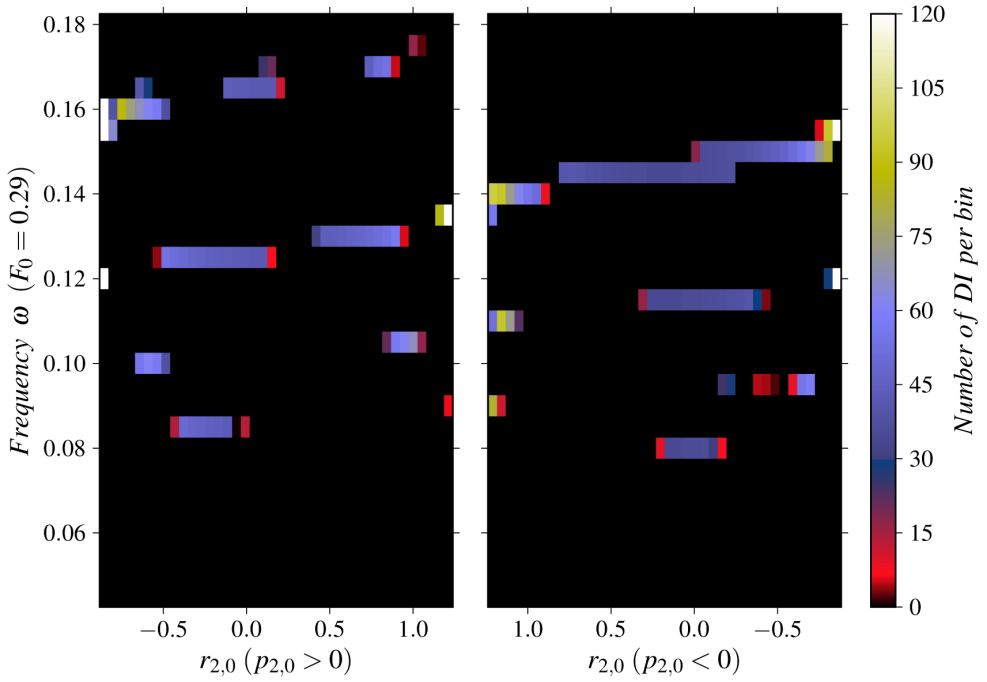

FIGURE 5.25: For a two-cycle pulse where tunneling occurs at the second field maximum, the number of initial conditions for the bound electron per bin which lead to double ionization for different field frequencies are highlighted. The external field used in all simulations was constant with $F_0 = 0.29$ a.u..

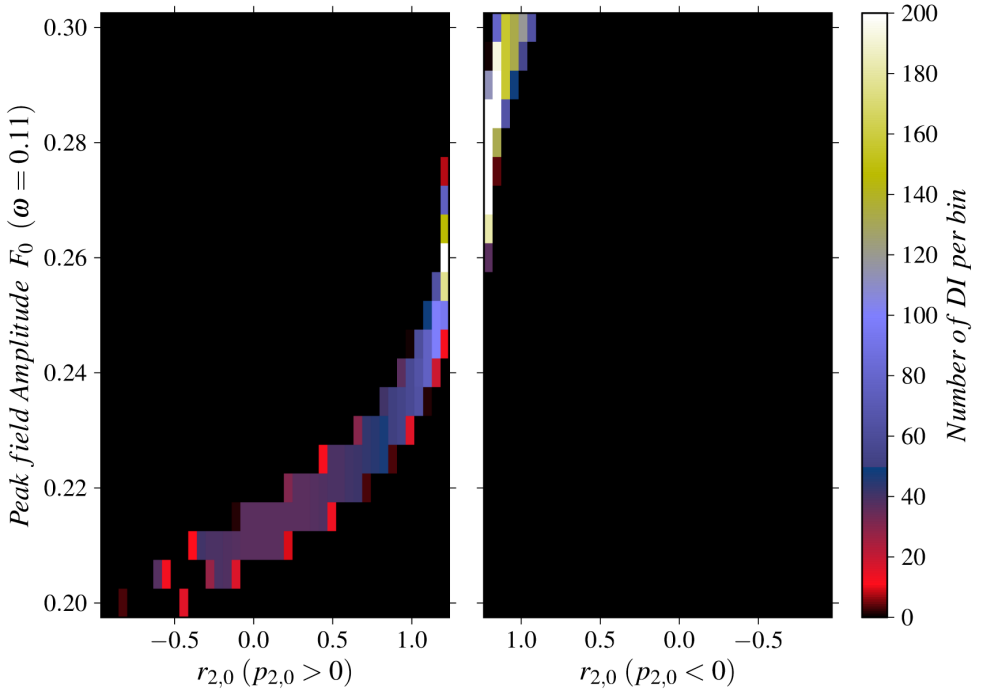

FIGURE 5.26: For a two-cycle pulse where simulations begin at the second field maximum, trajectories from an ensemble of 2×10^5 initial conditions for both positive initial momentum (*left*) and negative initial momentum (*right*), have been calculated for 21 different peak field amplitudes. For all results, the applied pulse had a frequency of $\omega = 0.11$ a.u.. The number of initial conditions per bin that lead to double ionization are highlighted according to the color bar on the right.

In Figure 5.26, the initial conditions of the bound electron and an array of peak field amplitudes $F_0 \in [0.20 \text{ a.u.}, 0.30 \text{ a.u.}]$ are presented in a two-dimensional histogram. In all simulations, the field frequency was constant at $\omega = 0.11$ a.u.. Double ionization was not found at peak field amplitudes below $F_0 = 0.20$ a.u..

There is a connection between initial conditions of the bound electron and the peak field amplitude. The highlighted curve resembles that seen in Figure 5.2. The slope is steeper. The energy shell along which the initial conditions are found contracts with increasing amplitude because the strength of the maximum bends the Coulomb potential accordingly.

5.2.2.2 Ionization

In this section, the results from the analysis into the ionization dynamics arising between two electrons propagated by a two-cycle pulse starting at the second maximum are presented. After the initial maximum, the subsequent peak in the field must be of the same order or larger for successful double ionization. If the following maxima is smaller than the initial one, no double ionization is observed.

In Figure 5.27, four plots are shown, each generated with a different frequency. The two-cycle pulse with peak field amplitude $F_0 = 0.28$ a.u. and phase $\phi = 0$ a.u. is represented with a black line. The intersecting red bar denotes when the field electron has returned to the ion after its excursion in the field. The yellow bars show the time when both electrons have positive energy and ionize parallel. The blue bars represent the time when both electrons have positive energy and ionize anti-parallel. The strength of the double ionization signal is given on the right of the plots.

The upper left plot, generated with $\omega = 0.085$ a.u., only has a parallel double ionization signal. It has the largest gap between the field electrons return and double ionization. The double ionization signal is found at the last two zero-crossings of the pulse. In the following section, an example trajectory with this parameter set is presented and discussed.

In the plot with $\omega = 0.11$ a.u., the field electron returns to the core at 1.2 cycles. Both electrons are ionized by the following zero-crossing in the pulse. The plots generated with high frequencies, all double ionization events are anti-parallel. Furthermore, the time-span between the field electrons' return and double ionization decreases.

The time intervals, when both electrons ionize, has a comparatively short duration. Double ionization does not occur instantaneously but also not over the course of the entire pulse. It is contained in a small interval, approximately a tenth of the pulse.

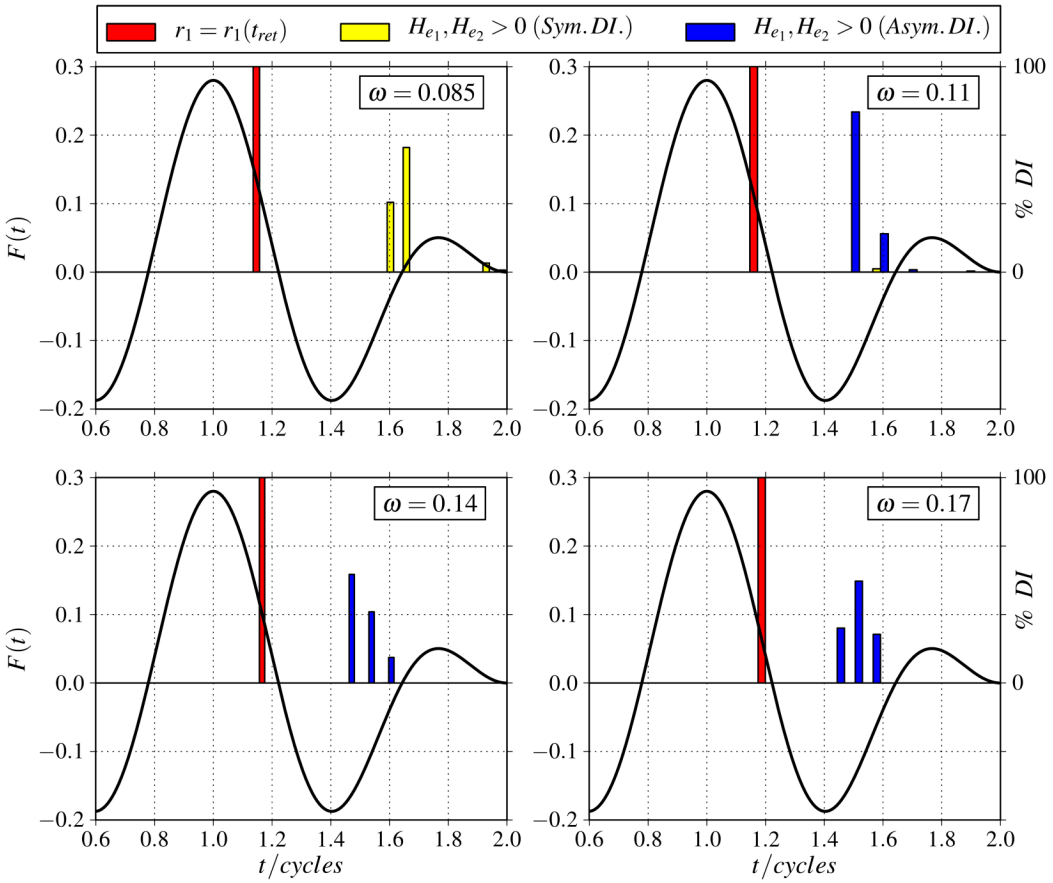

FIGURE 5.27: A two-cycle pulse (black curve), with $F_0 = 0.28$ a.u. and $\phi = 0$ a.u., is plotted with four different field frequencies $\omega = 0.085, 0.11, 0.14, 0.17$ a.u.. The red bar denotes when the field electron arrives at the edge of the Coulomb well. The blue bars show when both electrons have positive energy and ionize anti-symmetrically. The yellow bars represent when both electrons' energy is larger than zero and ionize parallel.

5.2.2.3 Trajectories

A long and short wavelength version of an external two-cycle pulse was used to generate two sample trajectories using the parameter configurations found in Figure 5.27. The difference between the parallel (low frequencies) and anti-parallel (high frequencies) double ionization is the primary focus.

The example trajectory from the low frequency ($\omega = 0.085$ a.u.) pulse is given in Figure 5.28. The initial positions of the field electron and the bound electron are indicated to by the red arrow. Following the field electrons excursion in the external pulse, it returns to the ion where it interacts with the bound electron before ionizing. The bound electron completes two additional oscillations in the potential before ionizing in the same direction as the field electron. The escape is parallel, but sequential. The low frequency double ionization has the largest time interval between the field electron's return and final double ionization. This explains the large gap between collision and double ionization in the upper left subplot of Figure 5.27.

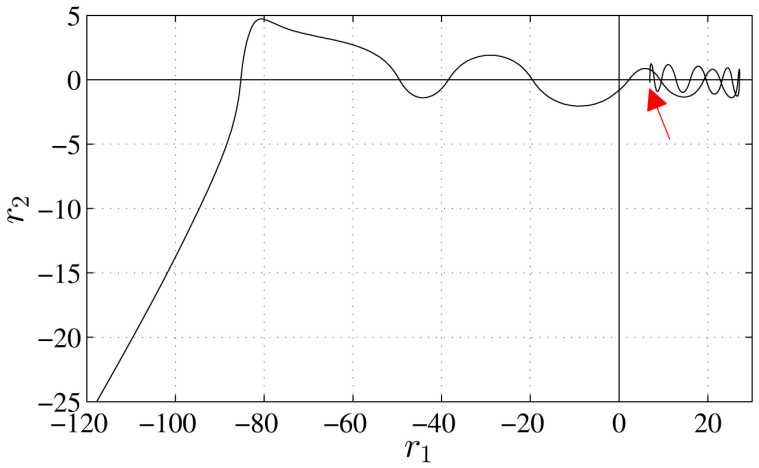

FIGURE 5.28: An example two-electron trajectory generated from a two-cycle external pulse. Calculations began at the second maximum in the pulse. The peak field amplitude is $F_0 = 0.28$ a.u., frequency $\omega = 0.085$ a.u., and phase $\phi = 0$ a.u.. The parallel double ionization is sequential.

An example trajectory from the high frequency ($\omega = 0.14$ a.u.) pulse is seen in Figure 5.29. In this case, double ionization is anti-parallel. These trajectories are very similar to those from a single-cycle pulse. The initial positions of the bound and field electron are marked with the red arrow. The field electron returns to the ion. It travels across the nucleus together with the bound electron, in the same direction, before ionizing. The bound electron crosses the origin once more before leaving over the emerging saddle in the combined Coulomb and external field. The escape is anti-parallel. As can be seen from the corresponding plot in Figure 5.27, the high-frequency double ionization has the shortest time interval between the field electron return and final double ionization.

There are instances of non-sequential parallel double ionization in simulations using a two-cycle

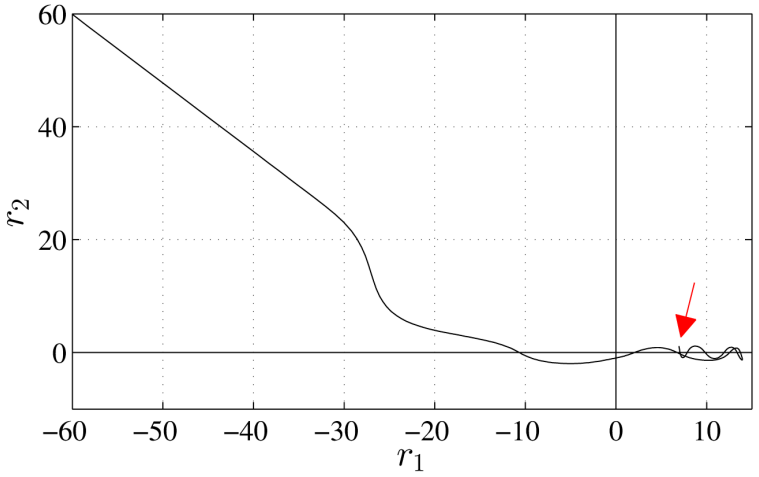

FIGURE 5.29: An example two-electron trajectory from a two-cycle field, with $F_0 = 0.28$ a.u., $\omega = 0.14$ a.u., and $\phi = 0$ a.u., depicts anti-parallel double ionization.

pulse. Calculations starting at the first field maximum yield parallel double ionization in a large set of parameters. Calculations starting at the second maximum, parallel double ionization is generated from a limited set of parameters.

Chapter 6

Frequency Dependency

In Chapter 1, the groundbreaking experiments which were introduced measured the double ionization yields as a function of field intensity. The double ionization yields could not be predicted by the SAE approximation and the correlated nature of the escape at low field intensities was revealed. The "knee" structure in the ionization yields as a function of laser intensity marks the transition from correlated double ionization at lower to uncorrelated double ionization at higher field intensities.

The wavelength dependency into the double ionization yields has not been as rigorously studied as the intensity dependency. In 1993, the wavelength dependence on the non-sequential double ionization of helium was measured [49]. For a small wavelength $\lambda = 248$ nm ($\omega = 0.183$ a.u.), no enhancement of the double ionization yields were observed. An enhancement of the double ionization yields as a function of laser intensity was found for a long wavelength $\lambda = 745$ nm ($\omega = 0.06$ a.u.).

In 1998, the wavelength dependence of NSDI of argon was measured [55]. For a large range of wavelengths, a peak in the double ionization yields was found near $\lambda = 600$ nm ($\omega = 0.076$ a.u.). There are two effects that influence the frequency dependency in the double ionization yields. The first is the ponderomotive energy, $U_p \propto F_0^2 \omega^{-2}$, i.e. the energy that an electron gains from an excursion in an external field of amplitude F_0 and frequency ω. Non-sequential double ionization is limited for large frequencies (short wavelengths). The second effect of the field frequency is that it determines the duration of the field electrons' propagation in the external field before it returns to its parent ion. In the case of an high-frequency field, the electron spends relatively little time in the field. Therefore, it is less likely to return with very different conditions from when it started out. In the quantum picture, this is manifested by the diffusion of the electron wave packet: In a laser field with a longer wavelength, the width of the wave packet of the first electron when it returns to the ion is much wider since an electron travels much longer in a field with a large wavelength.

In 2003, Chen *et al* calculated the wavelength dependency of NSDI in neon via classical electron trajectories [18]. They determined that for decreasing wavelength, the ratio Ne^{2+}/Ne^{+} increases as well. This seemed to be in direct conflict with previous results. By studying the electron trajectories, they were able to separate direct versus delayed, i.e. after 0.5 field cycles, double ionization events and discovered that the delayed double ionization events dominate for short wavelengths. It was suggested that a field-assisted double ionization mechanism at short wavelengths was responsible for this. More recently, studies into the wavelength dependency of NSDI in argon were undertaken [35, 47].

The primary focus in this chapter is the effect of the different field frequencies on the double ionization process. This cannot be done while neglecting the effect of the different amplitudes.

6.1 Single-Cycle Pulses

In the previous chapters, it was shown that single-cycle pulses are advantageous due to the simplicity of the ionization dynamics. When the field electron returns to the parent ion, there is only one further peak in the pulse which also is the weakest one.

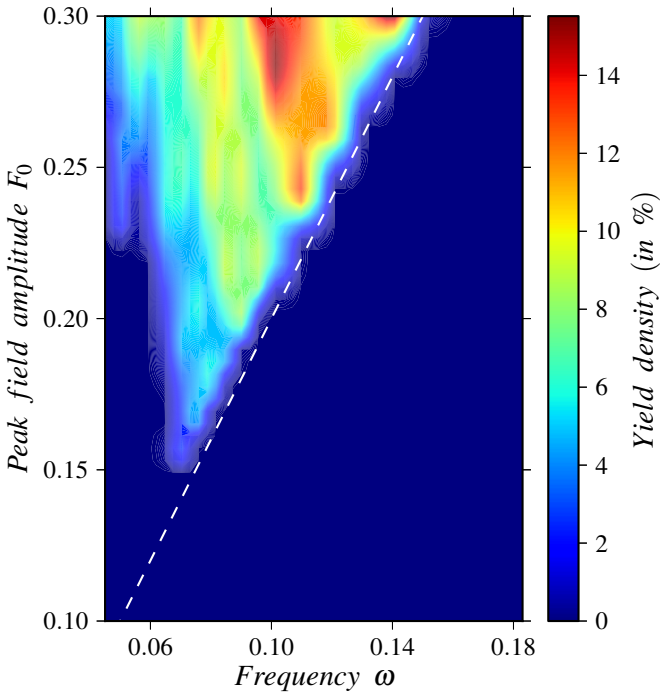

FIGURE 6.1: A histogram of the double ionization yield density (in %) from an ensemble of 2×10^5 initial conditions generated by an external single-cycle pulse using a range of peak field amplitudes and field frequencies. The white dotted line shows the boundary of $U_p = 1$ a.u. which the field electron gains while in the pulse. The slope of the line is 2.0 a.u..

Figure 6.1 is a two-dimensional interpolated histogram of the field frequency and field amplitude. For each set of peak field amplitudes F_0 and frequencies ω, an ensemble of 2×10^5 initial conditions is individually calculated. Each simulation starts with the same initial conditions for the field electron. It is positioned just outside the potential barrier which emerged due to the first field maximum with zero momentum. In each simulation, for each set of F_0, ω, the energy of the field electron when it returns to the core is very similar.

Calculations beyond a peak field amplitude of $F_0 = 0.30$ a.u. would be pointless for studying correlated double ionization as the energy of the Stark barrier would be less than the ionization potential of the bound electron. The bound electron could auto-ionize.

The intensity of the double ionization yields is given in percent according to the color bar on the right. It is calculated via the double ionization yields per bin. There are vertical structures within the region of double ionization. Across the horizontal, for each peak field amplitude, there are fluctuations in the double ionization yields across the domain of the frequencies. The white dotted line in Figure 6.1 divides the parameter regions where double ionization occurs from where it does not. It has a slope of $F_0/\omega = 2.0$ a.u. and the ponderomotive energy $U_p = 1$ a.u..

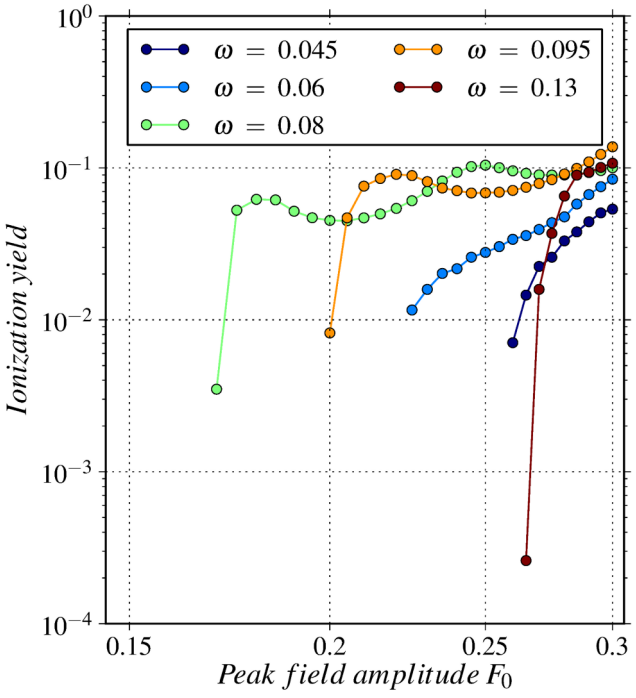

FIGURE 6.2: A double logarithmic plot of the ionization yields as a function of the peak field amplitudes obtained from an ensemble of 2×10^5 initial conditions, propagated in a single-cycle pulse for five different field frequencies. For the lowest and highest frequency, double ionization begins at a comparatively high field strength. For the three intermediate frequencies, double ionization sets in at lower field amplitudes and levels off with increasing field strength.

The field momentum $p = F_0/\omega$ is connected to the electron momentum components parallel to the laser field polarization by $p_{1,2} = 2\sqrt{U_p}$. At the ionization threshold, the field electron leaves at the field crossing and can gain up to $p_1 = 2\sqrt{U_p}$. The bound electron then leaves during the subsequent field maximum and its momentum will be near zero. The freed electron is the accelerated by the trailing end of the pulse. $2\sqrt{U_p}$ is then the energy expected for simultaneous emission of both electrons after re-collision.

Figure 6.2 is double logarithmic plot of the ionization yields as a function of peak field amplitudes from an ensemble of 2×10^5 initial conditions obtained from a single-cycle pulse calculated for five different field frequencies $\omega = 0.045$, 0.06, 0.08, 0.95, 0.13 a.u.. For the lowest and highest frequency used, double ionization yields were found only at high peak field amplitudes. For the three intermediate frequencies, an enhancement of the double ionization yields is found at smaller peak field amplitudes. There, the characteristic "knee" structure appears. All double ionization events are anti-parallel.

6.2 Two-Cycle Pulses

6.2.1 Tunneling at First Field Maximum

In a two-cycle field, the first field maximum has the smallest amplitude. The consequence of this is that the potential of the emerging saddle point in the Coulomb field is not that large. The initial position of the field electron is found far from the nucleus. However, during the field electrons' propagation there are two consecutive increasing field peaks from which it can gain energy.

The composition of the histogram Figure 6.3 is the same as in Figure 6.1. For the numerical simulations, each pulse with a peak field amplitude in the interval $F_0 \in [0.10 \text{ a.u.}, 0.30 \text{ a.u.}]$ and an array of 27 frequencies is calculated. The double ionization yields per bin, i.e. the yield density, in this figure is approximately double that in Figure 6.1. The additional field peaks open more channels to correlated double ionization.

The highlighted triangular area describing the parameter intervals for successful double ionization is similar to that in Figure 6.1. Starting the simulations at the first maximum in the two-cycle pulse, double ionization is found at far lower peak field amplitudes and frequencies. In this scenario, both parallel and anti-parallel NSDI occurs.

As in Figure 6.1, Figure 6.3 shows structures along the vertical in the highlighted region of double ionization. If read along the vertical or the horizontal, oscillations become apparent in the yield densities. For a high peak field amplitude and a small frequency, there is an initial high

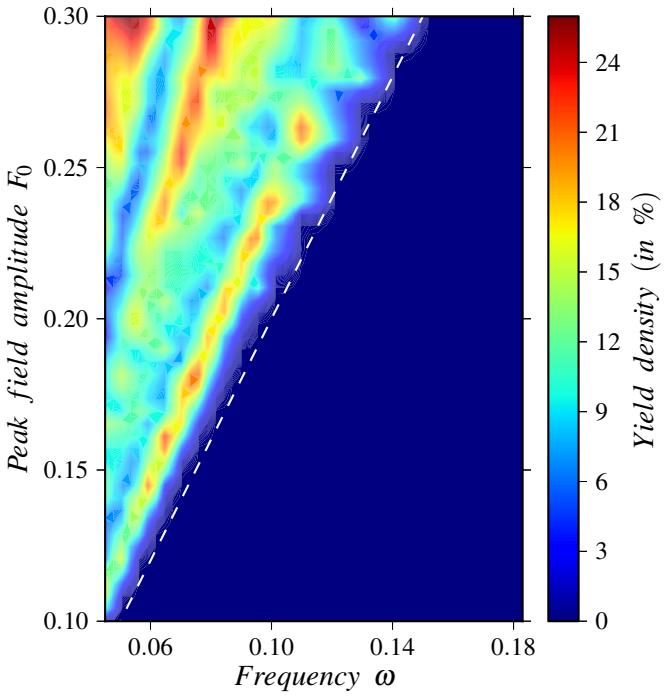

FIGURE 6.3: A histogram of the total double ionization yield density (in %) generated by an external two-cycle pulse using a range of peak field amplitudes and field frequencies. Simulations began at the first field maximum of the two-cycle pulse. As opposed to Figure 6.1, double ionization sets in at the lowest frequencies and field strengths. The white dotted line shows the boundary of $U_p = 1$ a.u.. The slope of the line is 2.0 a.u..

density of double ionization events. Then, for increasing frequency (along the horizontal), oscillations occur with decreasing strength in the density signal. The same is the case from a pulse with a low frequency. With increasing peak field amplitude (along the vertical), oscillations with increasing strength in the yield signal are found.

There is also a clear cut-off from the parameter space where double ionization occurs from where it does not. It is represented by the white dotted line with a slope $F_0/\omega = 2$ a.u.. This line describes the energy boundary of $F_0/\omega = 2\sqrt{U_p} = 2$ a.u. for $U_p = 1$ a.u.. Below this energy cut-off, no double ionization is found in the classical picture.

Figure 6.4 shows the double ionization yields obtained from simulations with an ensemble of 2×10^5 initial conditions. They were calculated from the first maximum of a two-cycle pulse for six different frequencies, $\omega = 0.045, 0.055, 0.065, 0.075, 0.085, 0.095$ a.u., and plotted in a double logarithmic plot over the ponderomotive potential. At low frequencies, the field electron returns to the parent ion at the second field maximum. In the case of a double ionization event, both electrons would spend the longest time in the field and gain the most energy. The aim is to to understand the differences between parallel and anti-parallel double ionization resulting from the various parameters.

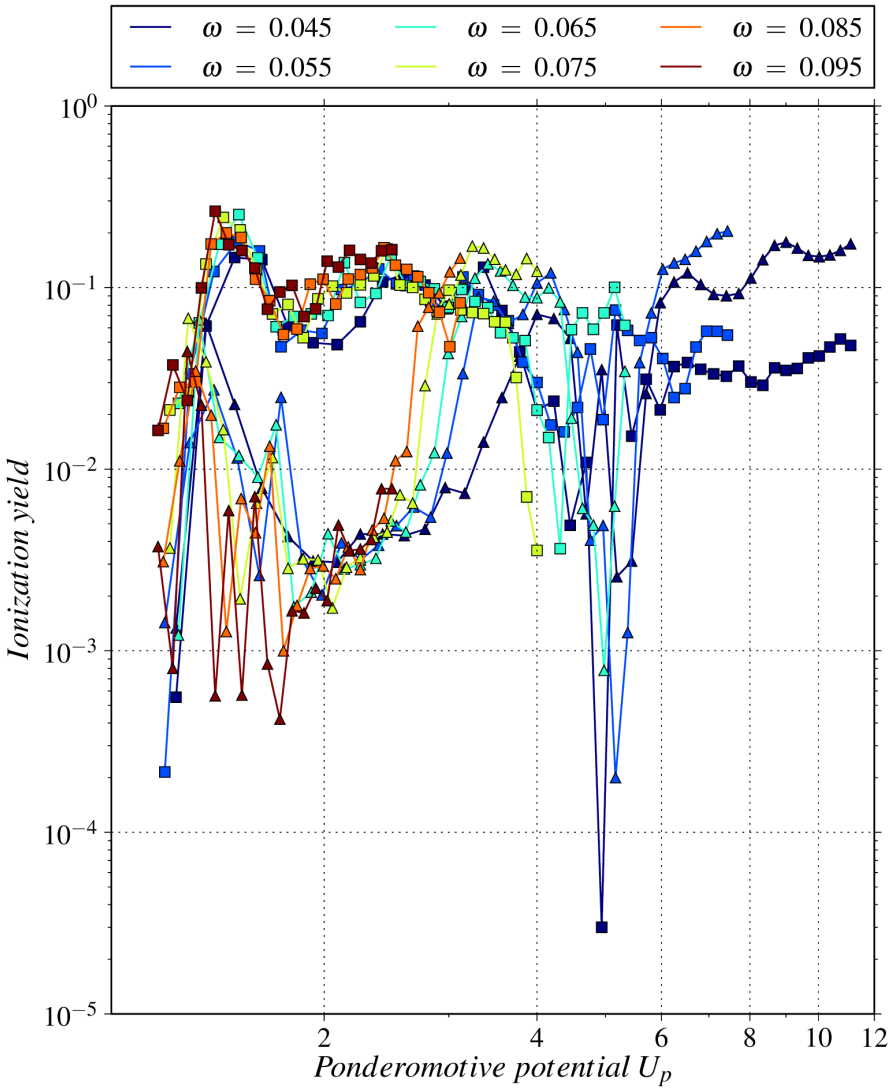

FIGURE 6.4: Ionization yields obtained from an ensemble of 2×10^5 initial conditions for a two-cycle pulse for six different frequencies. The non-sequential parallel ionization yields (squares) and total anti-parallel ionization (triangles) are plotted in a double logarithmic plot over the ponderomotive potential U_p. The simulations started at the first field maximum.

This field generates both parallel and anti-parallel double ionization. In Figure 6.4, the yields can be separated and studied individually. The triangles represent the anti-parallel double ionization. The squares indicate direct parallel double ionization. For each frequency, the parameter range of the field amplitudes is inserted and from this the ponderomotive energy is calculated. This serves to compare between the two different types of double ionization in the energy regions, low and high.

There are three regions in Figure 6.4 where, with increasing ponderomotive energy, different types of double ionization dominate. In the region $U_p \leq 2$ a.u., the direct parallel double ionization dominates. This is apparent for all frequencies calculated. The middle region lies near $U_p = 4$ a.u.. There, a transition occurs between the two styles of double ionization. An exception

are the yields for the highest frequency $\omega = 0.095$ a.u.. There are no double ionization events at a ponderomotive energy $U_p \geq 2.25$ a.u..

With increasing ponderomotive energy, 5 a.u.$\leq U_p \leq 7$ a.u., the double ionization events at higher frequencies begin to change. There is a crossover from parallel double ionization to anti-parallel double ionization. With decreasing field frequency, this crossover occurs at higher ponderomotive energies.

Finally, the third energy region in Figure 6.4 is approximately $U_p = 8$ a.u.. In this region only the lowest frequencies are plotted. Here, the anti-parallel NSDI dominates.

In summary, for low ponderomotive energies the parallel NSDI dominates for all frequencies considered. At high ponderomotive energies, the anti-parallel double ionization dominates. In between, there is a distinct crossover region. For a short interval both ionization types are equally represented. This crossover occurs for higher frequencies at lower energies.

6.2.2 Tunneling at Second Field Maximum

Figure 6.5 is a two-dimensional histogram of the double ionization yields of various peak field amplitudes and frequencies from a two-cycle sine-squared pulse. Simulations started at the second field maximum. The highlighted region depicting double ionization is similar to that from Figure 6.1. There is the same triangular shape with the vertical structures. However, within the same amplitude range double ionization occurs at higher frequencies, 0.13 a.u.$\leq \omega \leq 0.17$ a.u..

The dotted white line has a slope of $F_0/\omega = 1.64$ a.u. and divides the parameter space where double ionization is found from where it is not. The ponderomotive energy the electrons gain from the pulse along this barrier is smaller than 1 a.u.. Compared to the energy investigations in the two previous sections, there are significant double ionization yields in this region.

At high frequencies, the field electron returns after the largest peak in the pulse. The second to last maximum in the pulse activates the saddle in the Coulomb potential over which either one or both electrons escape. The short duration of pulses with high frequencies suggests that in the classical picture the double ionization is not likely. Especially, when simulations begin at the second maximum, there would be less time for the electrons to interact and doubly ionize.

Compared to the field electron tunneling at the first field maximum, the field electron which tunnels at the second maximum will have a comparatively short time after its return to the nucleus to ionize a second electron. Nevertheless, double ionization is very successful at high frequencies. In the parameter space where there is a strong signal for double ionization from the first maximum, there is no double ionization from simulations starting at the second maximum.

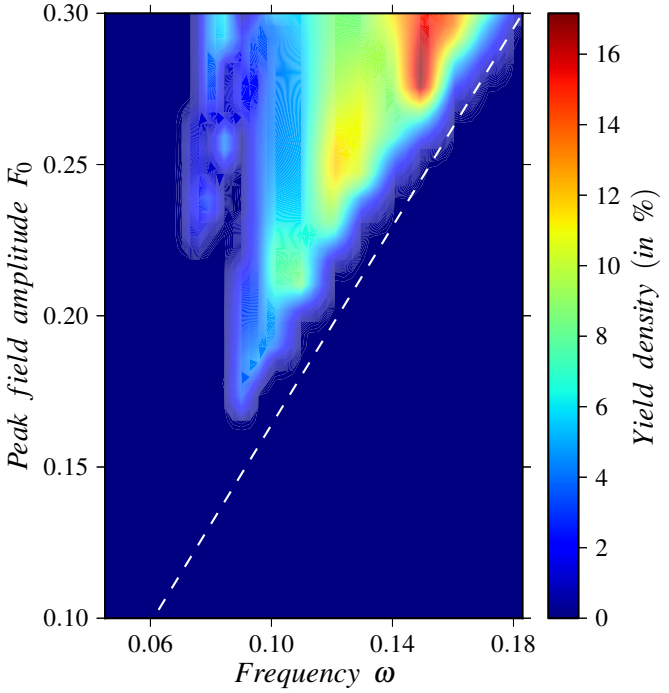

FIGURE 6.5: A histogram of the total double ionization yield density (in %) generated by an external two-cycle pulse using a range of peak field amplitudes and field frequencies. Simulations began at the second field maximum of the two-cycle pulse. As opposed to Figure 6.3, double ionization sets in at the highest frequencies and field strengths. The white dotted line shows the boundary of $U_p \approx 0.7$ a.u.. The slope of the line is 1.64 a.u..

Even at the same energy needed for double ionization in this region, at lower frequencies and field amplitudes, it does not suffice for ionizing two electrons.

A more detailed look into the double ionization yields is given in Figure 6.6. In this double logarithmic plot, the double ionization yields as a function of the peak field amplitude from an ensemble of 2×10^5 initial conditions for each six field frequencies are plotted. The data represented by triangles are the yields of anti-parallel and the squares represent the yields of parallel NSDI.

At small frequencies and amplitudes, the anti-parallel double ionization exceeds the parallel double ionization events by approximately two orders of magnitude. For the two lowest frequencies, the anti-parallel double ionization decreases with increasing peak field amplitude while the parallel double ionization increases. There is a crossover in the data near a peak field amplitude of $F_0 \approx 0.27$ a.u..

Figure 6.7 is a semi-logarithmic plot of the double ionization yields over the ponderomotive potential U_p for the same six frequencies as in Figure 6.6. Anti-parallel NSDI begins at energies $U_p \approx 0.7$ a.u.. There is a strong increase in the double ionization signal. The peaks in the yields are found at $U_p = 1$ a.u.. At higher energies, the yields begin to decrease. Parallel double

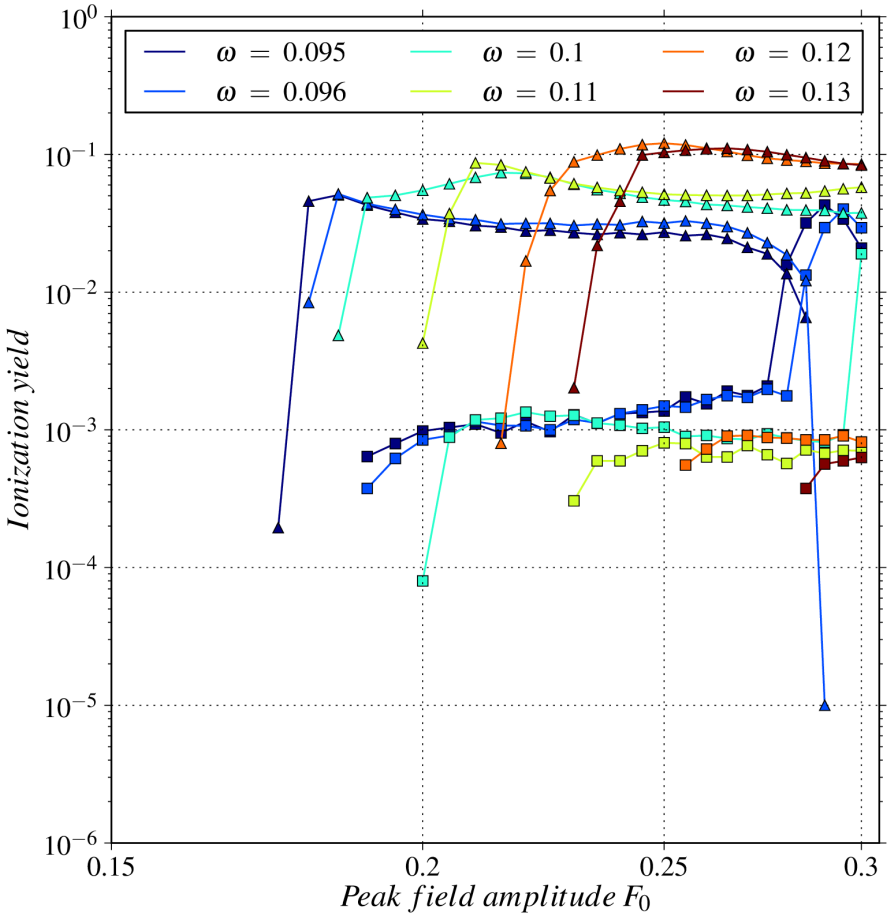

FIGURE 6.6: Ionization yields obtained from an ensemble of 2×10^5 initial conditions for a two-cycle pulse for six different frequencies. The non-sequential parallel ionization yields (squares) and total anti-parallel ionization (triangles) are plotted in a double logarithmic plot over the peak field amplitude F_0. The simulations started at the second field maximum.

ionization begins at $U_p = 1$ a.u.. For increasing energy, the parallel double ionization signal increases slowly up to $U_p = 2.0$ a.u. after which the signal increases significantly for the two smallest frequencies $\omega = 0.095$, 0.096 a.u. and, to some extent, $\omega = 0.1$ a.u.. In this energy region, the parallel double ionization signal completely dominates and the anti-parallel signal drops off completely.

To summarize, for low ponderomotive energies, the anti-parallel double ionization signal dominates whereas at high energies, the parallel double ionization signal dominates but only for low frequencies. This behavior is the exact opposite from that in Figure 6.4. The differences between both cases are when, in the field, the simulations start and the duration of pulse. Simulations starting from the first maximum, parallel double ionization dominates for low energies. Simulations starting at the second maximum, the anti-parallel double ionization dominates for low energies.

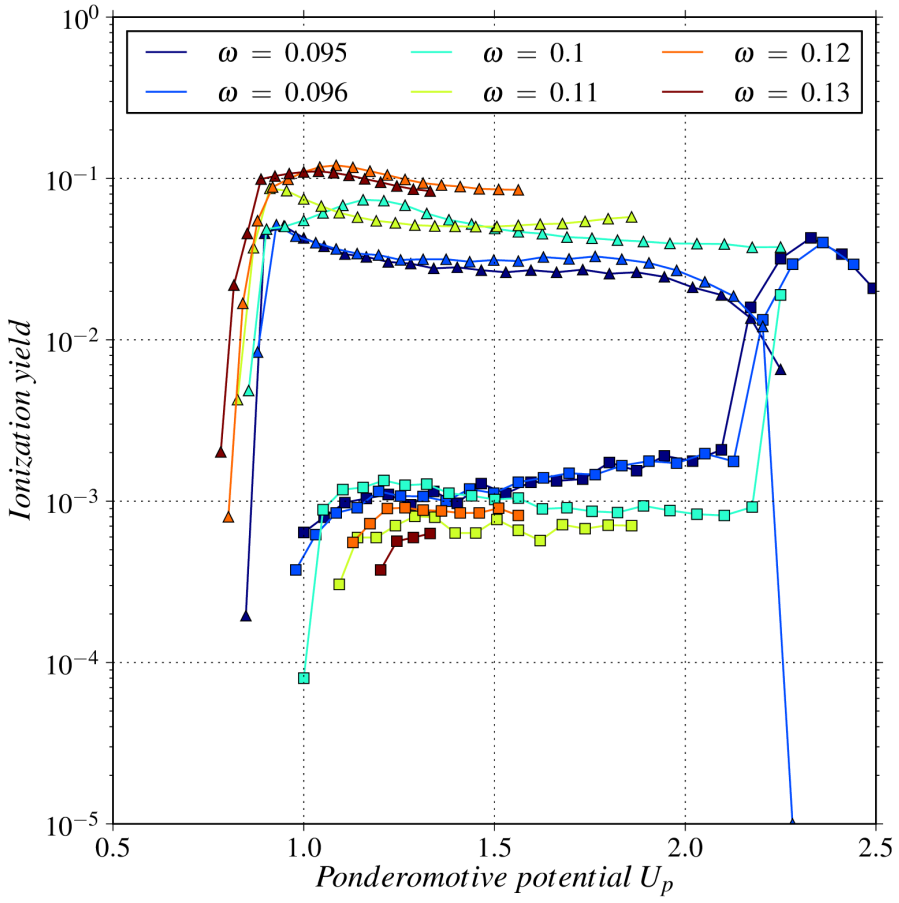

FIGURE 6.7: Ionization yields obtained from an ensemble of 2×10^5 initial conditions for a two-cycle pulse for six different frequencies. The non-sequential parallel ionization yields (squares) and total anti-parallel ionization (triangles) are plotted in a double logarithmic plot over the ponderomotive potential U_p. The simulations started at the second field maximum.

6.3 Discussion

The maximal kinetic energy the field electron can gain in the external field is $E_{kin}^{max} = \eta U_p$, where η is a number depending on the field phase when the electron has ionized. When the electron ionizes at the time of a zero-crossing in the field, the electron can gain $\eta = 3.17$. This is almost never the case in the calculations presented in this work, the exceptions can be seen in Figure 5.15 for $\omega = 0.096,\ 0.14$ a.u.. Barrier-suppression ionization is the main mechanism for the successful ionization of the bound electron. Electron ionization is only successful if the equation $\eta U_p \geq I_p - V_s$ is fulfilled, with V_s the saddle point energy and I_p the ionization potential.

F_0/ω is the field momentum and it is a constant value which separates the parameter space of successful double ionization from the classically forbidden tunnel regime. It follows that the ponderomotive energy that is associated with that field momentum, $F_0/\omega \propto \sqrt{U_p}$, is a constant of the particular system as well.

For different frequencies, the "knee" in the double ionization yields is found at different peak field amplitudes. From an experimental perspective, this would be especially important when using different lasers that produce light in different wavelengths.

Chapter 7

Comparison with Quantum Treatment

In this chapter, momentum distributions and double ionization yields from simulations using both the classical and quantum mechanical approach in the (1+1)-dimensional model are compared. A detailed account of the numerical methods for the quantum mechanical calculations is found in [72]. Since the two representations are fundamentally different they can only be compared qualitatively.

The need for a comparative treatment is revealed by Figure 7.1. The subplot $a)$ displays the double ionization results derived with the classical model in a two-dimensional histogram of momentum space, (p_1,p_2). Of all trajectories calculated, approximately 1% of the initial ensemble size doubly ionize. The color bar on the right is normed and shows the number of counts

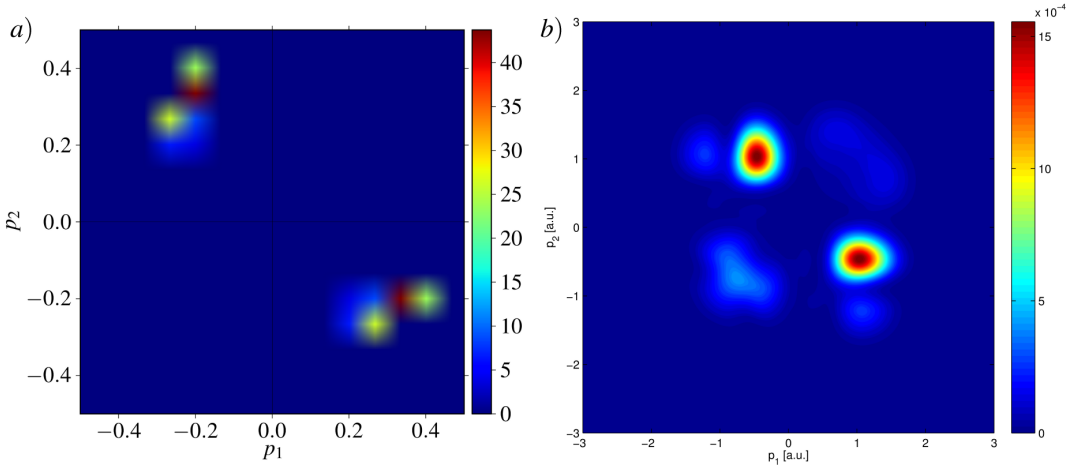

FIGURE 7.1: Momentum distribution of double ionization from a single-cycle field with an amplitude $F_0 = 0.30$ a.u., a frequency $\omega = 0.15$ a.u., and a phase $\phi = 0$. $a)$ is a two-dimensional histogram showing the momentum distribution from calculations using the classical representation. $b)$ is the momentum distribution from the simulations from the quantum representation of the model. The strong signal in the second and fourth quadrant suggest a dominant anti-parallel double ionization yield.

per bin area. The final momentum of both electrons from the same classical calculations is compared to the two-electron momentum distribution using the same parameters from a quantum treatment, Figure 7.1 b)[1].

A quantitative comparison between momentum in each plot reveals that the momentum of the electrons in b) is ≈ 2.5 times larger than the momentum of the electrons in a). In all the calculations using the classical picture, the simulations begin with the atom in the ground state. Within this parameter configuration, the incident electron returns to the ion with $U_p = 1$ a.u., which is the minimum needed for the double ionization event. Consequently, the momentum of the exiting electrons is low. In the simulations within the quantum picture, the ground state energy is given as a parameter but, once the calculations start, the electrons might occupy a higher energy state. This means that the bound electron has a lower ionization potential and at the collision both electrons have more momentum. Further classical calculations with the bound electron occupying an excited state are needed to verify this conclusion.

At first glance, there is a qualitatively good agreement between the two. The strong signals in the anti-parallel quadrants suggest back-to-back to dominates over the parallel double ionization. To verify this assumption, the quantum double ionization yields were calculated. In quantifying the contributions of correlated and anti-correlated yields, an unambiguous dominance of anti-correlated double ionization was expected.

7.1 Double Ionization Yields

In Figure 7.2 a), the parallel (squares) and anti-parallel (triangles) double ionization yields for a single-cycle field within an amplitude interval of $F \in [0.2 \text{ a.u.}, 0.3 \text{ a.u.}]$ using three frequencies $\omega = 0.06$ a.u. (red), 0.1 a.u. (blue), 0.15 a.u. (black) are plotted. Yields from the two-cycle pulse are included to demonstrate consistency in Figure 7.2 b).

These results are in direct contradiction to the conclusions drawn from the momentum distributions in Figure 7.1. The case presented in Figure 7.1 b) corresponds to the data plotted in black in Figure 7.2 a) at the peak field amplitude $F_0 = 0.3$ a.u.. The yields from all three frequencies show that parallel double ionization dominates. Secondly, with increasing frequency, back-to-back double ionization increases as well. An analysis of the criteria which distinguishes between parallel and anti-parallel double ionization in the respective programs for the classical and quantum representations is presented here.

In the classical representation, it is very straightforward. In position space, the final position of each electron is evaluated individually. Both must be sufficiently far away from the ion. In

[1] In this chapter, all simulations and the resulting figures within the quantum model were done by Jan Thiede.

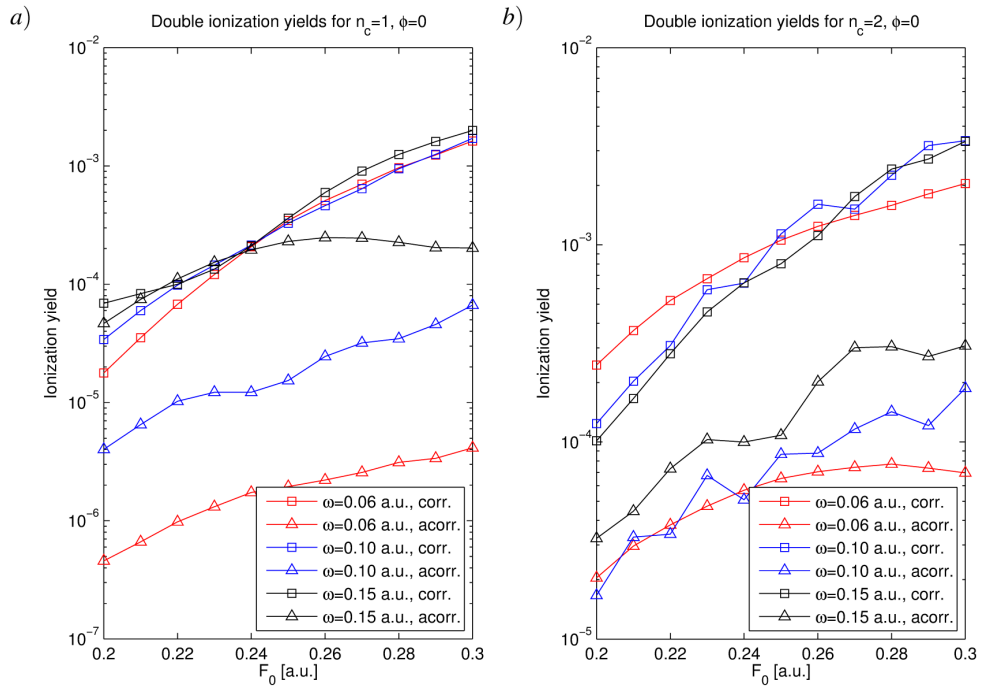

FIGURE 7.2: In a), the double ionization yields are plotted over the peak field amplitude of the single-cycle external pulse, where as in b) the double ionization yields from a two-cycle field are plotted. The data in red ($\omega = 0.06$ a.u.), blue ($\omega = 0.10$ a.u.), and black ($\omega = 0.15$ a.u.) are further divided into the parallel double ionization yields (squares) and anti-parallel double ionization (triangles).

determining the distance, one must take into account the number of field cycles, the frequency and the total calculation time. In fields with low frequencies, both electrons travel relatively long distances compared to those with high frequencies. For simulations using a high frequency, both electrons might not travel very far, but nevertheless satisfy the criteria for double ionization. This is illustrated in Figure 7.3. Furthermore, the final energy of each electron must be larger than zero, i.e. neither electron is bound to the ion, to be defined as ionized.

In the quantum representation, to ascertain the various double ionization yields in Figure 7.2, the configuration space is sub-divided into different regions. A finite area about the origin is allocated for the neutral atom. Beyond the atom, regions that define single and double ionization are determined. The flux of the electron wave function across the boundaries between regions is calculated. The construction of this partition of the configuration space is visualized in Figure 3.1 b). The size of the cross used in the quantum calculations is 7 a.u. $\times$ 12.5 a.u.. The yields for parallel escape entail contributions of the flux that pass *directly* from regions **A** to D_1 and D_3, and for anti-parallel escape the regions **a** to D_2 and D_4. If the flux passes from **A** to S_i to D_i, this would be classified as *indirect* or sequential double ionization .

In Figure 7.3, each plot is superimposed with the cross with the same dimensions used in the quantum simulations. In the low-frequency case, i.e. for $\omega = 0.06$ a.u., the trajectories would be classically classified as anti-correlated double ionization whereas in the quantum yields they

would be classified as single ionization. In the high-frequency case, i.e. $\omega = 0.15$ a.u., the interactions occur closer to the ion and the classical trajectories just barely pass directly from **A** to D_2. This accounts for the increase in anti-correlated yields in Figure 7.2 *a*) but it does not explain the higher yields of parallel double ionization.

7.2 Momentum Distributions

To determine the final two-electron momentum distribution, the wave function has a cross-bar along the electrons coordinates, with $|r_i|$ for $i = 1, 2$, removed while in position representation. However, the dimensions of the cross are approximately ten times larger in the calculations for the momentum distribution than in those for the yields, 100 a.u. vs. ~ 10 a.u.. This means that the many events which are recorded in the yields are not shown in the momentum distributions.

An example is shown in Figure 7.4. Using the same set of parameters as in Figure 7.1 *b*), a sequence of momentum distributions with different size cross-bars removed is presented.

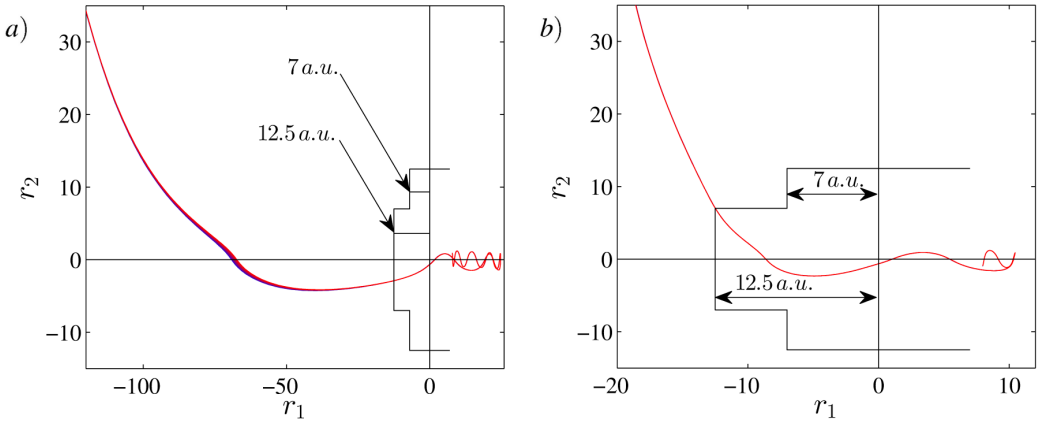

FIGURE 7.3: Classical electron trajectories with the boundary restrictions used in the quantum yields calculations. The trajectories are calculated using a frequency *a*) $\omega = 0.06$ a.u. and *b*) $\omega = 0.15$ a.u..

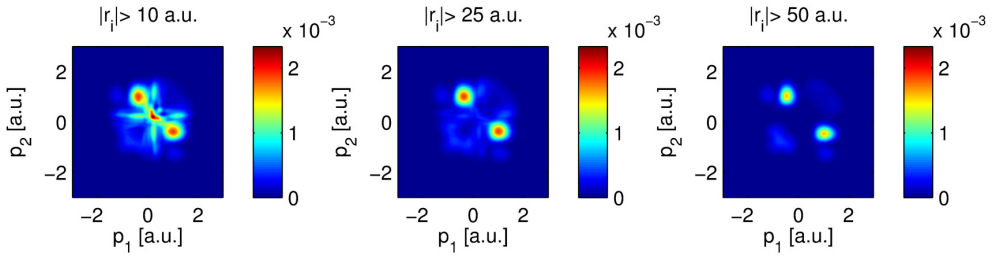

FIGURE 7.4: Momentum distributions from simulations using the quantum representation with different size cross-bar, $|r_i|$ for $i = 1, 2$, removed. The single-cycle field parameters are $F_0 = 0.3$ a.u., $\omega = 0.15$ a.u., $\phi = 0$.

The upper left figure has only a small cross-bar removed at $|r_i| > 10$ a.u.. A strong parallel double ionization signal in the first quadrant can be found close to the nucleus. It is this signal that is responsible for such high parallel yields in Figure 7.1 *b*). To compare the momentum distributions from quantum and classical calculations, the plot in the middle with the cross-size $|r_i| > 25$ a.u. would be most fitting. The dominant double ionization mechanism is the re-collision-induced excitation with subsequent ionization (RESI).

Nevertheless, even at $|r_i| > 50$ a.u., there is still a residual hint of parallel double ionization. An explanation as to its origin is given in the following section.

To summarize, reducing the size of the cross-bar is a valid correction for calculations in the high-frequency domain. Hidden sub-structures in the momentum distribution which have physical relevance are uncovered. This might lead to the possibility of scaling the cross-bar according to the field parameters, namely the field frequency.

7.3 Half-Cycle Pulse

In the quantum calculations, the two-electron momentum distribution can only be plotted once all parts of the wave function in position representation have been converted to momentum representation and added up. It is not possible to have a look at the momentum distribution mid-pulse. Therefore, the aim of this section is to minimize all possible re-scattering scenarios and focus on the results generated by a half-cycle pulse with a phase displacement of $\phi = \pi/2$ a.u.. A pulse with these field parameters is plotted in Figure 7.5.

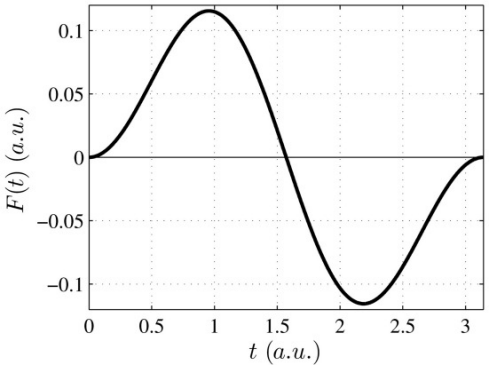

FIGURE 7.5: Half-cycle pulse with $\phi = 0.5\pi$ a.u.

The threshold intensity for impact ionization is found by $3.17\,U_p = E_0$. At this field intensity, the kinetic energy of the incident electron is equal to the ionization potential of the singly ionized atom. In the quantum picture, an excited electron may tunnel-ionize. The field electron returns, interacts with the bound electron and leaves near a field crossing. The energy transfer from the field electron is sufficient to excite the bound electron and it could tunnel at a subsequent field peak. From the results of the classical trajectory analysis, especially in the single-cycle case, the double ionization proceeds anti-parallel (RESI). If the field intensity is less than the threshold intensity, the kinetic energy of the incident electron is only enough to excite the bound electron.

Single-cycle sine-squared pulses, as defined in Figure 3.5, have three maxima. In classical simulations, calculations begin at the first field maximum. This is a sixth of a field length longer

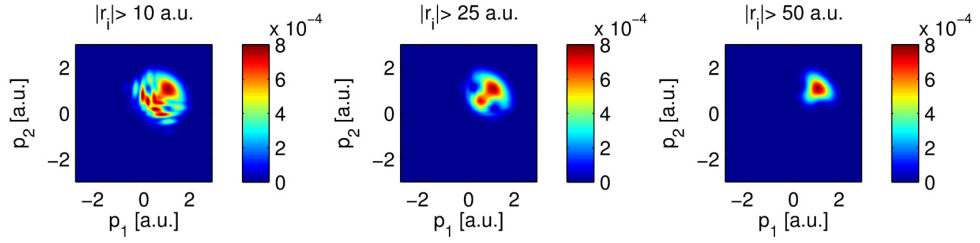

FIGURE 7.6: Momentum distributions from simulations using the quantum representation with different size cross-bar, $|r_i|$ for $i = 1, 2$, removed. **Half**-cycle field parameters are $F_0 = 0.2$ a.u., $\omega = 0.15$ a.u., $\phi = 0.5\pi$ a.u..

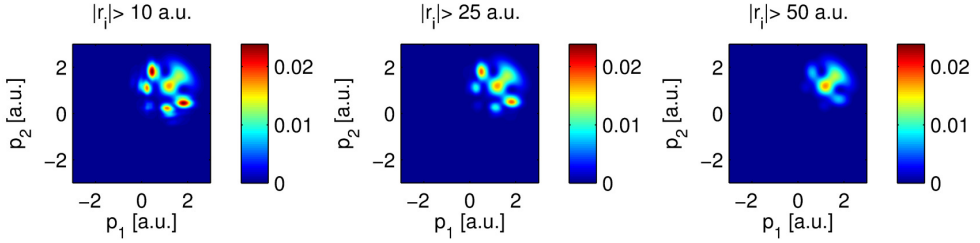

FIGURE 7.7: Momentum distributions from simulations using the quantum representation with different size cross-bar, $|r_i|$ for $i = 1, 2$, removed. **Half**-cycle field parameters are $F_0 = 0.3$ a.u., $\omega = 0.15$ a.u., $\phi = 0.5\pi$ a.u..

than a half-cycle pulse with a phase displacement of $\phi = \pi/2$ a.u.. Four scenarios were studied using such a field with $F_0 = 0.2$ and $F_0 = 0.3$ a.u., and for both $\omega = 0.15$ and $\omega = 0.06$ a.u.. In this scenario, multiple collisions are impossible. There is no time-delay between the initial collision and emission of the electrons.

In the high frequency case ($\omega = 0.15$ a.u.), the threshold intensity for impact ionization for an bound electron with ionization potential of 2 a.u. is $I_{th} = 0.056$ a.u. ($F_{th} \approx 0.24$ a.u.). In the below-threshold regime, tunneling must be taken into consideration because the kinetic energy of the incident electron is less than the ionization potential of the bound electron. Both electrons must leave symmetrically and simultaneously escape along the field polarization axis. The momentum distributions for $F_0 = 0.2$ a.u., with different sized cross-bars removed, is seen in Figure 7.6. Any deviation from this symmetry would result in no double ionization. This is mirrored by the weak ionization signal compared to Figure 7.7.

From Figure 7.6, the highly correlated electrons are produced via instantaneous impact ionization. It is apparent that in the high-frequency region, processes can be found close to the parent ion. A cross-bar with $|r_i| > 25$ a.u. in the momentum distribution captures the double ionization information.

In the high-frequency case ($\omega = 0.15$ a.u.) with above-threshold field intensity $F_0 = 0.3$ a.u., electrons may leave in the same direction and with slightly different momenta. This can be seen in the two signals on either side of the field polarization axis in Figure 7.7. Both electrons ionize

in the same direction either symmetrical with the same momentum or with slightly different momenta.

In the low-frequency case ($\omega = 0.06$ a.u.) and a field strength $F_0 = 0.2$ a.u., there is a more prominent and wider correlated double ionization signal in the momentum distributions seen in Figure 7.8. The field strength threshold for direct impact ionization is $F_{th} = 0.11$ a.u.. The field electron returns with a maximal kinetic energy of $E_{kin}^{max} \approx 9$. At intensities above the threshold for impact ionization, it has been found that there is an unequal distribution of the energy among the electrons at re-collision [78]. This would explain the momentum distributions in Figure 7.8.

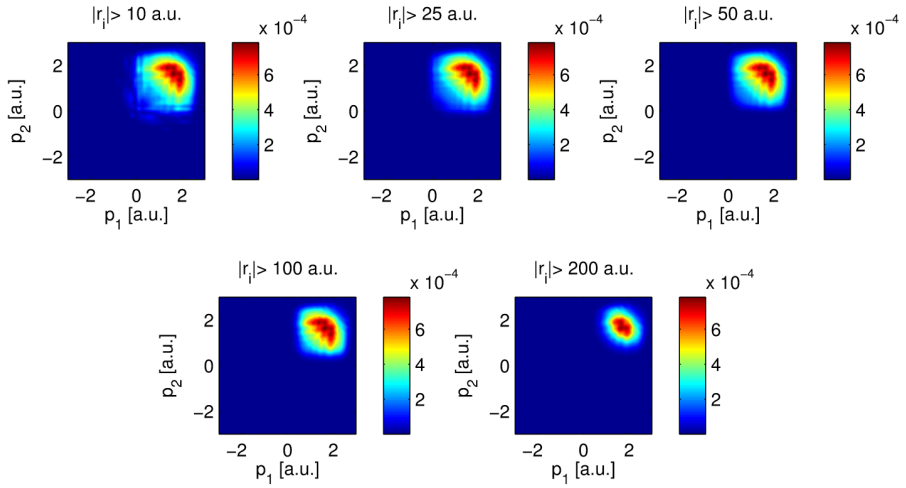

FIGURE 7.8: Momentum distributions from simulations using the quantum representation with different size cross-bar, $|r_i|$ for $i = 1, 2$, removed. **Half**-cycle field parameters are $F_0 = 0.2$ a.u., $\omega = 0.06$ a.u., $\phi = 0.5\pi$ a.u..

The figures in this section reveal the state of the electrons after propagation in one cycle of the field. In calculations within the quantum picture, a single oscillation in the field generates a parallel double ionization events, even for below-threshold intensities. The direct impact with tunneling is the only possible mechanism.

7.4 Discussion

A qualitative comparison of the double ionization signal in the momentum distributions from calculations using the quantum and classical picture, Figure 7.1, was carried out. A residual parallel double ionization signal observed in the momentum distribution, Figure 7.1 *b*), could not be explained by the calculated yields, Figure 7.2 *a*).

Multiple quantum calculations of double ionization generated by half-cycle pulses with various parameters were performed and analyzed. Both the high- and low-frequency regime with

both above- and below- threshold field intensities were studied. In the below-threshold intensity regime, the absence of multiple re-collisions and collision/emission time delay means that strongly correlated direct impact parallel double ionization via tunneling is the only double ionization mechanism.

In the case using a single-cycle field with a sine-squared envelope, the simple emission picture with the even symmetry is broken. The third maximum allows for two initial electron emission times and when the field changes sign, the field electron re-collides with the bound electron and leaves while the field is still on. The competing RESI mechanism necessitates all three peaks.

At high frequencies, the field electron experiences a relatively short excursion before it returns to the parent ion, bringing less kinetic energy than at low frequencies. For re-colliding electrons with low kinetic energy, field-assisted back-to-back emission is a key mechanism for double ionization. The re-collision induced excitation and subsequent field ionization mechanism for double ionization, reproduced in the classical picture, has a relatively large probability.

In the quantum picture, there two chances for the half-cycle direct parallel double ionization. As seen in Figure 7.7, the correlated escape is found parallel to the field polarization axis. The momentum distribution with the cross-bar $|r_i| > 50$ a.u., removed from the wave function, covers this up. Indeed, the proximity to the ion must be taken into account as these are relevant dynamics in NSDI.

At lower field frequencies, the whole double ionization process takes much longer. The field electron is pulled far from its parent ion and then returns with a higher kinetic energy. Figure 7.8 shows a more varied distribution of the electrons momentum from the half-cycle induced emission. This may occur twice together with the competing anti-correlated double ionization. The momentum distribution is much more complex.

Single-cycle pulses in classical calculations do not produce direct parallel double ionization. The Coulomb repulsion between the electrons and the unequal field maxima prevent it. In contrast to most other (semi-)classical models, the model employed does not have a built in allowance for electron tunneling [19, 29, 91, 92].

Chapter 8

Conclusion

Within a (1+1)-dimensional model, the classical dynamics of double ionization generated by one- and two-cycle laser pulses were analyzed. The classical treatment demanded the *ab initio* assumption, consistent with the re-scattering model for the double ionization process as a whole, that one electron had tunneled and emerged from the potential barrier with zero momentum. A one-parameter set of initial conditions for the bound electron on the energy shell in phase space was calculated. The electrons were propagated in two different laser pulses; a monochromatic wave with a trapezoidal envelope and a short pulse with a sine-squared envelope. A comprehensive study of the classical trajectories was undertaken.

In this thesis, the main focus was on the classical dynamics of non-sequential double ionization generated by a strong short pulse with a sine-squared envelope. The number of re-collisions was limited by the short pulse duration due to high field frequencies. All trajectories generated from a single-cycle pulse that described double ionization revealed that the electrons leave in opposite directions. It was observed that the electrons' mutual repulsion and the phase of the external field prevents parallel escape. This is in agreement with studies using a classical model for helium and experiments with argon which showed that back-to-back electron escape dominated at intensities at or below the ionization threshold [43, 60, 93]. The symmetric pathway to anti-parallel double ionization in which the electrons have the same value of energy and magnitude of momentum was identified. Furthermore, it was revealed that the anti-parallel double ionization could only proceed under specific conditions regarding the location of the bound electron within the potential well at the time of the field electron's return. Trajectories generated from two-cycle pulses with simulations starting from the first field maximum showed anti-parallel *and* parallel double ionization. Multiple non-sequential double ionization events in which both electrons had the same final momenta were identified. Their corresponding initial conditions in phase space were classified. Trajectories from simulations starting at the second field maximum resembled those generated from single-cycle pulses.

A monochromatic driving field with a trapezoidal envelope generated trajectories that described parallel non-sequential double ionization. At low-frequencies, trajectories were identified which showed simultaneous emission after a single collision. This was attributed to the presence of subsequent strong maxima in the field after the first re-scattering event. The incident electrons' return coincided with a field maximum which, in turn, provided the electrons with a direct path to double ionization across the saddle in the potential. With increasing field frequency, multiple re-collisions prior to field-assisted parallel double ionization resulted in more complex trajectories.

For pulses with a sine-squared envelope, a correlation between the initial conditions for the bound electron that lead to double ionization and the peak field amplitude was determined. For single-cycle pulses, all the initial conditions that lead to double ionization were found within one region in phase space. For two-cycle pulses, the initial conditions that lead to double ionization were found in clusters that are fragmentary and irregular. Since the external field strength influences the initial conditions, a phase dependency was expected as well.

Following the classical trajectories generated by a single-cycle pulse also revealed that the electrons' final state continued to change during a field-free propagation. The region of phase space, where the initial conditions that lead to double ionization were found, contracted.

A parameter study uncovered the frequency dependency of the double ionization yield in the classical picture. From the peak field amplitude and frequency, the classical threshold ionization boundary was reproduced.

A comparison of the momentum distributions derived from quantum and classical simulations using a single-cycle pulse and a high frequency showed a good qualitative agreement. However, quantum mechanical simulations showed a signal in the momentum distribution along the field polarization axis after a single field oscillation at intensities above and below the intensity threshold for non-sequential double ionization that the classical calculations could not reproduce. This points to the limitations of the classical model and the boundaries of the classical analysis.

Bibliography

[1] P. Agostini, G. Barjot, J. Bonnal, G. Mainfray, C. Manus, and J. Morellec, *Multiphoton ionization of hydrogen and rare gases*, IEEE Journal of Quantum Electronics **4** (1968), no. 10, 667–669.

[2] P. Agostini, F. Fabre, and G. Mainfray, *Free-free transitions following six-photon ionization of xenon atoms*, Physical Review Letters **42** (1979), no. 17, 1127–1130.

[3] P. Agostini, J. Kupersztych, and L.A. Lompré, *Direct evidence of ponderomotive effects via laser pulse duration in above-threshold ionization*, Physical Review A **36** (1987), no. 8, 4111–4114.

[4] M.V. Ammosov, N.B. Delone, and V. Krainov, *Tunnel ionization of complex atoms and of atomic ions in an alternating electromagnetic field*, Soviet Physics JETP **64** (1986), no. 6, 1191.

[5] D.G. Arbó, S. Yoshida, E. Persson, K.I. Dimitriou, and J. Burgdörfer, *Interference of electrons ionized by short laser pulses*, Journal of Physics: Conference Series **88** (2007), 012054.

[6] S. Augst, D.D. Meyerhofer, D. Strickland, and S.L. Chint, *Laser ionization of noble gases by Coulomb-barrier suppression*, Journal of the Optical Society of America B **8** (1991), no. 4, 858.

[7] S. Augst, D. Strickland, and D.D. Meyerhofer, *Tunneling ionization of noble gases in a high-intensity laser field*, Physical Review Letters **63** (1989), no. 20, 2212–2215.

[8] A.D. Bandrauk, F. Fillion-Gourdeau, and E. Lorin, *Atoms and molecules in intense laser fields: gauge invariance of theory and models*, Journal of Physics B: Atomic, Molecular and Optical Physics **46** (2013), no. 15, 153001.

[9] D. Bauer, *Two-dimensional, two-electron model atom in a laser pulse: Exact treatment, single-active-electron analysis, time-dependent density-functional theory, classical calculations, and nonsequential ionization*, Physical Review A **56** (1997), no. 4, 3028–3039.

[10] H.B. Bebb and A. Gold, *Multiphoton Ionization of Hydrogen and Rare-Gas Atoms*, Physical Review **143** (1966), no. 1, 1–24.

[11] A. Becker and F.H.M. Faisal, *Mechanism of laser-induced double ionization of helium*, Journal of Physics B: Atomic, Molecular and Optical Physics **29** (1996), no. 6, L197–L202.

[12] Andreas Becker and Farhad H.M. Faisal, *Interpretation of momentum distribution of recoil ions from laser induced nonsequential double ionization*, Physical review letters **84** (2000), no. 16, 3546–9.

[13] Andreas Becker and F.H.M. Faisal, *Interplay of electron correlation and intense field dynamics in the double ionization of helium*, Physical Review A **59** (1999), no. 3, R1742–R1745.

[14] B. Bergues, M. Kübel, N.G. Johnson, B. Fischer, N. Camus, K.J. Betsch, O. Herrwerth, A. Senftleben, A.M. Sayler, T. Rathje, T. Pfeifer, I. Ben-Itzhak, R.R. Jones, G.G. Paulus, F. Krausz, R. Moshammer, J. Ullrich, and M.F. Kling, *Attosecond tracing of correlated electron-emission in non-sequential double ionization.*, Nature communications **3** (2012), no. may, 813.

[15] E.G. Bessonov, *On a class of electromagnetic waves*, Soviet Physics JETP **858** (1981), no. March, 433–436.

[16] B.H. Bransden and C.J. Joachain, *Physics of Atoms and Molecules*, 2 ed., Prentice Hall, 2003.

[17] P.H. Bucksbaum, R.R. Freeman, M. Bashkansky, and T.J. McIlrath, *Role of the ponderomotive potential in above-threshold ionization*, Journal of the Optical Society of America B **4** (1987), no. 5, 760.

[18] J. Chen, J.H. Kim, and C.H. Nam, *Frequency dependence of non-sequential double ionization*, Journal of Physics B: Atomic, Molecular and Optical Physics **36** (2003), no. 4, 691–697.

[19] J. Chen, J. Liu, L. Fu, and W. Zheng, *Interpretation of momentum distribution of recoil ions from laser-induced nonsequential double ionization by semiclassical rescattering model*, Physical Review A **63** (2000), no. 1, 1–4.

[20] C. Cohen-Tannoudji, B. Diu, and F. Laloe, *Quantum Mechanics Volume Two*, 2 ed., John Wiley & Sons, Inc., Paris, France, 1977.

[21] P.B. Corkum, *Plasma perspective on strong field multiphoton ionization*, Physical Review Letters **71** (1993), no. 13, 1994–1997.

[22] M. Doerr, *Double ionization in a one-cycle laser pulse*, Optics Express **6** (2000), no. 5, 111.

[23] R. Dörner, T. Weber, and M. Weckenbrock, *Multiple ionization in strong laser fields*, Advances In Atomic, Molecular, and Optical Physics **48** (2002), 1–44.

[24] B. Eckhardt, J. Prauzner-Bechcicki, K. Sacha, and J. Zakrzewski, *Suppression of correlated electron escape in double ionization in strong laser fields*, Physical Review A **77** (2008), no. 1, 3–6.

[25] B. Eckhardt and K. Sacha, *Classical Analysis of Correlated Multiple Ionization in Strong Fields*, Physica Scripta **T90** (2001), no. 1, 185.

[26] Bruno Eckhardt, Jakub S. Prauzner-Bechcicki, Krzysztof Sacha, and Jakub Zakrzewski, *Phase effects in double ionization by strong short pulses*, Chemical Physics **370** (2010), no. 1-3, 168–174.

[27] Bruno Eckhardt and Krzysztof Sacha, *Classical threshold behaviour in a (1+1)-dimensional model for double ionization in strong fields*, Journal of Physics B: Atomic, Molecular and Optical Physics **39** (2006), no. 18, 3865–3871.

[28] P. Eckle, A.N. Pfeiffer, C. Cirelli, and A. Staudte, *Attosecond ionization and tunneling delay time measurements in helium*, science **322** (2008), no. 5907, 1525–9.

[29] A. Emmanouilidou, *Prevalence of different double ionization pathways and traces of three-body interactions in strongly driven helium*, Physical Review A **83** (2011), no. 2, 1–6.

[30] J. Feist, R. Pazourek, S. Nagele, E. Persson, B.I. Schneider, L.A. Collins, and J. Burgdörfer, *Electron correlation in two-photon double ionization of helium from attosecond to XFEL pulses*, Journal of Physics B: Atomic, Molecular and Optical Physics **42** (2009), no. 13, 134014.

[31] D.N. Fittinghoff, P.R. Bolton, B. Chang, and K.C. Kulander, *Polarization dependence of tunneling ionization of helium and neon by 120-fs pulses at 614 nm*, Physical Review A **49** (1994), no. 3, 2174–2177.

[32] H. Friedrich, *Theoretische Atomphysik*, 1 ed., Springer Berlin Heidelberg, 1990.

[33] L.-B. Fu, J. Liu, J. Chen, and S.-G. Chen, *Classical collisional trajectories as the source of strong-field double ionization of helium in the knee regime*, Physical Review A **63** (2001), no. 4, 043416.

[34] L.-B. Fu, J. Liu, and S.-G. Chen, *Correlated electron emission in laser-induced nonsequence double ionization of helium*, Physical Review A **65** (2002), no. 2, 021406.

[35] G. Gingras, A. Tripathi, and B. Witzel, *Wavelength and Intensity Dependence of Short Pulse Laser Xenon Double Ionization between 500 and 2300 nm*, Physical Review Letters **103** (2009), no. 17, 1–4.

[36] A. Gold and H.B. Bebb, *Theory of Multiphoton Ionization*, Physical Review Letters **14** (1965), no. 3, 60–63.

[37] M. Göppert-Mayer, *Über elementarakte mit zwei quantensprüngen*, Ph.D. thesis, 1931, pp. 273–294.

[38] E. Goulielmakis, M. Schultze, M. Hofstetter, V.S. Yakovlev, J. Gagnon, M. Uiberacker, A.L. Aquila, E.M. Gullikson, D.T. Attwood, R. Kienberger, F. Krausz, and U. Kleineberg, *Single-cycle nonlinear optics*, Science **320** (2008), no. 5883, 1614–7.

[39] R. Grobe and J.H. Eberly, *Single and double ionization and strong-field stabilization of a two-electron system*, Physical Review A **47** (1993), no. 3, R1605–R1608.

[40] F. Grossmann, *Theoretical Femtosecond Physics*, Springer Berlin Heidelberg, 2008.

[41] C. Guo, R.T. Jones, and G.N. Gibson, *Influence of spatial symmetry on the dynamics of strong-field ionization*, Physical Review A **62** (2000), no. 1, 015402.

[42] S. Haan, P. Wheeler, R. Panfili, and J. Eberly, *Origin of correlated electron emission in double ionization of atoms*, Physical Review A **66** (2002), no. 6, 061402.

[43] S.L. Haan, Z.S. Smith, K.N. Shomsky, and P.W. Plantinga, *Anticorrelated electrons from weak recollisions in nonsequential double ionization*, Journal of Physics B: Atomic, Molecular and Optical Physics **41** (2008), no. 21, 211002.

[44] P. Ho and J. Eberly, *Classical Effects of Laser Pulse Duration on Strong-Field Double Ionization*, Physical Review Letters **95** (2005), no. 19, 193002.

[45] P. Ho, R. Panfili, S. Haan, and J. Eberly, *Nonsequential Double Ionization as a Completely Classical Photoelectric Effect*, Physical Review Letters **94** (2005), no. 9, 1–4.

[46] J.D. Jackson, *Classical Electrodynamics*, 2. ed., John Wiley & Sons, Inc., New York, 1975.

[47] P. Kaminski, R. Wiehle, W. Kamke, H. Helm, and B. Witzel, *Wavelength dependence of double ionization of xenon in a strong laser field*, Physical Review A **73** (2006), no. 1, 013413.

[48] L.V. Keldysh, *Ionization in the field of a strong electromagnetic wave*, Soviet Physics JETP **20** (1965), 1307–1314.

[49] K. Kondo, A. Sagisaka, T. Tamida, Y. Nabekawa, and S. Watanabe, *Wavelength dependence of nonsequential double ionization in He*, Physical Review A **48** (1993), no. 4, R2531–R2533.

[50] R. Kopold, W. Becker, and M. Kleber, *Quantum path analysis of high-order above-threshold ionization*, Optics Communications **179** (2000), no. 1-6, 39–50.

[51] J. Krause, K. Schafer, and K. Kulander, *High-order harmonic generation from atoms and ions in the high intensity regime*, Physical Review Letters **68** (1992), no. 24, 3535–3538.

[52] J.L. Krause, K.J. Schafer, and K.C. Kulander, *Calculation of photoemission from atoms subject to intense laser fields*, Physical Review A **45** (1992), no. 7, 4998–5010.

[53] M.Y. Kuchiev, *Atomic antenna*, JETP Lett **45** (1987), 404.

[54] K.C. Kulander, K.J. Schafer, and J.L. Krause, *Theoretical model for intense field high-order harmonic generation in rare gases*, Laser Physics **3** (1993), no. 2, 359–364.

[55] S. Larochelle, A. Talebpour, and S.L. Chin, *Non-sequential multiple ionization of rare gas atoms in a Ti:Sapphire laser field*, Journal of Physics B: Atomic, Molecular and Optical Physics **31** (1998), no. 6, 1201–1214.

[56] M. Lein, E.K.U. Gross, and V. Engel, *On the mechanism of strong-field double photoionization in the helium atom*, Journal of Physics B: Atomic, Molecular and Optical Physics **33** (2000), no. 3, 433–442.

[57] A. L'Huillier, *Theoretical aspects of intense field harmonic generation*, Journal of Physics B: Atomic and Molecular Physics **24** (1999), no. 15, 3315–3341.

[58] A. L'Huillier, L.A. Lompre, G. Mainfray, and C. Manus, *Multiply charged ions induced by multiphoton absorption in rare gases at 0.53 μm*, Physical Review A **27** (1983), no. 5, 2503–2512.

[59] X. Liu, H. Rottke, E. Eremina, W. Sandner, E. Goulielmakis, K. Keeffe, M. Lezius, F. Krausz, F. Lindner, M. Schätzel, G. Paulus, and H. Walther, *Nonsequential Double Ionization at the Single-Optical-Cycle Limit*, Physical Review Letters **93** (2004), no. 26, 1–4.

[60] Y. Liu, S. Tschuch, A. Rudenko, M. Dürr, M. Siegel, U. Morgner, R. Moshammer, and J. Ullrich, *Strong-Field Double Ionization of Ar below the Recollision Threshold*, Physical Review Letters **101** (2008), no. 5, 053001.

[61] L. Madsen, *Gauge invariance in the interaction between atoms and few-cycle laser pulses*, Physical Review A **65** (2002), no. 5, 053417.

[62] F. Mauger, C. Chandre, and T. Uzer, *Strong field double ionization: what is under the "knee"?*, Journal of Physics B: Atomic, Molecular and Optical Physics **42** (2009), no. 16, 165602.

[63] D.B. Milosevic, G.G. Paulus, and W. Becker, *Above-threshold ionization with few-cycle laser pulses and the relevance of the absolute phase*, Laser Physics **13** (2003), no. 7, 948–958.

[64] U. Mohideen, M.H. Sher, and H.W.K. Tom, *High intensity above-threshold ionization of He*, Physical Review Letters **71** (1993), no. 4, 509–512.

[65] S.E. Moody and M. Lambropoulos, *ac Stark effect in multiphoton ionization*, Physical Review A **15** (1977), no. 4, 1497–1501.

[66] R. Moshammer, B. Feuerstein, J. López-Urrutia, J. Deipenwisch, A. Dorn, D. Fischer, C. Höhr, P. Neumayer, C. Schröter, J. Ullrich, H. Rottke, C. Trump, M. Wittmann, G. Korn, and W. Sandner, *Correlated two-electron dynamics in strong-field double ionization*, Physical Review A **65** (2002), no. 3, 035401.

[67] R. Moshammer, B. Feuerstein, W. Schmitt, A. Dorn, C. Schröter, J. Ullrich, H. Rottke, C. Trump, M. Wittmann, G. Korn, K. Hoffmann, and W. Sandner, *Momentum Distributions of Ne+ Ions Created by an Intense Ultrashort Laser Pulse*, Physical Review Letters **84** (2000), no. 3, 447–450.

[68] H.G. Muller and H. B. van Linden van den Heuvell, *Multiphoton ionization of xenon with 100-fs laser pulses*, Physical Review Letters **60** (1988), no. 7, 565–568.

[69] R. Panfili, J. Eberly, and S. Haan, *Comparing classical and quantum simulations of strong-field double-ionization*, Optics Express **8** (2001), no. 7, 431.

[70] R. Panfili, S. Haan, and J. Eberly, *Slow-Down Collisions and Nonsequential Double Ionization in Classical Simulations*, Physical Review Letters **89** (2002), no. 11, 113001.

[71] J. Prauzner-Bechcicki, K. Sacha, B. Eckhardt, and J. Zakrzewski, *Time-Resolved Quantum Dynamics of Double Ionization in Strong Laser Fields*, Physical Review Letters **98** (2007), no. 20, 1–4.

[72] Jakub Prauzner-Bechcicki, Krzysztof Sacha, Bruno Eckhardt, and Jakub Zakrzewski, *Quantum model for double ionization of atoms in strong laser fields*, Physical Review A **78** (2008), no. 1, 013419.

[73] K. Sacha and B. Eckhardt, *Pathways to double ionization of atoms in strong fields*, Physical Review A **63** (2001), no. 4, 1–9.

[74] Krzysztof Sacha and Bruno Eckhardt, *Pathways to non-sequential multiple ionization in strong laser fields*, Journal of Physics B: Atomic, Molecular and Optical Physics **36** (2003), no. 19, 3923–3935.

[75] G. Sansone, E. Benedetti, F. Calegari, C. Vozzi, L. Avaldi, R. Flammini, L. Poletto, P. Villoresi, C. Altucci, R. Velotta, S. Stagira, S. De Silvestri, and M. Nisoli, *Isolated single-cycle attosecond pulses.*, Science (New York, N.Y.) **314** (2006), no. 5798, 443–6.

[76] F. Schwabl, *Quantenmechanik*, 2 ed., Springer Berlin Heidelberg, Berlin, Heidelberg, 1990.

[77] T. Shaaran, M.T. Nygren, and C.F. de Morisson Faria, *Laser-induced nonsequential double ionization at and above the recollision-excitation-tunneling threshold*, Physical Review A **81** (2010), no. 6, 063413.

[78] A. Staudte, C. Ruiz, M. Schöffler, S. Schössler, D. Zeidler, T. Weber, M. Meckel, D. Villeneuve, P. Corkum, A. Becker, and R. Dörner, *Binary and Recoil Collisions in Strong Field Double Ionization of Helium*, Physical Review Letters **99** (2007), no. 26, 1–4.

[79] G. Steinmeyer, *Frontiers in Ultrashort Pulse Generation: Pushing the Limits in Linear and Nonlinear Optics*, Science **286** (1999), no. 5444, 1507–1512.

[80] K.T. Taylor, J.S. Parker, and D. Dundas, *Laser-Driven Helium in Full-Dimensionality*, Laser Physics **9** (1999), no. 1, 98–104.

[81] F.S. Tsung, C. Ren, L.O. Silva, W.B. Mori, and T. Katsouleas, *Generation of ultra-intense single-cycle laser pulses by using photon deceleration.*, Proceedings of the National Academy of Sciences of the United States of America **99** (2002), no. 1, 29–32.

[82] G.S. Voronov, G.A. Delone, and N.B. Delone, *Multiphoton Ionization of Krypton and Argon by Ruby Laser Radiation*, Soviet Physics JETP **3** (1966), no. 12, 480–483.

[83] G.S. Voronov and N.B. Delone, *Ionization of the xenon atom by the electric field of ruby laser emission*, Soviet Physics JETP **1** (1965), no. 2, 66.

[84] B. Walker, B. Sheehy, L.F. DiMauro, P. Agostini, K. Schafer, and K. Kulander, *Precision Measurement of Strong Field Double Ionization of Helium*, Physical Review Letters **73** (1994), no. 9, 1227–1230.

[85] G. Wannier, *The Threshold Law for Single Ionization of Atoms or Ions by Electrons*, Physical Review **90** (1953), no. 5, 817–825.

[86] D.A. Wasson and S.E. Koonin, *Molecular-dynamics simulations of atomic ionization by strong laser fields*, Physical Review A **39** (1989), no. 11, 5676–5685.

[87] J. Watson, A. Sanpera, D. Lappas, P. Knight, and K. Burnett, *Nonsequential double ionization of helium*, Physical Review Letters **78** (1997), no. 10, 1884–1887.

[88] T. Weber, H. Giessen, M. Weckenbrock, G. Urbasch, A. Staudte, L. Spielberger, O. Jagutzki, V. Mergel, M. Vollmer, and R. Dörner, *Correlated electron emission in multiphoton double ionization*, Nature **405** (2000), no. 6787, 658–61.

[89] T. Weber and M. Weckenbrock, *Sequential and nonsequential contributions to double ionization in strong laser fields*, Journal of Physics B: Atomic and Molecular Physics **33** (2000), no. 4, L127–L133.

[90] T. Weber, M. Weckenbrock, A. Staudte, L. Spielberger, O. Jagutzki, V. Mergel, F. Afaneh, G. Urbasch, M. Vollmer, H. Giessen, and R. Dörner, *Recoil-Ion Momentum Distributions for Single and Double Ionization of Helium in Strong Laser Fields*, Physical Review Letters **84** (2000), no. 3, 443–446.

[91] G. Xin, D. Ye, and J. Liu, *Dependence of the correlated-momentum patterns in double ionization on the carrier-envelope phase and intensity of a few-cycle laser pulse*, Physical Review A **82** (2010), no. 6, 2–9.

[92] D. Ye, X. Liu, and J. Liu, *Classical Trajectory Diagnosis of a Fingerlike Pattern in the Correlated Electron Momentum Distribution in Strong Field Double Ionization of Helium*, Physical Review Letters **101** (2008), no. 23, 1–4.

[93] D.F. Ye and J. Liu, *Strong-field double ionization at the transition to below the recollision threshold*, Physical Review A **81** (2010), no. 4, 1–8.